

ARTICLE TYPE

SALT spectroscopic follow-up of the G4Jy Sample

Sarah V. White,^{1,2} Kshitij Thorat,³ Moses Mogotsi,¹ Rosalind E. Skelton,¹ Soloher M. Randriamampandry,^{1,4} Encarni Romero-Colmenero,¹ Precious K. Sejake,³ Francesco Massaro,^{5,6,7} Abigail García-Pérez,^{5,8,9} Ana Jiménez-Gallardo,⁹ Harold A. Peña-Herazo,¹⁰ and Edward N. Taylor¹¹

¹South African Astronomical Observatory (SAAO), PO Box 9, Observatory, 7935, South Africa

²Department of Physics and Electronics, Rhodes University, PO Box 94, Makhanda, 6140, South Africa

³Department of Physics, University of Pretoria, Hatfield, Pretoria, 0028, South Africa

⁴A&A, Department of Physics, Faculty of Sciences, University of Antananarivo, PO Box 906, Antananarivo, Madagascar

⁵Dipartimento di Fisica, Università degli Studi di Torino, via Pietro Giuria 1, I-10125 Torino, Italy

⁶Istituto Nazionale di Astrofisica (INAF) - Osservatorio Astrofisico di Torino, via Osservatorio 20, 10025 Pino Torinese, Italy

⁷Istituto Nazionale di Fisica Nucleare (INFN) - Sezione di Torino, via Pietro Giuria 1, I-10125 Torino, Italy

⁸Instituto Nacional de Astrofísica, Óptica y Electrónica, Luis Enrique Erro 1, Tonantzintla, Puebla 72840, México

⁹European Southern Observatory (ESO), Alonso de Córdova 3107, Vitacura, Región Metropolitana, Chile

¹⁰East Asian Observatory (EAO), 660 N. A'ohōkū Place, Hilo, HI 96720, USA

¹¹Centre for Astrophysics and Supercomputing, Swinburne University of Technology, Hawthorn 3122, Melbourne, Australia

Author for correspondence: Sarah V. White, Email: sarahwhite.astro@gmail.com.

(Received 1 April 2025; revised 7 May 2025; accepted 16 May 2025; first published online 21 May 2025)

Abstract

The GLEAM 4-Jy (G4Jy) Sample is a thorough compilation of the ‘brightest’ radio sources in the southern sky (Declination $< 30^\circ$), as measured at 151 MHz ($S_{151\text{ MHz}} > 4.0\text{ Jy}$) with the Murchison Widefield Array (MWA), through the GaLactic and Extragalactic All-sky MWA (GLEAM) Survey. In addition to flux-density measurements, the G4Jy catalogue^a provides host-galaxy identifications (through careful visual-inspection) and four sets of spectral indices. Despite their brightness in the radio, many of these sources are poorly-studied, with the vast majority lacking a spectroscopic redshift in published work. This is crucial for studying the intrinsic properties of the sources, and so we conduct a multi-semester observing campaign on the Southern African Large Telescope (SALT), with optical spectroscopy enabling us to provide new redshifts to the astronomical community. Initial results show that not all of the host galaxies exhibit emission-line spectra in the optical ($\sim 4500\text{--}7500\text{\AA}$), which illustrates the importance of radio-frequency selection (rather than optical selection) for creating an *unbiased* sample of active galactic nuclei. By combining SALT redshifts with those from the 6-degree Field Galaxy Survey (6dFGS) and the Sloan Digital Sky Survey (SDSS), we calculate radio luminosities and linear sizes for 299 G4Jy sources (which includes one newly-discovered giant radio-galaxy, G4Jy 604). Furthermore, with the highest redshift acquired (so far) being $z \sim 2.2$ from SDSS, we look forward to evolution studies of this complete sample, as well as breaking degeneracies in radio properties with respect to, for example, the galaxy environment.

^a<https://github.com/swv26/G4Jy>

1. Introduction

Powerful active-galactic-nuclei (AGN) feature heavily in our understanding of galaxy evolution, with AGN activity thought to promote (e.g. Ishibashi & Fabian, 2012; Silk, 2013) or suppress (e.g. Croton et al., 2006; Davies et al., 2020; Lammers et al., 2023) star formation in the host galaxy. Meanwhile, radio observations are unaffected by dust obscuration, and so allow such activity to be detected out to higher redshift than is possible at other wavelengths (e.g. Collier et al., 2014; Singh et al., 2014). This includes finding high-redshift (proto-)clusters, by exploiting the tendency of ‘radio-loud’ AGN to reside in dense environments (Venemans et al., 2007; Wylezalek et al., 2013; Hlavacek-Larrondo et al., 2015). However, when studying the properties of powerful AGN as a function of redshift and/or environment, detailed research is hindered by small-number statistics.

Currently, the revised Third Cambridge Catalogue of Radio Sources (3CRR; Laing et al., 1983) is the most-prominent, low-frequency radio-source sample ($S_{178\text{ MHz}} > 10.9\text{ Jy}$) that

is optically complete, but this consists of only 173 sources (all in the northern hemisphere). White et al. (2018, 2020a,b) have created a sample that is over 10 times larger—the GLEAM 4-Jy (G4Jy) Sample—using observations from the Murchison Widefield Array (MWA; Tingay et al., 2013) over the entire southern sky (Dec. $< 30^\circ$). Thanks to these measurements at low radio-frequencies, we can select radio-loud AGN in an orientation-independent way (Barthel, 1989). This is because the low-frequency emission of powerful AGN is dominated by the radio lobes, which are not subject to relativistic beaming (Rees, 1966). The same cannot be said for the radio core, ‘hotspots’, and jets that dominate the emission of sources at high radio-frequencies. As a result of this beaming effect, radio sources selected at high frequencies tend to be biased towards AGN that have their jet axis close to the line-of-sight (e.g. Lister, 2003). Therefore, with 1,863 of the brightest radio-sources at low frequencies making up the G4Jy Sample, we can test models of powerful AGN more robustly than previously (e.g. Mullin et al., 2008; Wang & Kaiser, 2008; Best &

Heckman, 2012; Shabala et al., 2020). However, the paucity of existing optical spectroscopy over the southern sky [e.g. through the 6-degree Field Galaxy Survey, 6dFGS; Jones et al. (2009)] significantly limits the breadth of science that can be undertaken, hence our follow-up of a large fraction of G4Jy sources (Sejake et al., in prep.) using the Southern African Large Telescope (SALT).

In this paper, our results include some of the very ‘brightest’ of the G4Jy Sample, as determined through their integrated flux-density at ~ 178 MHz. Applying a threshold of 9.0 Jy^a here allows us to define a subsample that is equivalent to the first revised version of the Third Cambridge catalogue of radio sources (3CR survey; Bennett, 1962; Spinrad et al., 1985) of the northern hemisphere. Hence, they are referred to as *the G4Jy-3CRE subset* (Massaro et al., 2023a). To ensure that there is not overlap with the 298 extragalactic sources that comprise the 3CR sample, a criterion is applied with respect to the sky coverage ($\text{Dec.} < -5^\circ$), resulting in a list of 264 G4Jy sources. These sources are being studied in the X-ray (e.g. Massaro et al., 2023b) in order to better-understand how radio jets interact with their surroundings, with additional optical spectroscopy being provided via numerous telescopes (e.g. García-Pérez et al., 2024). The intrinsic radio-properties of these G4Jy-3CRE sources will be presented (in more-complete form) in future work.

We also plan to extend X-ray follow-up to the wider G4Jy Sample as a whole. However, **to ensure good signal-to-noise ratios we need to have high spectroscopic completeness** so that sources are not biased with respect to dust obscuration. This is also necessary for creating appropriate subsamples for observations with the Atacama Large Millimeter Array (ALMA), which would allow us to address questions about the amount of gas that is available for black-hole accretion and star formation. The wide range in optical magnitudes for our sources makes the G4Jy Sample particularly suitable for large-scale follow-up with SALT, offering us a firm foundation for combining with additional spectroscopy in the future.

1.1 Paper outline

In the next section (Section 2), we describe the criteria that were applied to the G4Jy Sample in order to generate the target list for our spectroscopic campaign with SALT. The resulting spectra are presented in Appendix 2, and the acquired redshifts are summarised in Section 3. Section 3 also discusses the radio luminosities and linear sizes for G4Jy sources, enabled by the collation of 299 redshifts. J2000 co-ordinates and AB magnitudes are used throughout this work, and we use a Λ CDM cosmology, with $H_0 = 70 \text{ km s}^{-1} \text{ Mpc}^{-1}$, $\Omega_m = 0.3$, $\Omega_\Lambda = 0.7$.

2. Target selection and Data acquisition

In creating the G4Jy Sample, White et al. (2020b,a) used the GaLactic and Extragalactic All-sky MWA (GLEAM) catalogue (Hurley-Walker et al., 2017) to select 1,863 radio-sources

brighter than 4.0 Jy at 151 MHz (with a spatial resolution of ~ 2 arcmin). They then used higher-resolution images from:

1. the TIFR GMRT Sky Survey (TGSS) first alternative data release (ADR1; Intema et al., 2017), at ~ 25 arcsec resolution,
2. the Sydney University Molonglo Sky Survey (SUMSS) catalogue (Mauch et al., 2003; Murphy et al., 2007), at ~ 45 arcsec, and
3. the NRAO (National Radio Astronomy Observatory) VLA Sky Survey (NVSS; Condon et al., 1998) at ~ 45 arcsec,

to determine the radio morphology of the sources, and help to identify the host galaxies (Figure 1). The latter was done through careful visual inspection, using W1-band images from AllWISE (Cutri et al., 2013) to *avoid being biased against the most dust-obscured sources*. The result is that 1,606 of the 1,863 sources have identifications in the (original) G4Jy catalogue (White et al., 2020a,b), 1,253 of which are at Declinations accessible by SALT ($-76^\circ < \text{Dec.} < 11^\circ$). Considering the 1,606 sources, we remove 136 with spectra from the 6-degree Field Galaxy Survey (6dFGS; Jones et al., 2009), and 104 with Sloan Digital Sky Survey (SDSS) spectra (DR12; Alam et al., 2015). This illustrates that we still require optical spectroscopy for the vast majority of the sample, primarily in order to obtain robust redshifts and (where possible) determine the accretion modes of these radio galaxies.

When compiling *R*-band magnitudes for the sample (Figure 2) in January 2020 (SALT proposal: 2020-1-MLT-008, PI: White), we cross-matched the AllWISE host-galaxy positions with the following datasets, using a radius of 1 arcsec: SuperCOSMOS (Hambly et al., 2001), the National Optical Astronomy Observatory (NOAO) Source Catalog (NSC) DR1 (Nidever et al., 2018), the Dark Energy Spectroscopic Instrument (DESI) Legacy Imaging Surveys (LS) DR8 (Dey et al., 2019), SDSS DR12 (Alam et al., 2015), SkyMapper DR1.1 (Wolf et al., 2018) and PanSTARRS (Flewelling et al., 2020) photometry newly-extracted using ProFound (Robotham et al., 2018). (Further details are provided in Appendix 1.) The scatter in magnitudes from the different datasets was then assessed and used to convert everything onto the SuperCOSMOS magnitude scale. The aim of our SALT follow-up is to get good completeness for the G4Jy Sample down to $R = 20.0$ mag (the optical limit of the SuperCOSMOS data), and doing so gives us a subsample of 706 sources (at $-76^\circ < \text{Dec.} < 11^\circ$, and including the 158 sources with 6dFGS/SDSS spectra in this range). An additional 38 G4Jy sources were added to the SALT target-list, thanks to new host-galaxy identifications provided by Sejake et al. (2023) via 1300-MHz MeerKAT imaging (of ~ 7 -arcsec spatial resolution). For a summary of the number of sources considered, please see Table 1.

^aNoting the calibration differences found by Roger et al. (1973) with respect to the original 3C observations, application of a 9.8-Jy threshold results in 181 G4Jy sources at $\text{Dec.} < -5^\circ$ (Massaro et al., 2023a).

Table 1. A summary of how the target list of 586 G4Jy sources was derived from the original catalogue of 1,863 sources (White et al., 2020a,b). This summary also accounts for the 299 redshifts presented in this paper. Note that 12 of the 98 host-galaxy positions provided by Sejake et al. (2023) were confirmation of existing identifications in the G4Jy catalogue.

Description	Tally of redshifts	Tally of SALT targets
1,863 sources in the G4Jy catalogue	–	–
1,606 with AllWISE identifications (IDs)	–	–
SALT-accessible sources ($-76^\circ < \text{Dec.} < 11^\circ$)	–	1,253
Apply the R -band cut, aiming for completeness	–	706
136 sources in 6dFGS DR3 (Jones et al., 2009)	136	573
104 sources in SDSS DR12 (Alam et al., 2015)	240	548
98 IDs via MeerKAT images (Sejake et al., 2023)	–	–
38 of these sources are at $-76^\circ < \text{Dec.} < 11^\circ$	–	586
53 sources in SDSS DR16 (Ahumada et al., 2020)	293	–
36 of these overlap with SDSS DR12	257	–
100 SALT spectra reduced as part of monitoring	299	586

Targetting ($706 - 158 + 38 =$) 586 G4Jy sources^b enables investigation of a subsample that is over 10 times larger than the number of 3CRR sources at $R < 20.0$. This allows us to determine more-robust statistics for comparing with galaxy-evolution simulations, making this an excellent legacy dataset for studying powerful active galaxies as a function of redshift and environment. The all-sky distribution of our sources means that we have relaxed scheduling restraints with respect to Right Ascension and Declination, whilst the broad range of R -band magnitudes (Figure 2) means that we can take advantage of SALT time that is available for different moon conditions; ‘Bright’ time is suitable for the 316 targets that are at $R < 18.5$ mag, and ‘Grey’ time is selected for the 270 targets that are at $18.5 \leq R/\text{mag} < 20.0$. Thanks to the sources with brighter magnitudes, we can also accommodate more-difficult seeing conditions (up to 2.5 arcsec).

We observe the sources via the pg0900 grating on the SALT Robert Stobie Spectrograph (RSS), at the standard grating-angle of 15.875° , and with the pc03850 Order-Blocking Filter. This provides the resolution ($R = \sim 660 - 930$) and wavelength coverage ($\sim 4500 - 7500\text{\AA}$) for maximising redshift completeness ($z \lesssim 4.5$) and broad-line width measurement. Acquisition involves imaging the field using the SALT Imaging Camera (SALTICAM, also abbreviated to SCAM), and (typically) identifying an acquisition object that allows fainter targets to enter the longslit via the ‘blind-offset’ method (see Appendix 2). Also, we split the observations into 2 to 3 exposures per target (in order to enable cosmic-ray removal), and perform wavelength calibrations using the RSSMOSPipeline software^c (Hilton et al., 2018), facilitated by arc-observations of a Xenon lamp. This Python-based pipeline automatically: de-

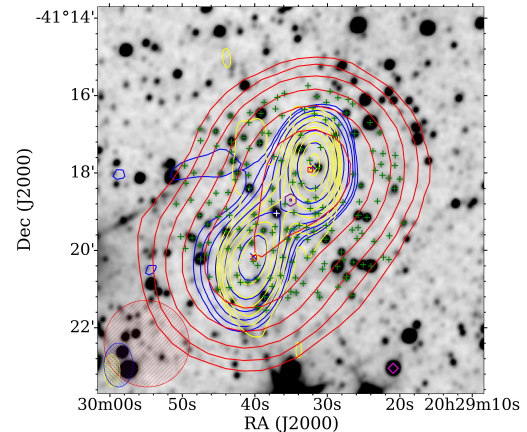


Figure 1. An example overlay showing how different sets of radio contours (GLEAM [200 MHz] in red, SUMSS [843 MHz] in blue, and TGSS [150 MHz] in yellow) were used to assess the morphology of a G4Jy source (G4Jy 1628), with the respective beam-sizes of the different radio surveys shown in the bottom left-hand corner. The underlying, inverted-greyscale image is from the W1 band of AllWISE, with green pluses ('+') marking AllWISE catalogue positions within 3 arcmin of the radio-centroid position (purple hexagon). This enabled White et al. (2020b,a) to identify the appropriate host galaxy of the radio emission (white '+'), which was followed by thorough checks against published studies before being included the G4Jy catalogue.

tects sources that are present along the 2-arcsec-width longslit of the RSS, uses data from the intervening regions for sky subtraction, and performs stacking of spectra from multiple exposures.

3. Results and discussion

The (homogenised, SuperCOSMOS-scale) R -band magnitudes that informed our observations are shown in Figure 2(a). This dataset not only aids redshift determination but also provides further understanding of host-galaxy properties, which are essential for understanding the role of AGN in galaxy evolution. 124 of the 586 G4Jy sources belong to the G4Jy-3CRE subset (Massaro et al., 2023a), and 429 G4Jy sources have a (less than) 1-arcsec crossmatch with DR4 of the SkyMapper survey (Onken et al., 2024)^d. We note that the application of an $R = 20.0$ mag cut to the homogenised magnitudes corresponds to an $r \simeq 21.0$ limit in the SkyMapper-PSF magnitudes. A scatter-plot comparison of the magnitudes is shown in Figure 2(b), and indicates that there is a large degree of scatter, irrespective of source brightness. As such, our multsemester campaign needed to be extended so that underexposed host-galaxies could be reobserved (in order to achieve better signal-to-noise ratios). This is crucial as it facilitates the determination of redshifts for a larger sample of radio sources, which is essential for understanding their evolution and the environments that they inhabit.

^bThese 586 targets include 124 of the 264 G4Jy sources belonging to the G4Jy-3CRE subset (Section 1).

^c<https://github.com/mattyowl/RSSMOSPipeline>

^dEarlier data releases were not of the required optical depth for obtaining a large fraction of crossmatches with the G4Jy Sample (White et al., 2020b,a).

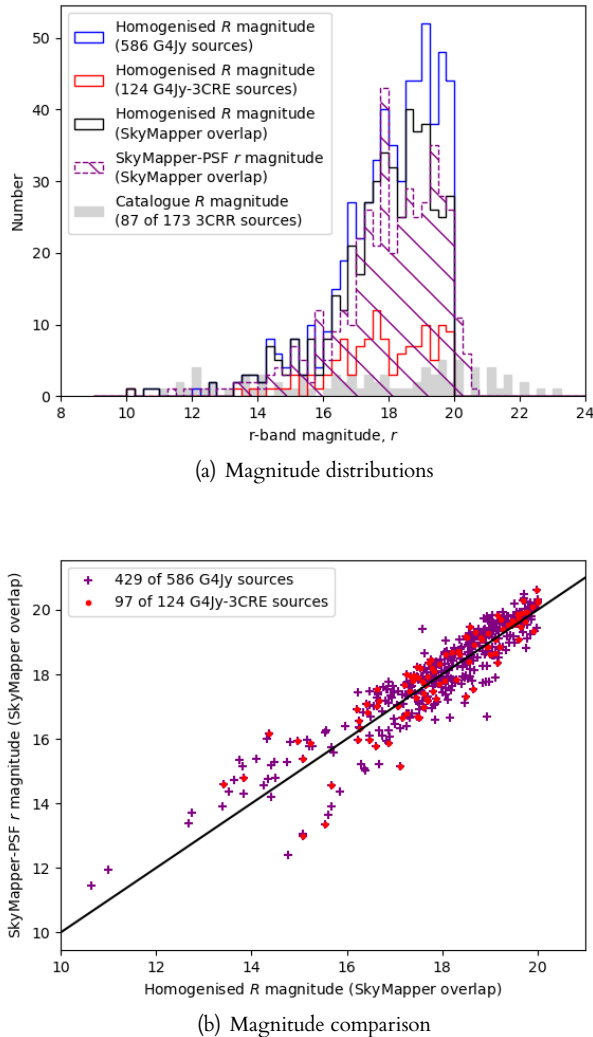


Figure 2. (a) Distributions of the R -band magnitudes (Section 2) for different subsets of the G4Jy Sample ($-76^\circ < \text{Dec.} < 11^\circ$, restricted to $R \sim 20$), with the magnitude distribution for 3CRR sources (without restriction) added for comparison (grey histogram). “Homogenised” refers to magnitudes from different surveys being put on the SuperCOSMOS scale (Hambly et al., 2001), and “SkyMapper overlap” refers to the 429 G4Jy-on-SALT targets that appear in the SkyMapper survey. (b) A comparison of the SkyMapper-PSF r -magnitude with the homogenised R -band magnitude for the G4Jy targets that appear in the SkyMapper survey (purple ‘+’). Sources that also belong to the G4Jy-3CRE subset (Massaro et al., 2023a) are indicated by red dots.

3.1 SALT spectra

The first batch of 42 G4Jy sources that already have good signal-to-noise ratios for deriving redshifts are shown in Figure 8, with the redshifts obtained being summarised in Table 2. Twenty-six of the sources listed belong to the G4Jy-3CRE subset, and so supplement the 42 (entirely-new) redshifts obtained by García-Pérez et al. (2024) and via ongoing observing campaigns. In addition, we note that six of the observations presented here are made possible by the host-galaxy positions determined through MeerKAT imaging (Sejake et al., 2023).

If the target spectrum is dominated by emission lines, then we attempt to fit it with a “quasar” template^e; if, instead, absorption lines dominate the spectrum, then we employ an “early-type galaxy” template^f (Yip et al., 2004). In sources that appear to have an even mixture of emission- and absorption-lines, we fit the target spectrum with a “galaxy” template that incorporates (for example) both a strong $\text{H}\alpha$ emission-line and the Calcium-II H+K doublet^e. As a reminder, the aim is to obtain redshifts rather than complete emission-/absorption-line characterisation (for which flux calibration would be needed). The error in the redshift is estimated by applying lower and upper limits to the template, and seeing (by eye) how well-aligned the spectral features remain. Such template-shifting allows us to get an idea of the ‘tolerance’ of the fit, and also encompasses any error in the wavelength calibration (which is usually $< 1 \text{ \AA}$).

Like Mauch & Sadler (2007), we see a mixture of emission-line (‘e’), absorption-line (‘a’), and absorption-/emission-line (‘ae’) spectra, and no correspondence between r -band magnitude and the spectroscopic redshift (Table 2). However, we note that the brightness of emission lines allows for the redshift to be more-readily determined than via fitting absorption lines (which are more difficult to differentiate from a noisy continuum), and therefore our first set of results are biased towards the former spectral-type. For the interested reader, Sejake et al. (in prep.) will present the relative fractions for a more-completely-defined subsample of G4Jy sources.

3.2 Comments on individual sources

G4Jy 530, G4Jy 590, and G4Jy 1819 overlap with the sources analysed by García-Pérez et al. (2024). Our redshifts are in agreement for G4Jy 530 and G4Jy 1819, but differ for G4Jy 590 (where they estimate the redshift as $z = 0.5384 \pm 0.0027$). Following correspondence with the authors, we provide the corrected spectroscopic-redshift of $z = 0.529 \pm 0.002$, in disagreement with the photometric redshift ($z = 0.58$) provided by Burgess & Hunstead (2006).

The largest redshift error in the present work is for G4Jy 541 ($z = 0.200 \pm 0.007$), on account of the CaII H+K doublet being tentatively detected (towards the edge of the wavelength coverage) in addition to strong [OIII] emission-lines. We

^eThis template was provided courtesy of P.C. Hewett, and is for a ‘pure quasar’, with no host-galaxy contribution towards the emission. A refined version of the quasar template, and a link to Python code, is now available in Temple et al. (2021).

^f<https://classic.sdss.org/dr5/algorithms/spectemplates/>

Table 2. Spectroscopic redshifts for 42 G4Jy sources, as determined via SALT optical-spectroscopy (Appendix 2). Sources belonging to the G4Jy-3CRE subset (Massaro et al., 2023a) and the MeerKAT-2019 subset (Seijake et al., 2023) are indicated with a flag of ‘1’ in the respective columns. The point-spread function (PSF) r -band magnitude provided via DR4 of SkyMapper (Onken et al., 2024) is also presented, where available. The night of observation is given in the format of YYYY-MM-DD.

Source name	G4Jy-3CRE subset	MeerkAT-2019 subset	RA. (h:m:s, J2000)	Host-galaxy Dec. (d:m:s, J2000)	SuperCOSMOS r -band magnitude	SkyMapper PSF r -band magnitude	Night of observation	Spectral type	Spectroscopic redshift
G4Jy 43	1	0	00:23:08.86	-25:02:29.6	19.78	19.9458 ± 0.2633	2023-08-06	absorption-line	0.354 ± 0.001
G4Jy 45	1	0	00:24:30.15	-29:23:54.3	17.65	17.6794 ± 0.0249	2021-09-08	emission-line	0.407 ± 0.002
G4Jy 98	0	0	00:54:08.43	-03:33:55.2	17.81	17.9300 ± 0.0774	2021-11-18	emission-line	0.211 ± 0.001
G4Jy 172	0	0	01:33:33.18	-44:44:17.7	16.56	17.0252 ± 0.1376	2021-07-23	emission-line	0.091 ± 0.003
G4Jy 192	1	0	01:50:35.94	-29:31:55.3	19.16	19.8300 ± 0.0378	2020-10-24	emission-line	0.413 ± 0.003
G4Jy 373	1	0	03:38:46.01	-35:22:52.0	17.58	17.7767 ± 0.0676	2020-12-28	emission-line	0.113 ± 0.001
G4Jy 492	1	0	04:44:37.70	-28:09:54.3	16.67	17.1836 ± 0.0837	2021-08-25	emission-line	0.148 ± 0.001
G4Jy 530	1	1	05:12:47.41	-48:24:16.5	18.37	18.6866 ± 0.2019	2022-02-13	emission-line	0.305 ± 0.002
G4Jy 541	0	0	05:23:20.72	-48:16:30.6	17.35	17.8014 ± 0.0524	2024-03-19	emission-line	0.200 ± 0.007
G4Jy 590	1	0	06:03:12.22	-34:26:32.6	19.97	20.6115 ± 0.2703	2022-08-27	emission-line	0.529 ± 0.002
G4Jy 604	0	0	06:18:13.03	-48:44:58.3	14.35	14.7611 ± 0.1184	2021-12-19	absorption-line	0.049 ± 0.003
G4Jy 611	1	1	06:26:20.46	-53:41:35.1	17.21	14.6096 ± 0.1107	2021-11-18	absorption-line	0.055 ± 0.001
G4Jy 641	0	1	07:05:32.94	-45:13:08.8	17.62	18.0829 ± 0.1151	2023-11-24	emission-line	0.128 ± 0.002
G4Jy 672	1	1	07:43:31.61	-67:26:25.5	16.18	16.3000 ± 0.0233	2022-11-07	emission-line	1.510 ± 0.001
G4Jy 692	0	0	08:15:27.81	-03:08:26.6	16.65	17.4301 ± 0.1780	2021-11-18	absorption-line	0.198 ± 0.001
G4Jy 706	1	0	08:27:17.41	-20:26:24.8	17.70	17.1893 ± 0.0446	2021-01-25	emission-line	0.828 ± 0.004
G4Jy 901	0	1	11:11:19.43	-40:30:51.9	19.18	17.8111 ± 0.0852	2024-03-19	emission-line	0.725 ± 0.002
G4Jy 909	0	0	11:18:26.95	-46:34:14.9	17.52	17.0930 ± 0.0098	2024-03-13	emission-line	0.714 ± 0.001
G4Jy 957	1	0	11:49:06.68	-12:04:33.4	16.62	17.5547 ± 0.0843	2022-06-02	absorption-/emission-line	0.119 ± 0.002
G4Jy 965	1	0	11:54:21.78	-35:05:29.0	17.83	18.1017 ± 0.0637	2021-05-25	emission-line	0.258 ± 0.001
G4Jy 1112	0	0	14:02:31.57	+02:15:46.5	17.16	17.3919 ± 0.0666	2022-04-19	emission-line	0.180 ± 0.003
G4Jy 1135	1	0	14:16:33.15	-36:40:53.7	16.22	16.9136 ± 0.1238	2021-07-25	emission-line	0.075 ± 0.001
G4Jy 1157	1	0	14:24:16.47	-38:26:47.6	16.92	–	2021-08-22	emission-line	0.406 ± 0.001
G4Jy 1203	1	0	14:54:28.22	-36:40:04.7	19.37	19.5418 ± 0.1037	2021-06-11	emission-line	0.420 ± 0.001
G4Jy 1306	0	0	16:06:12.69	+00:00:27.2	15.16	15.9605 ± 0.1408	2022-04-21	absorption-line	0.058 ± 0.001
G4Jy 1343	1	0	16:31:41.60	-26:56:51.3	18.96	18.8668 ± 0.1255	2023-05-01	emission-line	0.168 ± 0.001
G4Jy 1364	0	0	16:45:42.39	+02:11:45.0	16.25	16.3795 ± 0.1673	2022-04-21	absorption-/emission-line	0.094 ± 0.001
G4Jy 1487	1	0	18:30:58.92	-36:02:30.7	16.24	15.9748 ± 0.1575	2021-07-24	emission-line	0.078 ± 0.001
G4Jy 1511	1	0	18:57:10.80	-30:19:40.1	17.94	17.7130 ± 0.0215	2020-09-15	emission-line	1.554 ± 0.003
G4Jy 1518	1	1	19:15:48.68	-26:52:57.4	18.94	18.3254 ± 0.1774	2024-04-04	absorption-/emission-line	0.231 ± 0.003
G4Jy 1555	1	0	19:33:25.00	-39:40:20.7	15.09	15.3791 ± 0.1508	2021-06-20	absorption-line	0.074 ± 0.001
G4Jy 1565	1	0	19:41:15.02	-15:24:31.2	19.91	19.3288 ± 0.0846	2020-10-14	emission-line	0.454 ± 0.001
G4Jy 1581	0	0	19:52:15.79	+02:30:24.1	15.68	15.7368 ± 0.1094	2021-08-29	absorption-/emission-line	0.059 ± 0.001
G4Jy 1660	0	0	20:52:02.35	-57:04:07.5	12.01	–	2022-05-14	absorption-/emission-line	0.012 ± 0.001

Table 2. *Continued* – Spectroscopic redshifts for 42 G4Jy sources, as determined via SALT optical-spectroscopy (Appendix 2).

Source name	G4Jy-3CRE subset	MeerKAT-2019 subset	Host-galaxy R.A. (h:m:s, J2000)	Host-galaxy Dec. (d:m:s, J2000)	SuperCOSMOS R-band magnitude	SkyMapper PSF r-band magnitude	Night of observation	Spectral type	Spectroscopic redshift
G4Jy 1665	0	0	20:56:16.36	-47:14:47.6	18.48	17.1078 ± 0.0525	2021-08-04	emission-line	1.488 ± 0.003
G4Jy 1698	1	0	21:31:01.47	-20:36:56.1	19.54	19.5835 ± 0.0954	2020-10-12	emission-line	1.630 ± 0.002
G4Jy 1704	0	0	21:34:06.70	-53:34:18.7	14.49	15.2795 ± 0.1473	2022-05-14	absorption-line	0.078 ± 0.001
G4Jy 1705	0	0	21:34:17.69	-53:38:11.1	14.28	–	2021-08-29	absorption-line	0.076 ± 0.002
G4Jy 1709	1	0	21:37:50.00	-20:42:31.7	19.61	19.7336 ± 0.0280	2022-05-24	emission-line	0.638 ± 0.004
G4Jy 1781	1	0	22:29:18.63	-40:51:32.8	19.11	19.0730 ± 0.0298	2023-11-10	emission-line	0.448 ± 0.002
G4Jy 1795	1	0	22:53:03.11	-40:57:46.7	18.49	19.1680 ± 0.1630	2020-12-02	emission-line	0.307 ± 0.003
G4Jy 1819	1	0	23:19:56.26	-27:28:07.4	16.68	–	2022-11-07	emission-line	0.174 ± 0.001

note that there are not emission lines in the template that align with the distinctive peaks at $\sim 6650\text{\AA}$ and $\sim 6825\text{\AA}$, but caution that the target's continuum is affected by suboptimal sky-background subtraction.

The ‘double’ radio morphologies of G4Jy 1704 and G4Jy 1705 were first published by White et al. (2020a,b), based on the PhD thesis of Haigh (2001), and show extended emission within the Abell-3785 cluster. They are referred to as “the dancing ghosts” by Norris et al. (2021) and Velović et al. (2023), who present ASKAP and MeerKAT imaging of these radio sources, respectively. Our spectroscopic redshifts are in agreement with the photometric redshifts previously acquired (Bilicki et al., 2014), with G4Jy 1704 at $z = 0.078 \pm 0.001$ and G4Jy 1705 at $z = 0.076 \pm 0.002$. These values were determined via fitting their SALT spectra with an “early-type galaxy” template, as shown in Figure 8.

Within the SALT spectra we identify the MgII emission-line for 8 of the 42 sources, these being: G4Jy 672, G4Jy 706, G4Jy 901, G4Jy 909, G4Jy 1511, G4Jy 1665, G4Jy 1698, and G4Jy 1709. This is of special interest for follow-up, as the black-hole mass can be estimated via measuring the linewidth of this line (e.g. McLure & Jarvis, 2002).

We recheck how many G4Jy sources have spectra in SDSS (Appendix 3), and find that 53 overlap with SDSS DR16 (Ahumada et al., 2020), which includes 36 that have had their SDSS-DR12 entries updated. We retain the remaining ($104 - 36 = 68$) SDSS-DR12 sources (Alam et al., 2015) that are cross-identified with the G4Jy Sample, and combine these with the 136 redshifts from 6dFGS (Jones et al., 2009). The redshift distributions of these different datasets are shown in Figure 3.

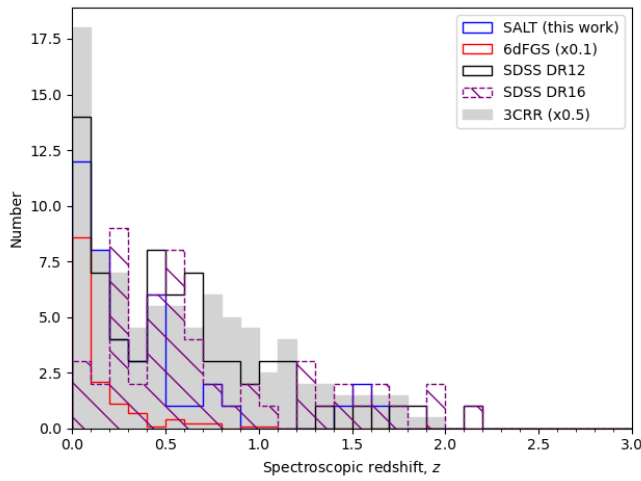


Figure 3. Distributions of the redshifts (Section 3.2) for different subsets of the G4Jy Sample (with no restrictions based on Declination). The redshift distribution for 3CRR sources (Laing et al., 1983) is added for comparison (grey histogram, scaled by 0.5), and the 6dFGS distribution has been scaled by 0.1.

The highest of these redshifts is $z = 2.17827 \pm 0.00015$ from SDSS DR12, which is corroborated by Hewett & Wild (2010), who measure $z = 2.17920 \pm 0.00055$. The G4Jy overlay for this source, G4Jy 1065 (also known as 4C+11.45), is shown

in Figure 4. The large MWA beam means that the GLEAM contours are affected by confusion with a nearby unrelated source towards the southwest, whilst the TGSS contours show extended radio morphology at 150 MHz. The latter (‘double’ morphology) was first presented by Barthel et al. (1988) in a VLA map at 5 GHz.

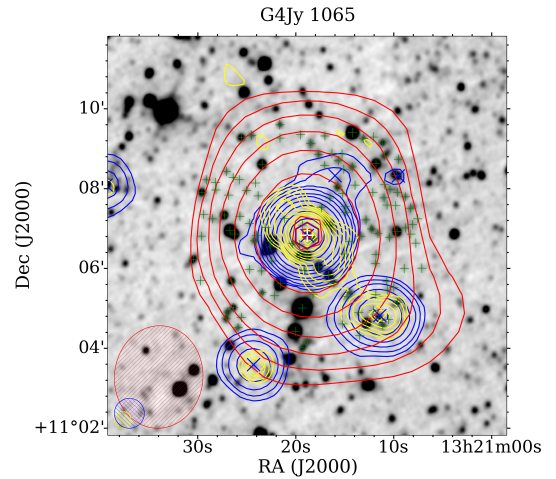


Figure 4. Radio contours (GLEAM [200 MHz] in red, NVSS [1400 MHz] in blue, and TGSS [150 MHz] in yellow) for G4Jy 1065, with the respective beam-sizes of the different radio surveys shown in the bottom left-hand corner. The inverted-greyscale image is from the W1 band of AllWISE, with green pluses (+) marking AllWISE catalogue positions within 3 arcmin of the radio-centroid position (purple hexagon). The host galaxy of the radio emission is indicated by a white '+', in close alignment with the radio positions from the different radio surveys (a red square, a blue 'x', and a yellow diamond, respectively).

3.3 Intrinsic radio properties

The combination of SALT, 6dFGS, and SDSS redshifts allows us to calculate intrinsic radio-properties for a sample of 299 G4Jy sources. For this work, we focus on radio luminosities (based upon measurements at 151 MHz) and projected linear-sizes (based upon angular sizes determined through NVSS and SUMSS catalogue positions, at 1.4 GHz and 843 MHz, respectively; see section 6.3.1 by White et al. 2020a). These values are provided in Table 3 (Appendix 3). We note that 49 sources do not have spectral indices because the G4Jy flux-densities (20 measurements across 72 to 231 MHz, provided in the G4Jy catalogue) are not well-fit by a power-law function ($S \propto \nu^\alpha$, where α is the spectral index within the GLEAM band). As a result, we do not calculate their radio luminosities for Figure 5. This is because these luminosities are K-corrected, *assuming* a power-law description of the radio emission. Future work will present the broadband spectra of these sources, which show significant spectral curvature in the radio (White et al., in prep.).

In order to compare the G4Jy Sample with 3CRR (Laing et al., 1983), we scale the 178-MHz radio-luminosities to 151-MHz radio-luminosities for the 3CRR sources (with the spectral index, α , taken from the 3CRR catalogue). We remind the reader that the G4Jy (sub-)sample is not spectroscopically-complete yet, but it is encouraging that new redshifts from

SALT are already enabling us to probe a wide parameter space in luminosity (Figure 5). The five G4Jy sources with the highest luminosities, above $1.4 \times 10^{29} \text{ W Hz}^{-1}$, are: G4Jy 1511 (SALT, $z = 1.554 \pm 0.003$), G4Jy 1698 (SALT, $z = 1.630 \pm 0.002$), G4Jy 845 (re-fitted $z = 1.706 \pm 0.001$; see Figure 10), G4Jy 1065 (SDSS DR12, $z = 2.17827 \pm 0.00015$), and G4Jy 682 (SDSS DR16, $z = 1.96818 \pm 0.00016$). Joining the most-powerful ($\gtrsim 10^{29} \text{ W Hz}^{-1}$) radio-galaxies in the Universe (e.g. Laing et al., 1983; Saxena et al., 2018; Capetti & Balmaverde, 2024), we anticipate that the G4Jy Sample will allow more-robust comparisons with cosmological and galaxy-evolution simulations, for a range of redshifts and environments.

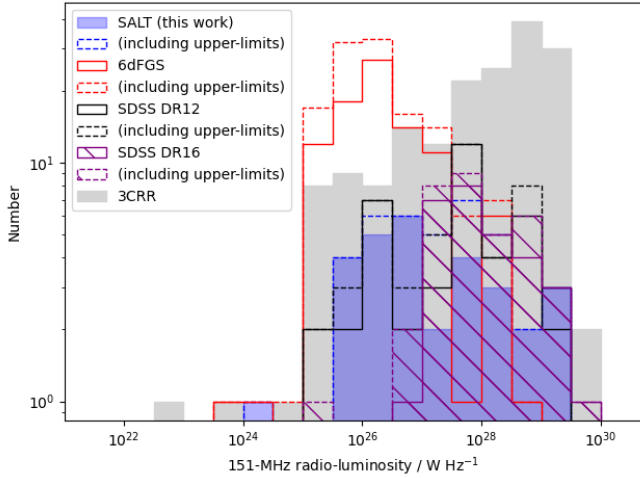


Figure 5. Distributions of the 151-MHz radio-luminosities (Section 3.3) for different subsets of the G4Jy Sample (with no restrictions based on Declination). The luminosity distribution for 3CRR sources (Laing et al., 1983) is added for comparison (grey histogram).

Connected to the gas-density distribution of the environment is the linear extent of the radio emission associated with a particular host galaxy. Of course, the 2-dimensional imaging of radio sources means that we can only calculate the projected linear size, when going from the observed frame to the intrinsic frame. As such, all linear sizes are (in effect) lower limits, but for this work we treat these sizes as absolute values (see Figure 6). We also present the linear-size distributions when upper limits are included (dashed-line histograms in Figure 6). These correspond to G4Jy sources that are either unresolved in NVSS/SUMSS imaging or have radio emission at 151 MHz that is blended with an unrelated radio-source. (The former are indicated via an inequality sign, ' $<$ ', associated with the angular size in the G4Jy catalogue, and the latter are assigned a 'Confusion flag' of '1'; Table 3.)

Again, the linear sizes of 3CRR sources are added for comparison, with these values being obtained from the online 3CRR database^g. However, they are derived from radio maps at a range of frequencies (typically 1.4 GHz to 8 GHz) and so the linear sizes will be connected to the different spatial resolutions (and sensitivity to different angular-scales) that are

^g<https://3crr.extragalactic.info/cgi/database?1=on&2=on&3=on&4=on&5=on&6=on&12=on&13=on>

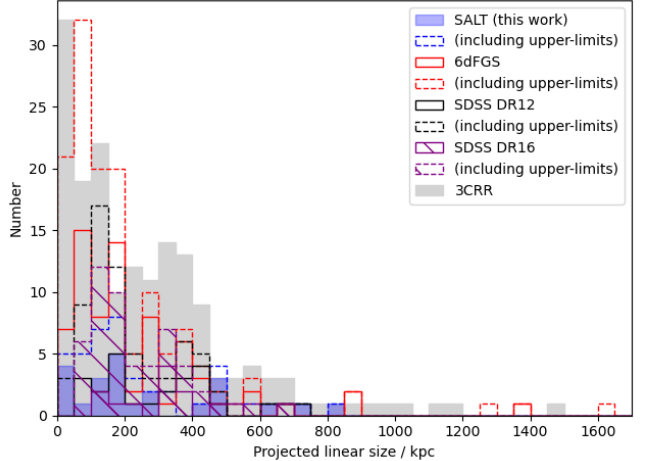


Figure 6. Distributions of the (projected) linear sizes (Section 3.3) for different subsets of the G4Jy Sample (with no restrictions based on Declination). The size distribution for 3CRR sources (Laing et al., 1983) is added for comparison (grey histogram), with three of these sources (NGC 6251, 3C 326 = G4Jy 1282, and 3C 236) having linear sizes that are beyond the plot range (i.e. 1900 kpc to 4530 kpc).

involved. Our linear sizes (for the G4Jy Sample) are more-consistent in that they are from a homogeneous dataset; NVSS or SUMSS, both of which are at 45-arcsec resolution. Either way, another caveat to add, regarding both the G4Jy Sample and the 3CRR sample, is that the linear-size values will be lower limits for FRI ('centre-brightened') sources and better estimates for FRII ('edge-brightened') sources (Fanaroff & Riley, 1974). The scope of this work can be extended to consider FRI and FRII sources separately, once a survey of the entire G4Jy Sample is completed at $\lesssim 10$ arcsec resolution (allowing such a morphology classification to be performed).

Like White et al. (2020b), we follow Willis & Strom (1978) in defining a giant radio galaxy (GRG) as having a projected, linear size of > 1 Mpc. Amongst the 299 G4Jy sources analysed in this work are three GRGs: G4Jy 1079 (1.271 Mpc), G4Jy 133 (1.388 Mpc), and G4Jy 517 (1.620 Mpc). However, the existence of 6dFGS spectra (Jones et al., 2009) means that these are already-known GRGs, as noted in section 4.8 of White et al. (2020b). If we instead relax the size threshold (for defining a GRG) to 0.7 Mpc (e.g. Malarecki et al., 2013; Oei et al., 2023), then we can identify G4Jy 1665 (SALT, $z = 1.488 \pm 0.003$), G4Jy 1173 (SDSS DR12, $z = 0.05509 \pm 0.00001$), G4Jy 604 (SALT, $z = 0.049 \pm 0.003$), G4Jy 619 (6dFGS, $z = 0.05501$), and G4Jy 1741 (6dFGS, $z = 0.14519$) as additional sources belonging to this category of radio galaxy.

Of these, G4Jy 604 is a *new* GRG, with a linear size of 0.846 Mpc. Its absorption-line optical spectrum (Figure 8) may explain why, despite its 6-Jy brightness at 151 MHz, it has not been previously classified as a GRG. Meanwhile, G4Jy 1173 is noted by Oei et al. (2023) as a GRG in the LOw-Frequency ARray (LOFAR) Two-metre Sky Survey (LoTSS), and G4Jy 1741 is recorded in the Rapid ASKAP Continuum Survey (RACS) by Andernach et al. (2021). As for G4Jy 619 (aka PKS B0634-205), its giant size has been known since the

work of Danziger et al. (1978).

For further interest, in Figure 7 we present the 151-MHz radio-luminosity against the linear size. It is thought that extended radio-galaxies follow evolutionary tracks across this plane, in what is effectively a power-size (P - D) diagram (Baldwin, 1982), but this is complicated by various factors, such as: (i) the impact of the environment on the radio morphology (e.g. Vardoulaki et al., 2024), (ii) the strength of magnetic fields (e.g. Miley, 1980; Jamrozy et al., 2004) in and around the radio galaxy (through its connection to the radio luminosity), (iii) the impact of viewing angle on the observed brightness of the radio emission (although this is ameliorated by the *low-frequency* selection for the G4Jy Sample; Barthel 1989), (iv) assumptions made about the duty cycle of the AGN (e.g. Turner, 2018), and (v) how quickly hotspots advance through the intergalactic medium (Alexander & Leahy, 1987). We refer the reader to figure 8 of Hardcastle et al. (2019) and the discussion therein for further details. It is expected that as we gather more redshifts for the G4Jy Sample, we will populate a greater area of the P - D diagram, with follow-up observations (such as those studying X-rays and polarisation) allowing us to break the degeneracy of some of the aforementioned factors.

For now, we note that the G4Jy Sample shows a similar spread in radio luminosity and linear size as the 3CRR sample (Figure 7). The lack of a G4Jy source larger than 1620 kpc (Figure 6) may be a combined effect of current incompleteness of the spectroscopic follow-up, and the relative shallowness of existing optical data (resulting in a bias towards the small volume of the local Universe). We also emphasise that the linear sizes are limited by the 45-arcsec resolution of the SUMSS/NVSS imaging. Combined with the Malmquist bias towards higher radio-luminosities at higher redshifts, this could explain the clustering (and positive trend) of linear-size upper-limits at $L_{151 \text{ MHz}} \gtrsim 10^{27} \text{ W Hz}^{-1}$. This is because the upper limit of the linear size will become more discrepant with increasing redshift for unresolved sources (in a given radio survey). We conclude with a note that this is being addressed via improved angular sizes for the full sample (White et al., in prep.).

4. Summary

Our ongoing observing campaign with SALT is to obtain optical spectroscopy (PI: White) for a complete sample (SuperCOSMOS $R2 \lesssim 20.0$) of powerful radio-galaxies from the G4Jy Sample (White et al., 2020a,b), which are selected at low radio-frequencies and distributed over the entire southern sky. This enables accurate redshift measurements, with new spectra presented in this paper (for 42 G4Jy sources; Figure 8) and as part of a larger data release (Sejake et al., in prep.). We also refit the spectra for five G4Jy sources that appear in SDSS (Alam et al., 2015; Ahumada et al., 2020), and present the corrected redshifts in Appendix 3.

For an initial analysis of 299 G4Jy sources, we combine SALT redshifts with those from 6dFGS (Jones et al., 2009) and SDSS, and find that the sample spans a wide range in radio luminosities ($L_{151 \text{ MHz}} = 5.7 \times 10^{23} - 3.5 \times 10^{29} \text{ W Hz}^{-1}$) and linear sizes (1–1620 kpc). We expect that the lower flux-density

threshold for the G4Jy Sample ($S_{151 \text{ MHz}} > 4.0 \text{ Jy}$), compared to the famous 3CRR sample ($S_{178 \text{ MHz}} > 10.9 \text{ Jy}$), will allow us to better-populate the radio-power-physical-size (P - D diagram; Figure 7) and conduct more-detailed investigations of how radio-loud AGN evolve, over a larger fraction of the Universe's history^h.

The redshift information collated from multiple sources will also enable us to address several key questions on the interaction of AGN with their environment, without the orientation bias that affects both AGN samples selected at high radio-frequencies (due to relativistic beaming) and those selected in the optical (caused by dust obscuration). Furthermore, the spectroscopy will form a valuable *legacy multiwavelength dataset* for future detailed active-galaxy studies. This is because it addresses a critical gap in prior work on powerful AGN in the southern sky, aiding research with facilities like the Square Kilometre Array (SKA) and its precursor telescopes.

Funding Statement This work is based on the research supported in part by the National Research Foundation of South Africa (Grant Number 151060). The financial assistance of the South African Radio Astronomy Observatory (SARAO) towards this research is also hereby acknowledged.

Acknowledgements The observations reported in this paper were obtained with the Southern African Large Telescope (SALT), under program 2020-1-MLT-008 (PI: White). We thank Christian Hettlage for his expertise with SALT schedule-blocks; Lucia Marchetti, Mattia Vaccari, and the SALT Team for helpful comments on the proposal; Christopher White for help with the SALT Finder Charts; and Dan Smith for support. We also thank the anonymous reader for their comments, which improved the scope of the paper, and both Martin Hardcastle and the anonymous referee, regarding the luminosities.

The national facility capability for SkyMapper has been funded through ARC LIEF grant LE130100104 from the Australian Research Council, awarded to the University of Sydney, the Australian National University, Swinburne University of Technology, the University of Queensland, the University of Western Australia, the University of Melbourne, Curtin University of Technology, Monash University and the Australian Astronomical Observatory. SkyMapper is owned and operated by The Australian National University's Research School of Astronomy and Astrophysics. The survey data were processed and provided by the SkyMapper Team at ANU. The SkyMapper node of the All-Sky Virtual Observatory (ASVO) is hosted at the National Computational Infrastructure (NCI). Development and support of the SkyMapper node of the ASVO has been funded in part by Astronomy Australia Limited (AAL) and the Australian Government through the Commonwealth's Education Investment Fund (EIF) and National Collaborative Research Infrastructure Strategy (NCRIS), particularly

^hSDSS DR12 (Alam et al., 2015) provides the highest redshift for the G4Jy Sample *so far* (geddit?), at $z = 2.17827 \pm 0.00015$ (for G4Jy 1065), whilst 3C9 has the highest redshift in the 3CRR sample (Laing et al., 1983), at $z = 2.012$. See Bridle et al. (1994) for a deep, 5-GHz VLA map of the latter.

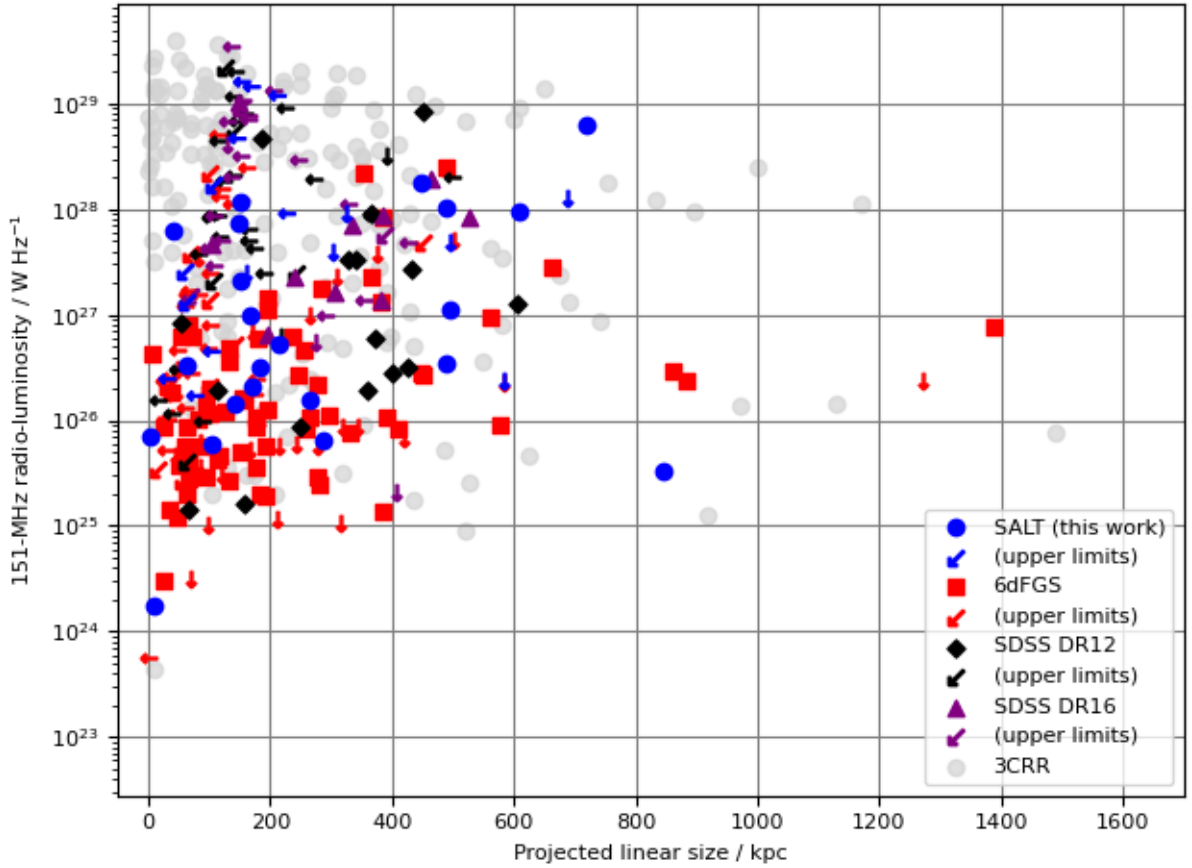


Figure 7. The distribution of 151-MHz radio-luminosities against the (projected) linear sizes of the G4Jy Sample (Section 3.3), with no restrictions based on Declination. Each set of “upper limits” is with respect to the linear-size value and/or the radio luminosity. Upper limits in the linear size are represented by horizontal arrows, and are the result of the angular size of the source being an upper limit (due to the resolution of SUMSS/NVSS imaging). Vertical arrows represent upper limits in the radio luminosity, which are a consequence of the 151-MHz flux-density being affected by blended emission from unrelated radio sources. (The affected G4Jy sources are demarcated via a ‘confusion flag’ of ‘1’.) Meanwhile, diagonal arrows are used when both the linear size and the radio luminosity are upper limits. The distribution for 3CRR sources (Laing et al., 1983) is added for comparison (grey circles), with three of these sources (NGC 6251, 3C 326 = G4Jy 1282, and 3C 236) having linear sizes that are beyond the plot range (at 1900 kpc to 4530 kpc). In addition, 49 G4Jy sources do not appear in this figure on account of their lack of a spectral-index fit (White et al., 2020a). (This is required for appropriate K-correction of the radio luminosity.)

Table 4. SDSS spectroscopic redshifts for five G4Jy sources, with new redshifts presented as a result of re-fitting the target spectrum (Appendix 3 and Figure 10). The ‘SDSS best-fit’ values are where the reduced- χ^2 metric is the global minimum (per source). Each of the sources listed are quasars.

Source name	Redshift origin	SDSS objID	SDSS best-fit redshift	Alternative SDSS redshift	Reduced- χ^2 ranking	Re-fitted redshift (this work)
G4Jy 148	SDSS DR16	1237679323928789061	2.78413 ± 0.00024	1.97376 ± 0.00034	2nd	1.965 ± 0.005
G4Jy 176	SDSS DR16	1237666274203271475	1.68729 ± 0.00086	1.63661 ± 0.00034	5th	1.660 ± 0.005
G4Jy 679	SDSS DR12	1237667254525952687	0.24639 ± 0.00010	1.19644 ± 0.00060	6th	1.196 ± 0.001
G4Jy 845	SDSS DR12	1237658423552376915	2.46126 ± 0.00015	1.71835 ± 0.00016	4th	1.706 ± 0.001
G4Jy 1240	SDSS DR12	1237667967497077036	5.49964 ± 0.00032	0.58067 ± 0.00005	3rd	0.581 ± 0.001

the National eResearch Collaboration Tools and Resources (NeCTAR) and the Australian National Data Service Projects (ANDS).

Funding for the Sloan Digital Sky Survey IV has been provided by the Alfred P. Sloan Foundation, the U.S. Department of Energy Office of Science, and the Participating Institutions. SDSS-IV acknowledges support and resources from the Center for High Performance Computing at the University of Utah. The SDSS website is www.sdss.org. SDSS-IV is managed by the Astrophysical Research Consortium for the Participating Institutions of the SDSS Collaboration including the Brazilian Participation Group, the Carnegie Institution for Science, Carnegie Mellon University, Center for Astrophysics | Harvard & Smithsonian, the Chilean Participation Group, the French Participation Group, Instituto de Astrofísica de Canarias, The Johns Hopkins University, Kavli Institute for the Physics and Mathematics of the Universe (IPMU) / University of Tokyo, the Korean Participation Group, Lawrence Berkeley National Laboratory, Leibniz Institut für Astrophysik Potsdam (AIP), Max-Planck-Institut für Astronomie (MPIA Heidelberg), Max-Planck-Institut für Astrophysik (MPA Garching), Max-Planck-Institut für Extraterrestrische Physik (MPE), National Astronomical Observatories of China, New Mexico State University, New York University, University of Notre Dame, Observatório Nacional / MCTI, The Ohio State University, Pennsylvania State University, Shanghai Astronomical Observatory, United Kingdom Participation Group, Universidad Nacional Autónoma de México, University of Arizona, University of Colorado Boulder, University of Oxford, University of Portsmouth, University of Utah, University of Virginia, University of Washington, University of Wisconsin, Vanderbilt University, and Yale University.

Competing Interests

None.

Data Availability Statement The DOI for the SkyMapper DR4 release is 10.25914/5M47-S621, and the SALT spectra will be made available through the Zenodo repository for the G4Jy Sample: <https://zenodo.org/communities/g4jy/>.

Ethical Standards The research meets all ethical guidelines, including adherence to the legal requirements of the study country.

References

- Ahumada, R., Allende Prieto, C., Almeida, A., et al. 2020, ApJS, 249, 3
- Alam, S., Albareti, F. D., Allende Prieto, C., et al. 2015, ApJS, 219, 12
- Alexander, P., & Leahy, J. P. 1987, MNRAS, 225, 1
- Andernach, H., Jiménez-Andrade, E. F., & Willis, A. G. 2021, Galaxies, 9, 99
- Baldwin, J. E. 1982, in IAU Symposium, Vol. 97, Extragalactic Radio Sources, ed. D. S. Heeschen & C. M. Wade, 21–24
- Barthel, P. D. 1989, ApJ, 336, 606
- Barthel, P. D., Miley, G. K., Schilizzi, R. T., & Lonsdale, C. J. 1988, A&AS, 73, 515
- Bennett, A. S. 1962, MmRAS, 68, 163
- Bessell, M., Bloxham, G., Schmidt, B., et al. 2011, PASP, 123, 789
- Best, P. N., & Heckman, T. M. 2012, MNRAS, 421, 1569
- Bilicki, M., Jarrett, T. H., Peacock, J. A., Cluver, M. E., & Steward, L. 2014, ApJS, 210, 9
- Bolton, A. S., Schlegel, D. J., Aubourg, É., et al. 2012, AJ, 144, 144
- Bridle, A. H., Hough, D. H., Lonsdale, C. J., Burns, J. O., & Laing, R. A. 1994, AJ, 108, 766
- Burgess, A. M., & Hunstead, R. W. 2006, AJ, 131, 114
- Capetti, A., & Balmaverde, B. 2024, A&A, 689, A174
- Collier, J. D., Banfield, J. K., Norris, R. P., et al. 2014, MNRAS, 439, 545
- Condon, J. J., Cotton, W. D., Greisen, E. W., et al. 1998, AJ, 115, 1693
- Croton, D. J., Springel, V., White, S. D. M., et al. 2006, MNRAS, 365, 11
- Cutri, R. M., Wright, E. L., Conrow, T., et al. 2013, Explanatory Supplement to the AllWISE Data Release Products, Explanatory Supplement to the AllWISE Data Release Products, by R. M. Cutri et al.
- Danziger, I. J., Goss, W. M., & Frater, R. H. 1978, MNRAS, 184, 341
- Davies, J. J., Crain, R. A., Oppenheimer, B. D., & Schaye, J. 2020, MNRAS, 491, 4462
- Dey, A., Schlegel, D. J., Lang, D., et al. 2019, AJ, 157, 168
- Fanaroff, B. L., & Riley, J. M. 1974, MNRAS, 167, 31P
- Flewelling, H. A., Magnier, E. A., Chambers, K. C., et al. 2020, ApJS, 251, 7
- García-Pérez, A., Peña-Herazo, H. A., Jimenez-Gallardo, A., et al. 2024, ApJS, 271, 8
- Gendre, M. A., & Wall, J. V. 2008, MNRAS, 390, 819
- Grasha, K., Darling, J., Bolatto, A., Leroy, A. K., & Stocke, J. T. 2019, ApJS, 245, 3
- Haigh, A. J. 2001, PhD thesis, University of Sydney, Australia
- Hambly, N. C., MacGillivray, H. T., Read, M. A., et al. 2001, MNRAS, 326, 1279
- Hardcastle, M. J., Williams, W. L., Best, P. N., et al. 2019, A&A, 622, A12
- Hewett, P. C., & Wild, V. 2010, MNRAS, 405, 2302
- Hilton, M., Hasselfield, M., Sifón, C., et al. 2018, ApJS, 235, 20
- Hlavacek-Larrondo, J., McDonald, M., Benson, B. A., et al. 2015, ApJ, 805, 35
- Hurley-Walker, N., Callingham, J. R., Hancock, P. J., et al. 2017, MNRAS, 464, 1146
- Intema, H. T., Jagannathan, P., Mooley, K. P., & Frail, D. A. 2017, A&A, 598, A78
- Ishibashi, W., & Fabian, A. C. 2012, MNRAS, 427, 2998
- Jamrozy, M., Klein, U., Mack, K. H., Gregorini, L., & Parma, P. 2004, A&A, 427, 79
- Jones, D. H., Read, M. A., Saunders, W., et al. 2009, MNRAS, 399, 683
- Kuijken, K., Heymans, C., Hildebrandt, H., et al. 2015, MNRAS, 454, 3500
- Laing, R. A., Riley, J. M., & Longair, M. S. 1983, MNRAS, 204, 151
- Lammers, C., Iyer, K. G., Ibarra-Medel, H., et al. 2023, ApJ, 953, 26
- Lister, M. L. 2003, ApJ, 599, 105
- Malarecki, J. M., Staveley-Smith, L., Saripalli, L., et al. 2013, MNRAS, 432, 200
- Massaro, F., White, S. V., García-Pérez, A., et al. 2023a, ApJS, 265, 32
- Massaro, F., White, S. V., Paggi, A., et al. 2023b, ApJS, 268, 32
- Mauch, T., Murphy, T., Buttery, H. J., et al. 2003, MNRAS, 342, 1117
- Mauch, T., & Sadler, E. M. 2007, MNRAS, 375, 931
- McLure, R. J., & Jarvis, M. J. 2002, MNRAS, 337, 109
- Miley, G. 1980, ARA&A, 18, 165
- Mullin, L. M., Riley, J. M., & Hardcastle, M. J. 2008, MNRAS, 390, 595
- Murphy, T., Mauch, T., Green, A., et al. 2007, MNRAS, 382, 382
- Nidever, D. L., Dey, A., Olsen, K., et al. 2018, AJ, 156, 131
- Norris, R. P., Marvil, J., Collier, J. D., et al. 2021, PASA, 38, e046
- Oei, M. S. S. L., van Weeren, R. J., Gast, A. R. D. J. G. I. B., et al. 2023, A&A, 672, A163
- Onken, C. A., Wolf, C., Bessell, M. S., et al. 2024, PASA, 41, e061
- Osmer, P. S., Porter, A. C., & Green, R. F. 1994, ApJ, 436, 678
- Rees, M. J. 1966, Nature, 211, 468
- Robotham, A. S. G., Davies, L. J. M., Driver, S. P., et al. 2018, MNRAS, 476, 3137

- Roger, R. S., Costain, C. H., & Bridle, A. H. 1973, AJ, 78, 1030
 Saxena, A., Marinello, M., Overzier, R. A., et al. 2018, MNRAS, 480, 2733
 Sejake, P. K., White, S. V., Heywood, I., et al. 2023, MNRAS, 518, 4290
 Shabala, S. S., Jurlin, N., Morganti, R., et al. 2020, MNRAS, 496, 1706
 Silk, J. 2013, ApJ, 772, 112
 Singh, V., Beelen, A., Wadadekar, Y., et al. 2014, A&A, 569, A52
 Smith, K. L., Shields, G. A., Bonning, E. W., et al. 2010, ApJ, 716, 866
 Spinrad, H., Djorgovski, S., Marr, J., & Aguilar, L. 1985, PASP, 97, 932
 Steidel, C. C., & Sargent, W. L. W. 1991, ApJ, 382, 433
 Temple, M. J., Hewett, P. C., & Banerji, M. 2021, MNRAS, 508, 737
 Tingay, S. J., Goeke, R., Bowman, J. D., et al. 2013, PASA, 30, e007
 Tonry, J. L., Stubbs, C. W., Lykke, K. R., et al. 2012, ApJ, 750, 99
 Turner, R. J. 2018, MNRAS, 476, 2522
 Vardoulaki, E., Backöfer, V., Finoguenov, A., et al. 2024, arXiv e-prints, arXiv:2412.01795
 Velović, V., Cotton, W. D., Filipović, M. D., et al. 2023, MNRAS, 523, 1933
 Venemans, B. P., Röttgering, H. J. A., Miley, G. K., et al. 2007, A&A, 461, 823
 Wang, Y., & Kaiser, C. R. 2008, MNRAS, 388, 677
 White, S. V., Franzen, T. M. O., Wong, O. I., et al. 2018, arXiv e-prints, arXiv:1810.01226
 White, S. V., Franzen, T. M. O., Riseley, C. J., et al. 2020a, PASA, 37, e018
 —. 2020b, PASA, 37, e017
 Willis, A. G., & Strom, R. G. 1978, A&A, 62, 375
 Wolf, C., Onken, C. A., Luvaal, L. C., et al. 2018, PASA, 35, e010
 Wylezalek, D., Galametz, A., Stern, D., et al. 2013, ApJ, 769, 79
 Yao, S., Wu, X.-B., Ai, Y. L., et al. 2019, ApJS, 240, 6
 Yip, C. W., Connolly, A. J., Szalay, A. S., et al. 2004, AJ, 128, 585

Appendix 1. Collating *R*-band magnitudes

We collated magnitudes for the (cross-identified) G4Jy sources, as observed in the following filters by various surveys:

- the *R*2 filter for SuperCOSMOSⁱ (Hambly et al., 2001),
- the *r* filter for the National Optical Astronomy Observatory (NOAO) Source Catalog (NSC)^j DR1 (Nidever et al., 2018),
- the *r* filter for the Dark Energy Spectroscopic Instrument (DESI) Legacy Imaging Surveys (LS)^k DR8 (Dey et al., 2019),
- the *r* filter for SDSS DR12 (Alam et al., 2015),
- the Petrosian *r* filter^l (Bessell et al., 2011) for SkyMapper (SM) DR1.1 (Wolf et al., 2018),
- the *r* filter^m (Tonry et al., 2012) for PanSTARRS (PS; Flewelling et al., 2020),
- and Visual Survey Telescope *r*-band photometry (Kuijken et al., 2015), newly-extracted using ProFound (PF; Robotham et al., 2018).

The greatest coverage was provided by SuperCOSMOS (i.e. $\sim 64\%$ of the 586 G4Jy targets), and so this magnitude scale was chosen to be the ‘anchor’ to which the other magnitudes

ⁱ<http://ssa.roe.ac.uk/dboverview.html>

^j<https://datalab.noirlab.edu/nscdr1/index.php>

^k<https://www.legacysurvey.org>

^l<https://datalab.noirlab.edu/skymapper.php>

^m<https://outerspace.stsci.edu/display/PANSTARRS/PS1+Filter+properties#PS1Filterproperties-Filterdescriptions>

were ‘homogenised’. This was done by applying the following $y = mx + c$ equations (based upon linear-regression analysis), as appropriate:

$$r_{\text{NSC}}^{R2} = (r_{\text{NSC}} - c_{\text{NSC}}^{R2})/m_{\text{NSC}}^{R2} = (r_{\text{NSC}} + 0.493)/1.022 \quad (1)$$

$$r_{\text{LS}}^{R2} = (r_{\text{LS}} - c_{\text{LS}}^{R2})/m_{\text{LS}}^{R2} = (r_{\text{LS}} + 0.729)/1.029 \quad (2)$$

$$r_{\text{SDSS}}^{R2} = (r_{\text{SDSS}} - c_{\text{SDSS}}^{R2})/m_{\text{SDSS}}^{R2} = (r_{\text{SDSS}} + 1.349)/1.067 \quad (3)$$

$$r_{\text{SM}}^{R2} = (r_{\text{SM}} - c_{\text{SM}}^{R2})/m_{\text{SM}}^{R2} = (r_{\text{SM}} - 2.600)/0.845 \quad (4)$$

$$r_{\text{PS}}^{R2} = (r_{\text{PS}} - c_{\text{PS}}^{R2})/m_{\text{PS}}^{R2} = (r_{\text{PS}} - 2.908)/0.866 \quad (5)$$

$$r_{\text{PF}}^{R2} = (r_{\text{PF}} - c_{\text{PF}}^{R2})/m_{\text{PF}}^{R2} = (r_{\text{PF}} + 0.254)/1.001 \quad (6)$$

Appendix 2. SALT spectra and Finder Charts

Within Figure 8, we present optical spectra for 42 G4Jy sources (White et al., 2020a,b), including those that belong to the G4Jy-3CRE subset (Massaro et al., 2023a) and optical spectra for “the dancing ghosts”, G4Jy 1704 and G4Jy 1705.

The corresponding Finder Charts are shown in Figure 9, for reference, by way of corroborating the host-galaxy position used for optical follow-up. Note that, for G4Jy 1511, Massaro et al. (2023a) suggest that the AllWISE identification for the host galaxy (White et al., 2020a,b) is ‘confused’ with a (much fainter) optical source nearby. For our observation, SALT is pointed at the optical source that coincides with the AllWISE position (which has ObjectID = 229802842 within SkyMapper DR4ⁿ).

Additional spectra will be provided to the community as part of a SALT data release that focuses on G4Jy sources at $-40^\circ < \text{Dec.} < -10^\circ$ (Sejake et al., in prep.).

Appendix 3. Redshifts and radio properties

Table 3 presents observed and *intrinsic* radio properties for 299 G4Jy sources, having collated their redshifts from SALT proposal 2020-1-MLT-008 (PI: White, this work), 6dFGS (Jones et al., 2009), SDSS DR12 (Alam et al., 2015), and SDSS DR16 (Ahumada et al., 2020). We visually-inspect all of the spectra and find that five sources have incorrect redshifts in the SDSS database, mainly on account of emission lines being misidentified. The better fittings of these spectra, and the corrected redshifts, are shown in Figure 10 and summarised in Table 4.

In the case of G4Jy 148, the peak emission from the presence of CIV was mislabelled as Lyman- α , whilst the prominent emission of CIII] and MgII went unlabelled. By re-fitting the spectrum (still with a quasar template) we determine a redshift

ⁿ<https://skymapper.anu.edu.au/object-viewer/dr4/229802842/>

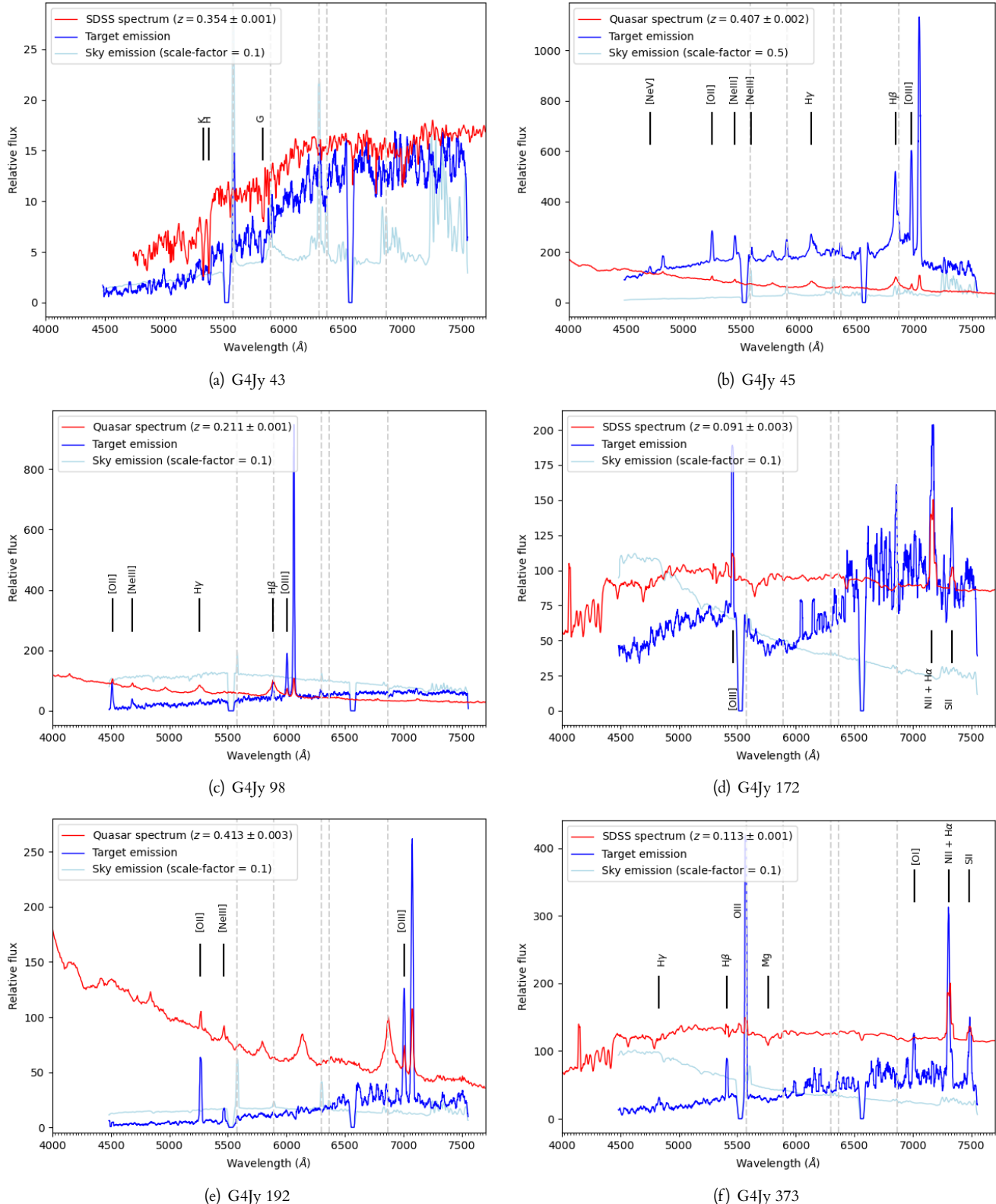


Figure 8. SALT spectra (blue lines) of G4Jy sources (Section 3 and Appendix 2). CCD chip-gaps are indicated by the blue line dropping to zero relative-flux, whilst the sky-emission spectra are represented by lighter-blue lines. (The latter is scaled to aid comparison with the target emission, and the scale factor that has been applied is noted in each legend.) The dashed, grey, vertical lines indicate the sky-emission that is used to assess the accuracy of the wavelength calibration, and the target spectrum is fitted with the appropriate template spectrum (red line; Section 3).

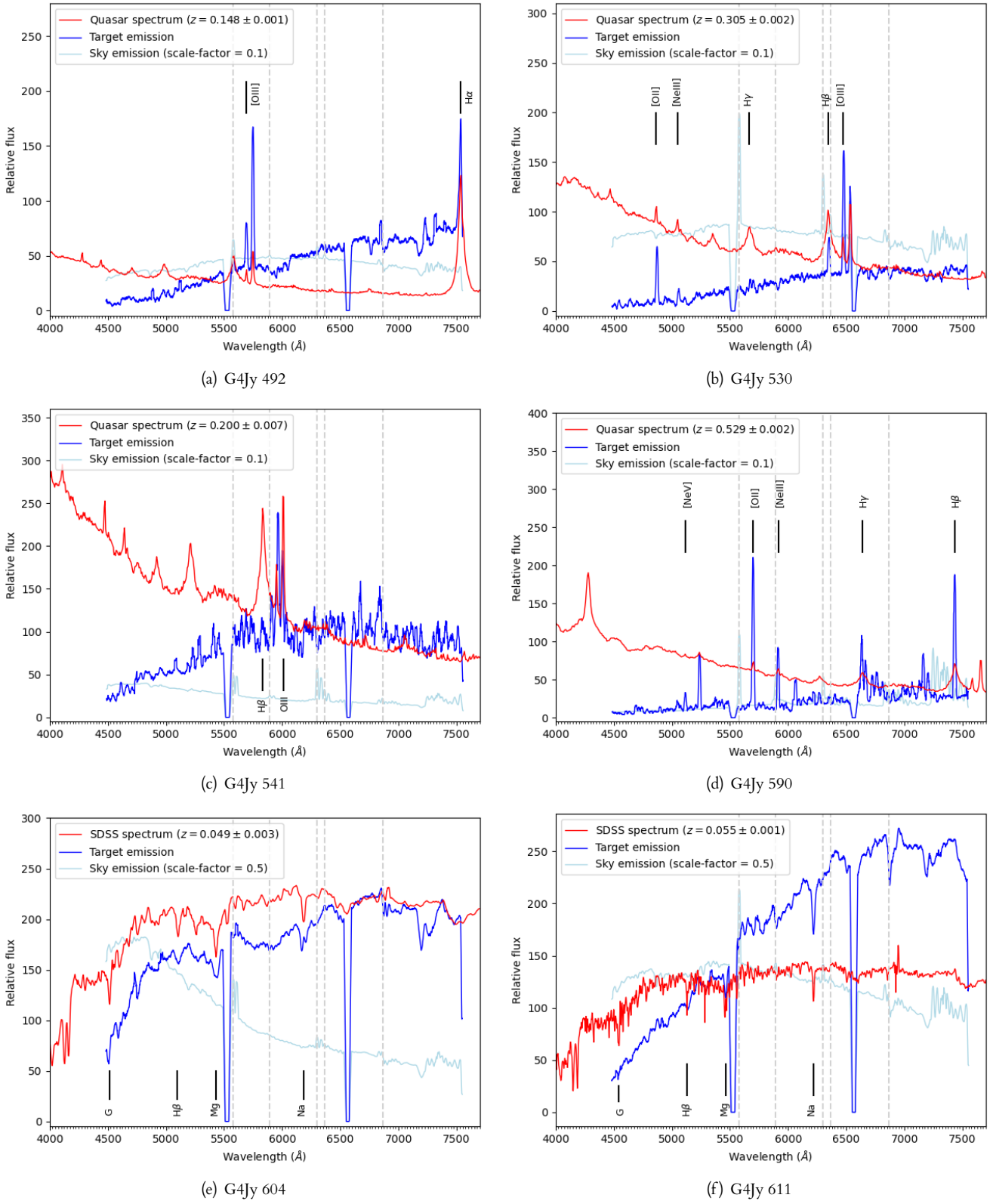


Figure 8. *Continued* – SALT spectra of G4Jy sources (Section 3 and Appendix 2).

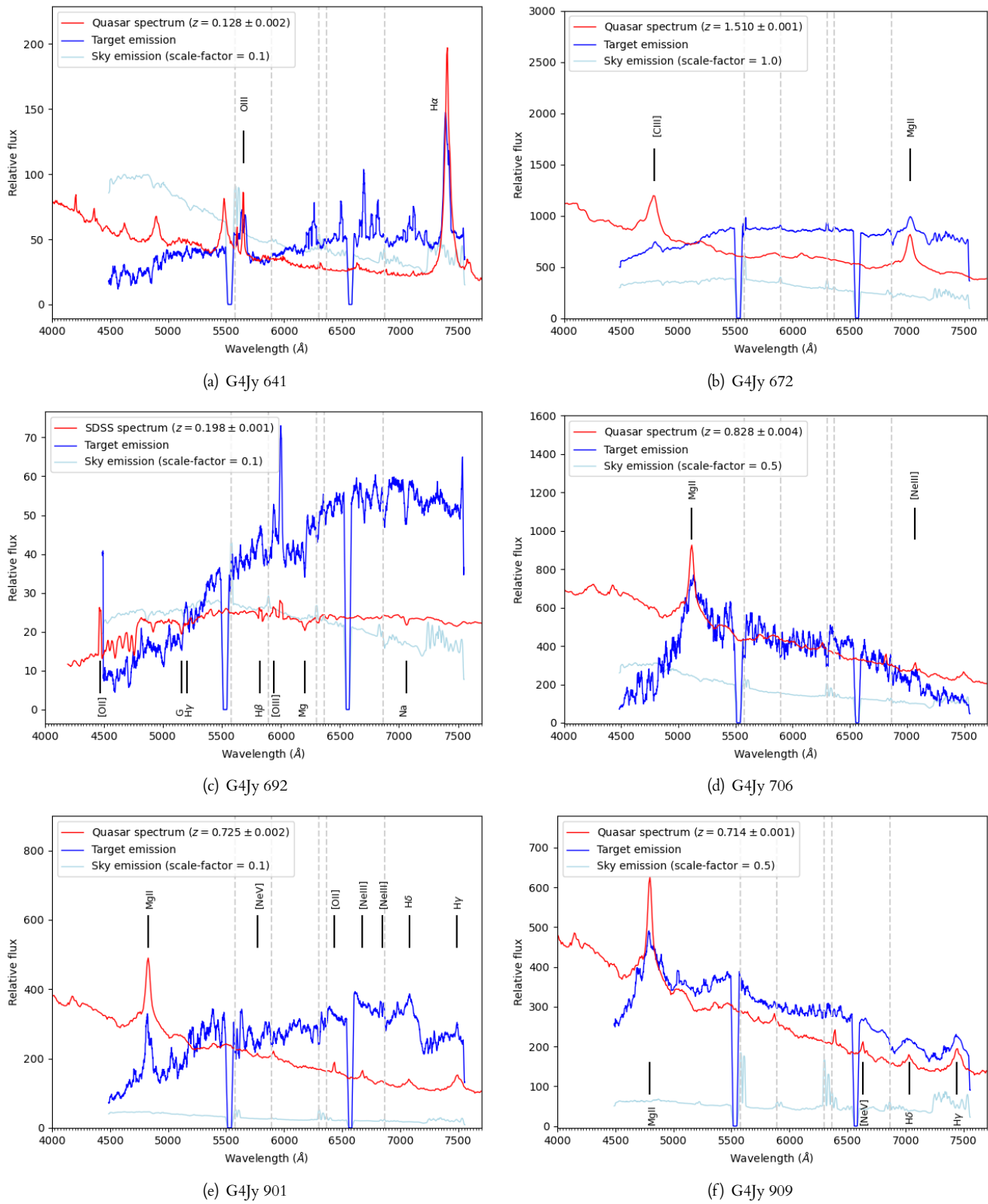


Figure 8. Continued – SALT spectra of G4Jy sources (Section 3 and Appendix 2).

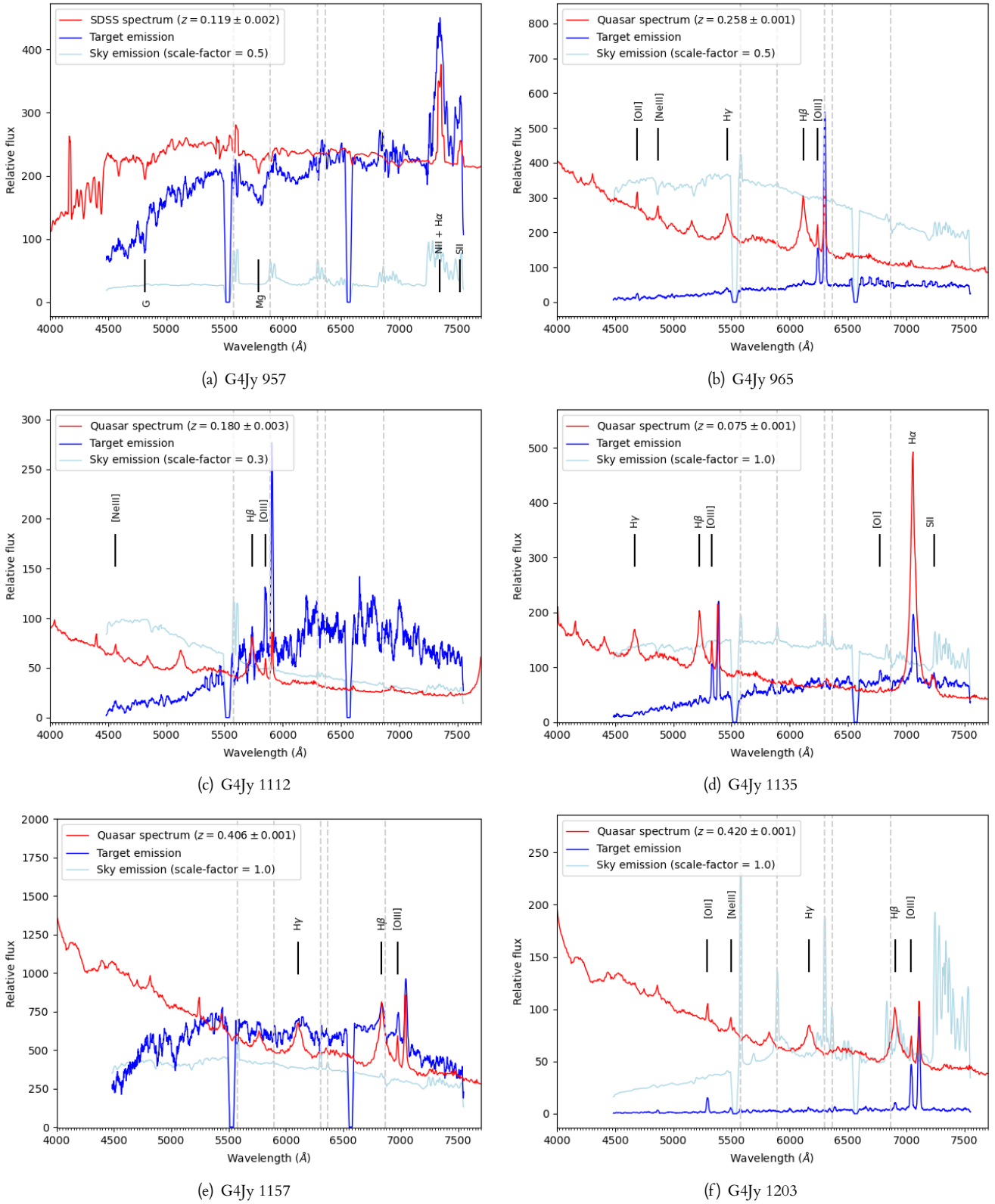


Figure 8. *Continued* – SALT spectra of G4Jy sources (Section 3 and Appendix 2).

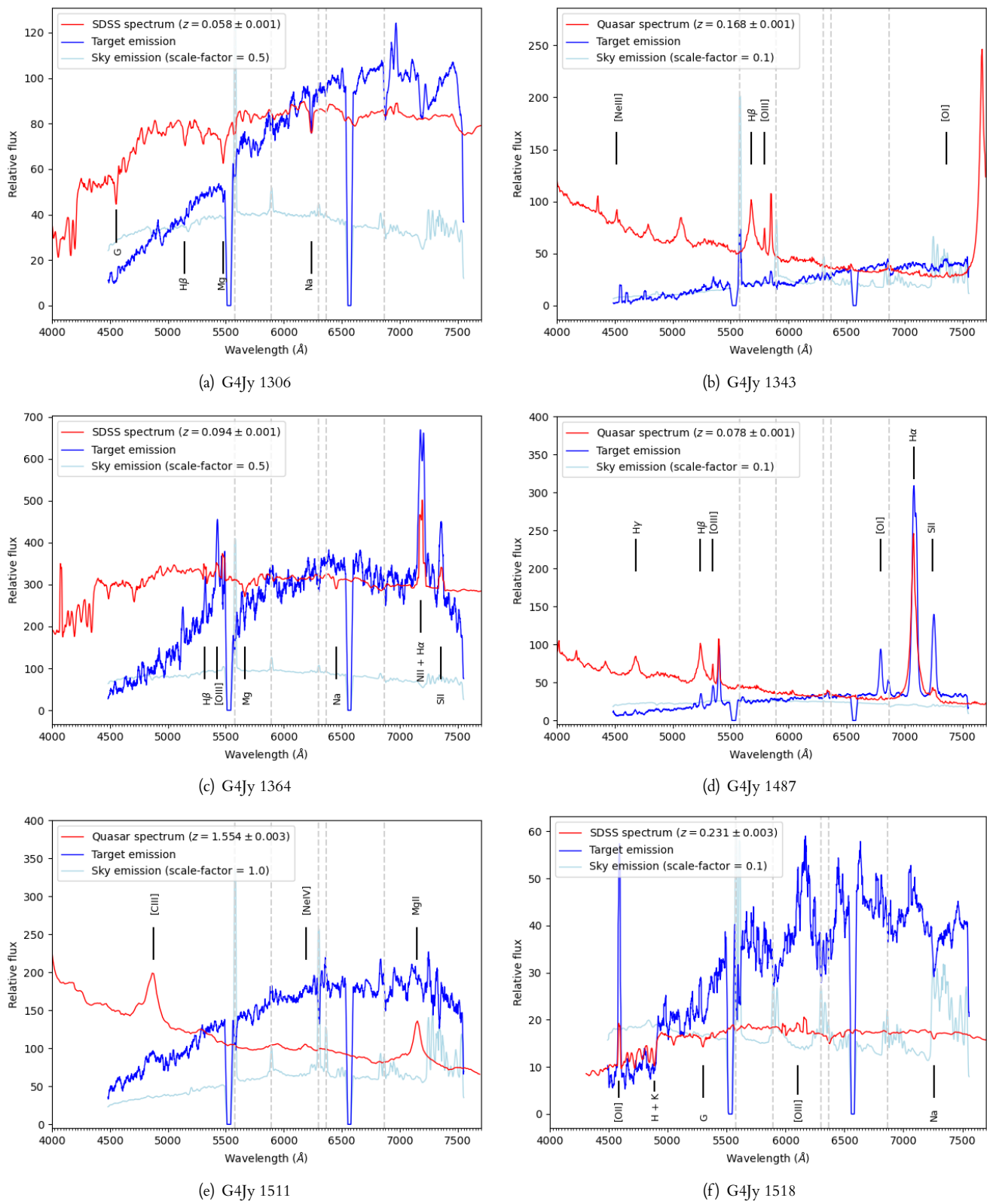


Figure 8. Continued – SALT spectra of G4Jy sources (Section 3 and Appendix 2).

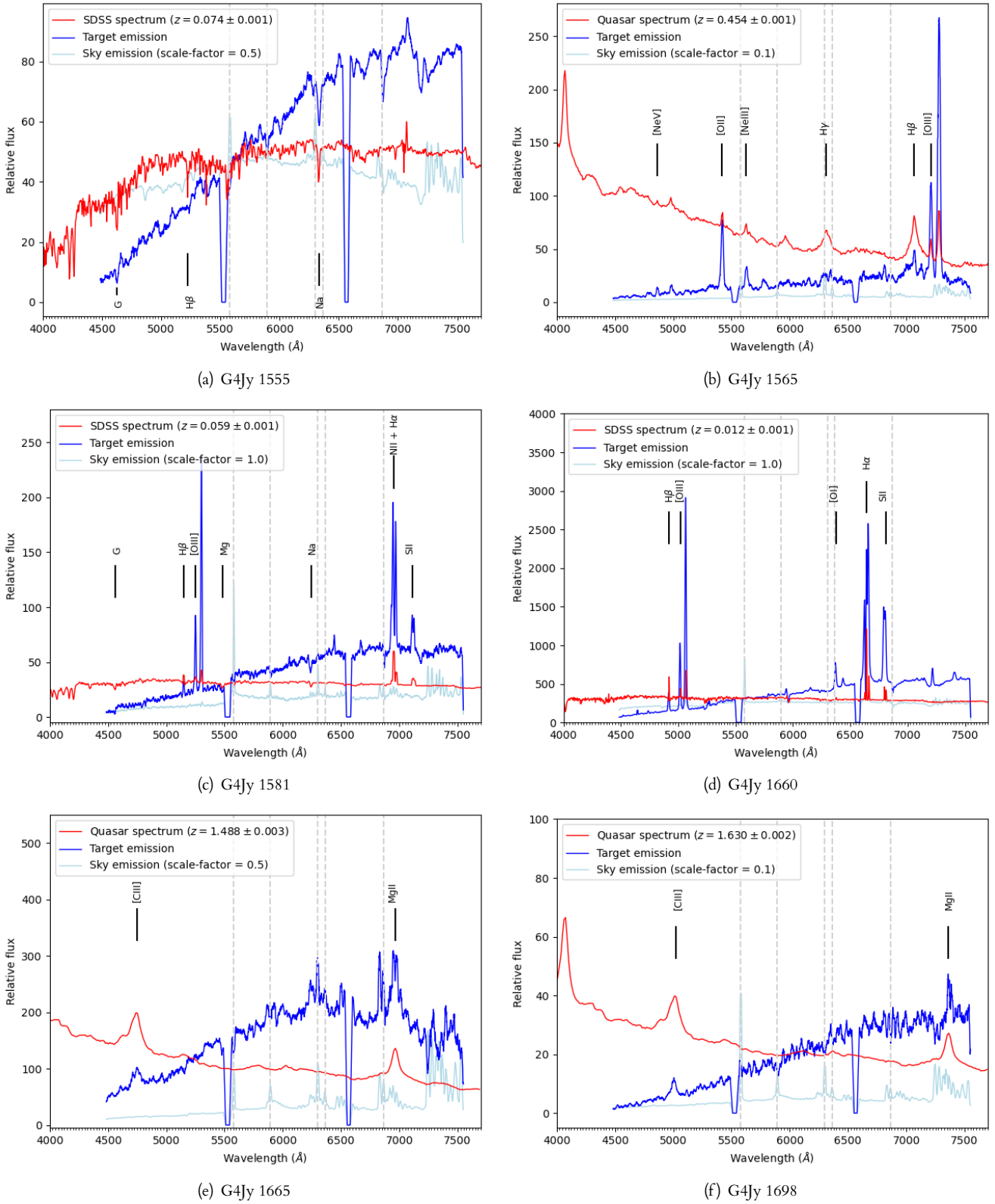


Figure 8. *Continued* – SALT spectra of G4Jy sources (Section 3 and Appendix 2).

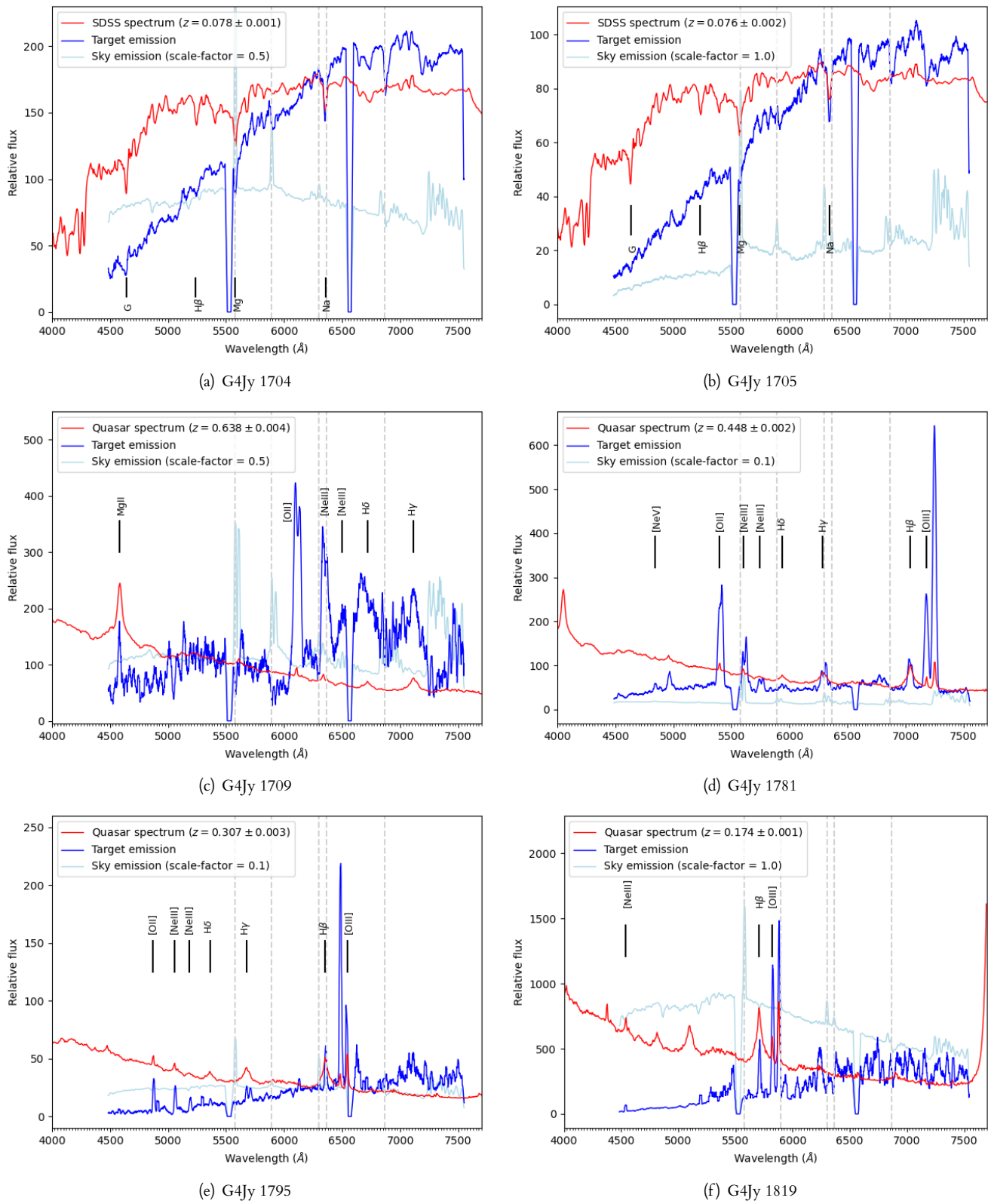
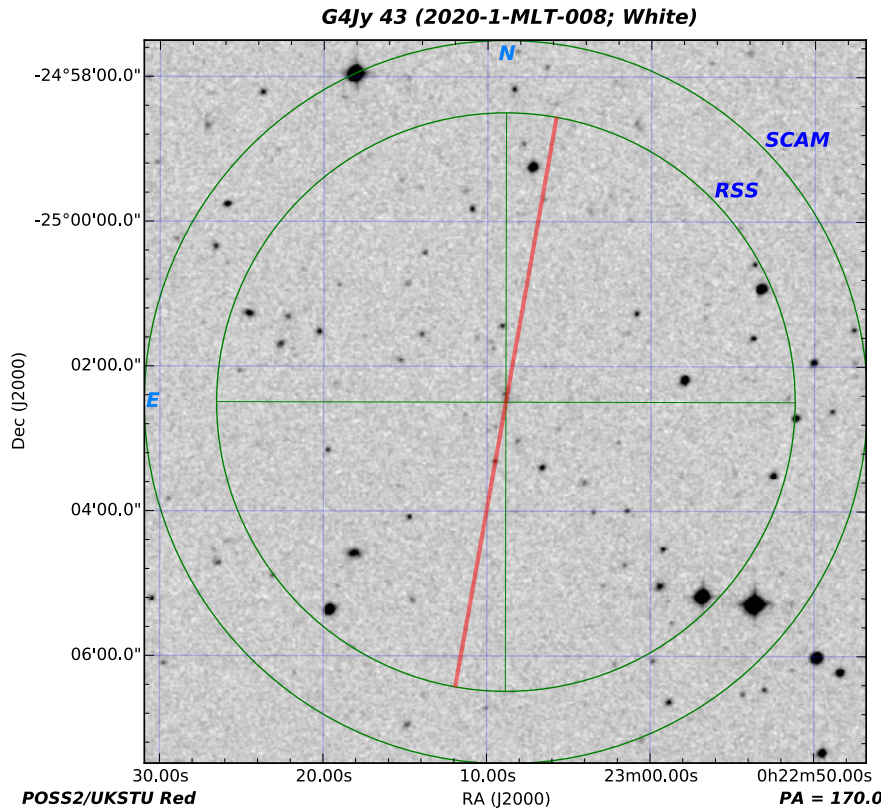
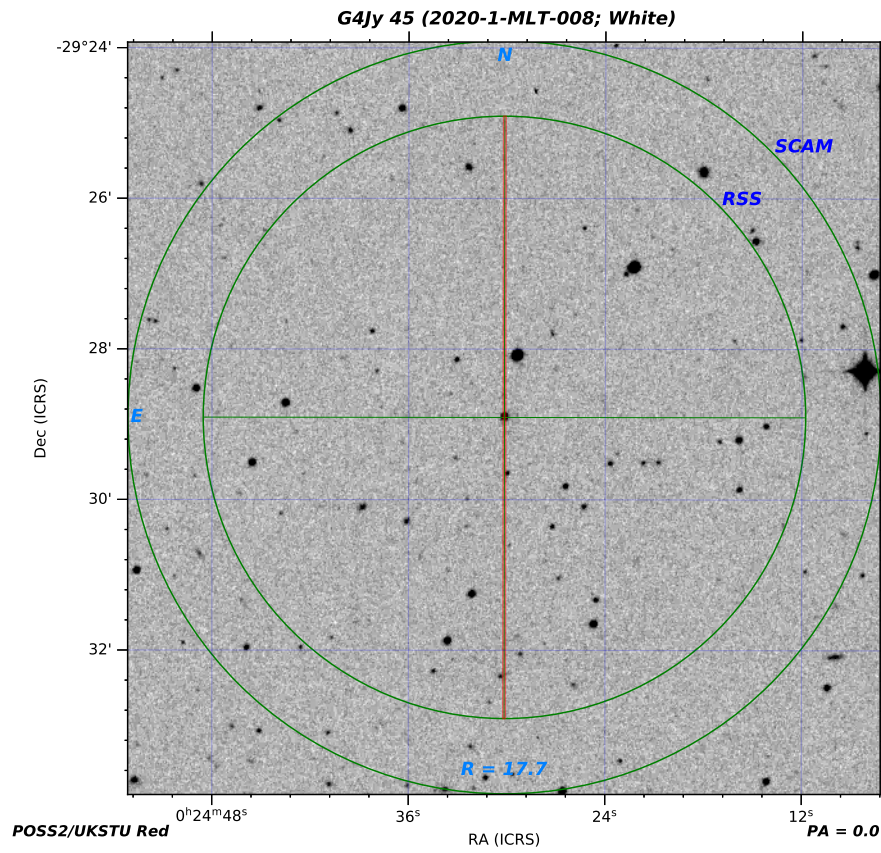


Figure 8. Continued – SALT spectra of G4Jy sources (Section 3 and Appendix 2).

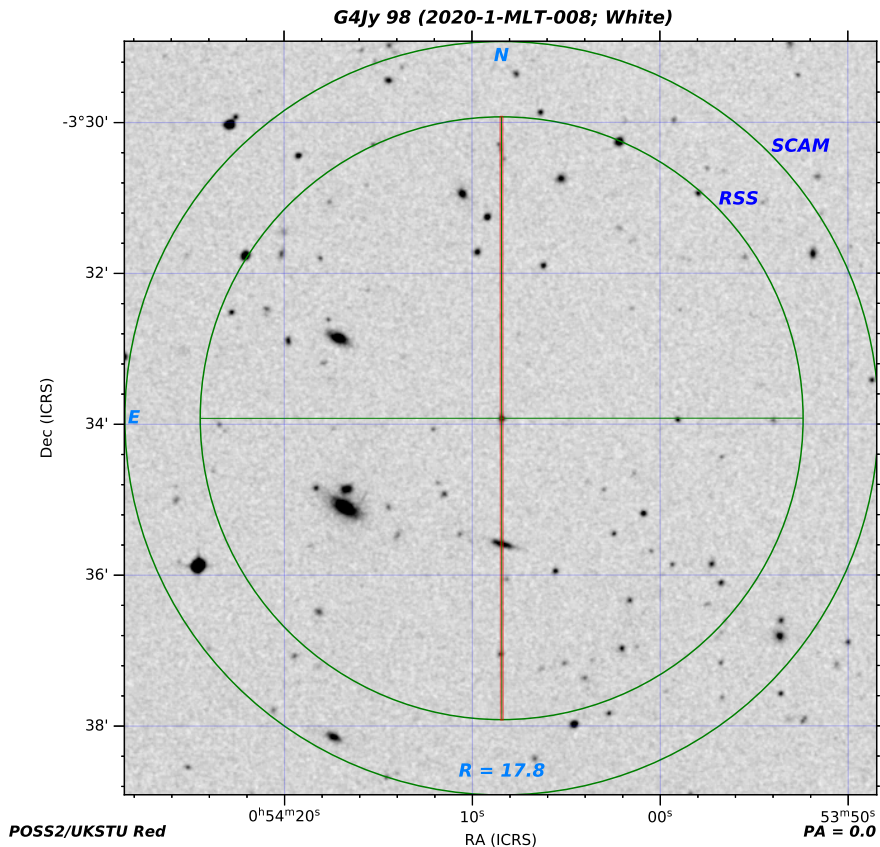


(a) Finder Chart for G4Jy 43

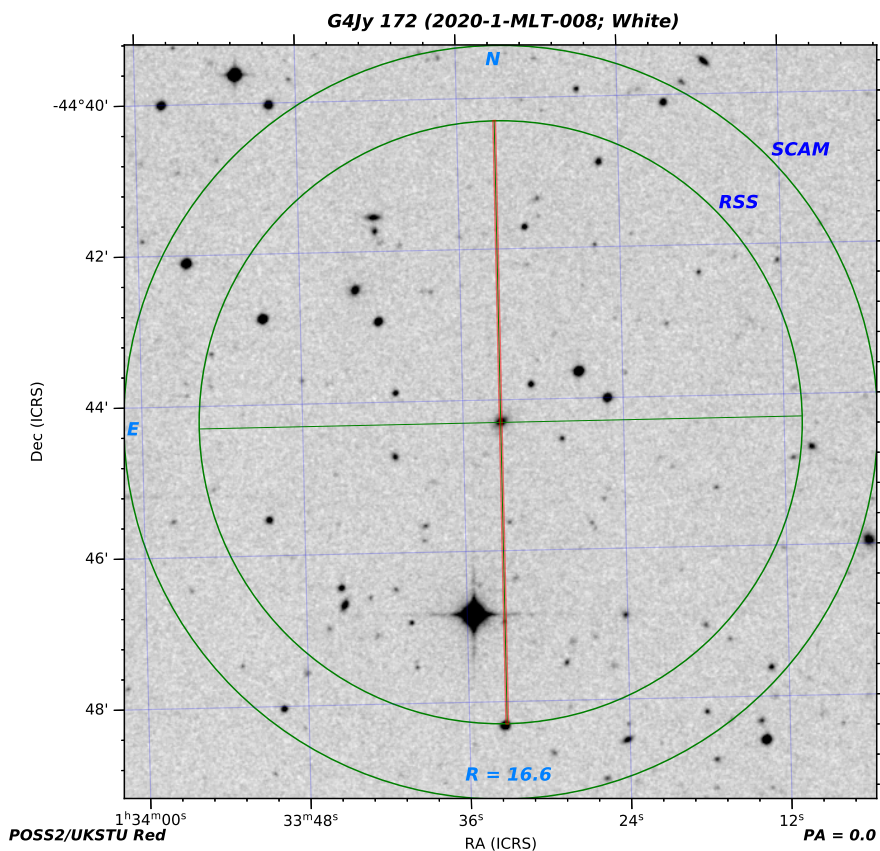


(b) Finder Chart for G4Jy 45

Figure 9. SALT Finder Charts, with the target at the centre. A non-zero Position Angle (PA) for the slit indicates that an alignment object was used.

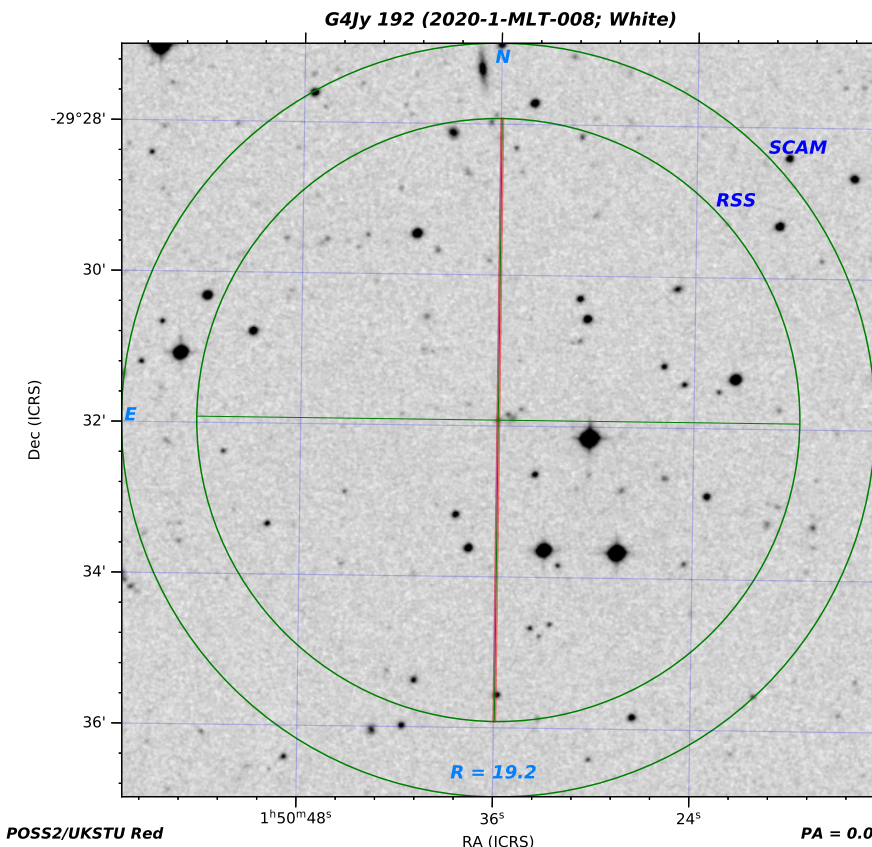


(a) Finder Chart for G4Jy 98

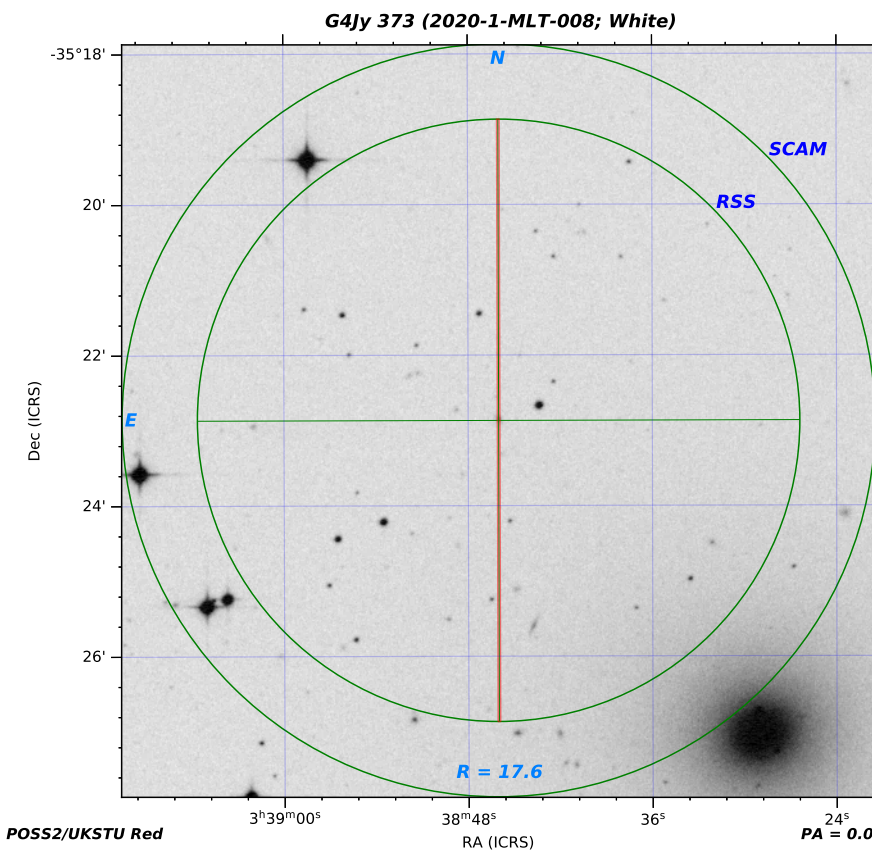


(b) Finder Chart for G4Jy 172

Figure 9. *Continued* – SALT Finder Charts, with the target at the centre.

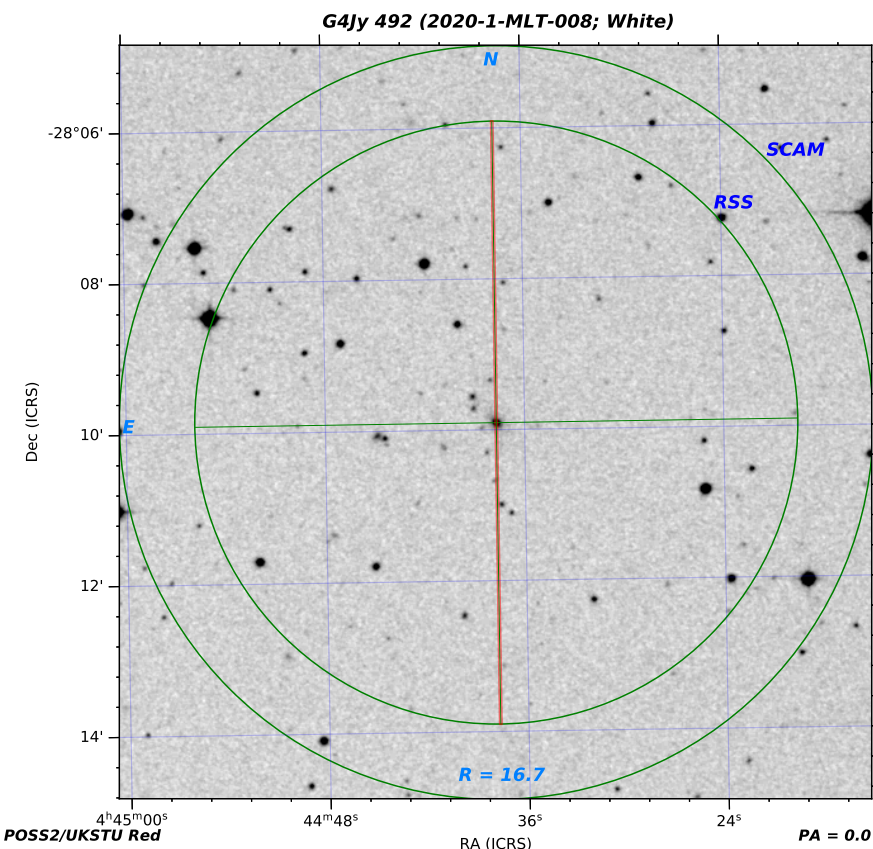


(a) Finder Chart for G4Jy 192

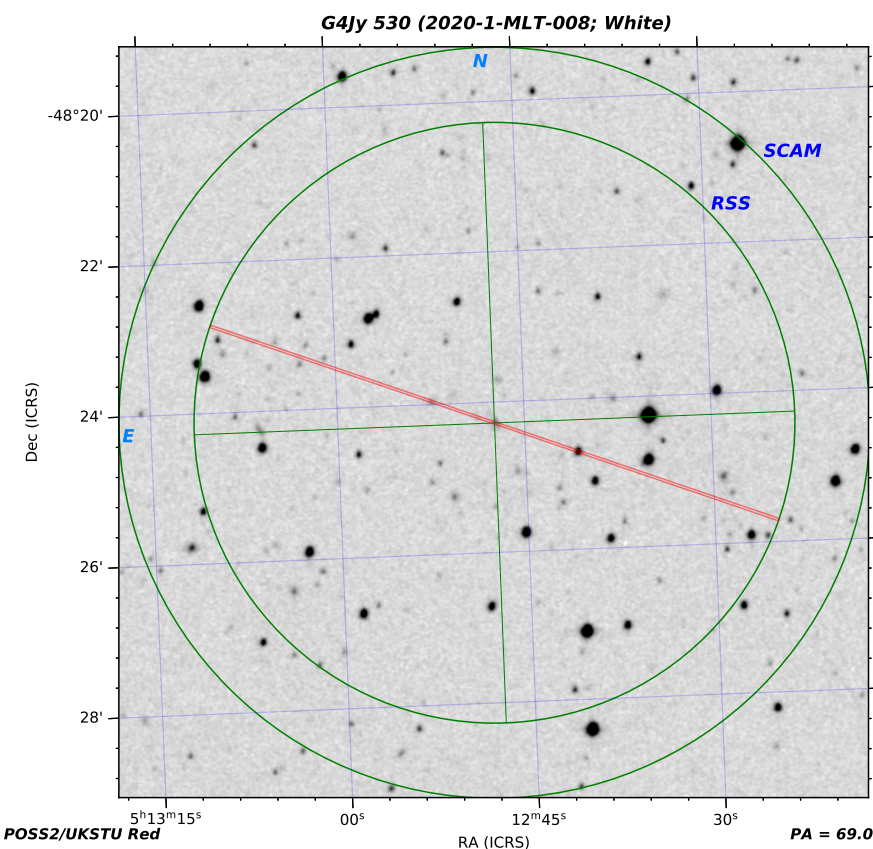


(b) Finder Chart for G4Jy 373

Figure 9. Continued – SALT Finder Charts, with the target at the centre.

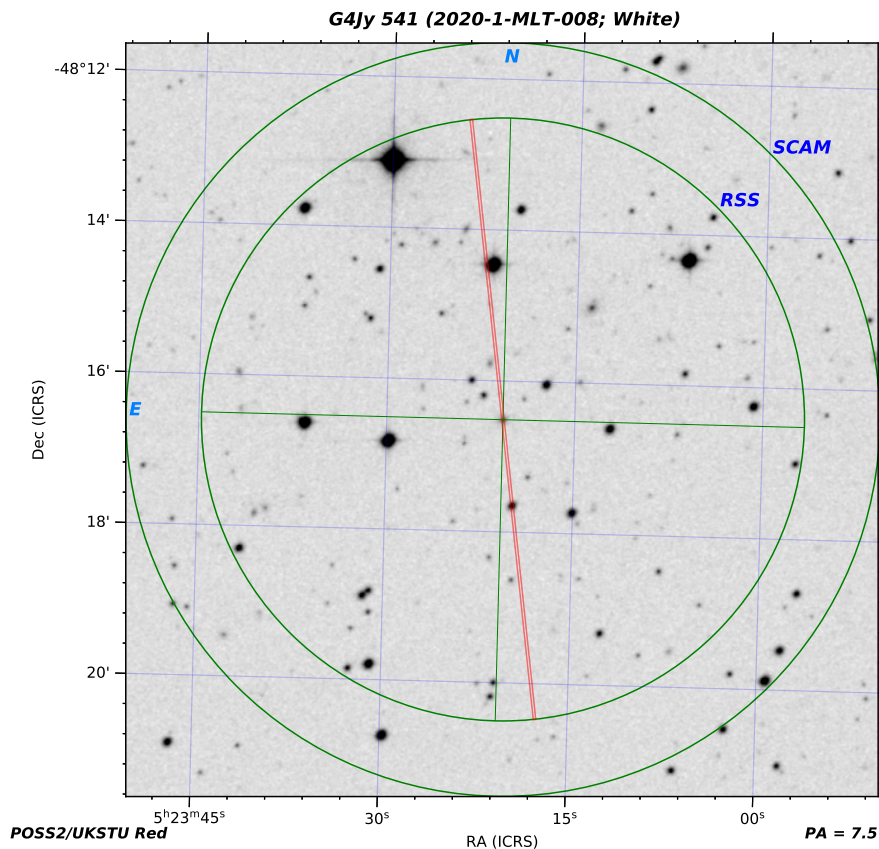


(a) Finder Chart for G4Jy 492

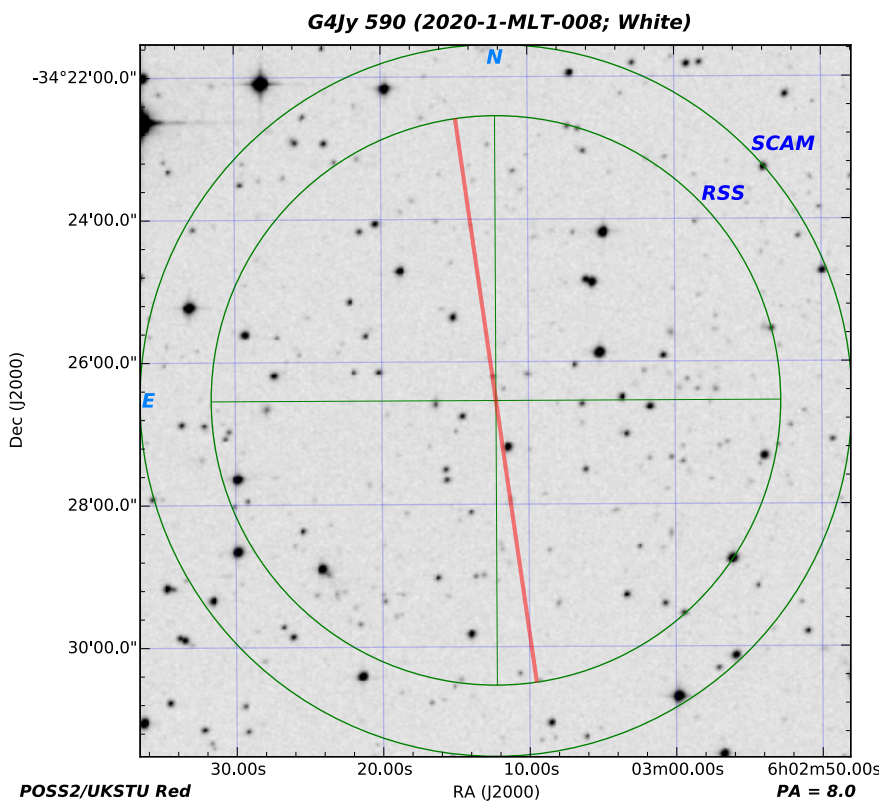


(b) Finder Chart for G4Jy 530

Figure 9. *Continued* – SALT Finder Charts, with the target at the centre.

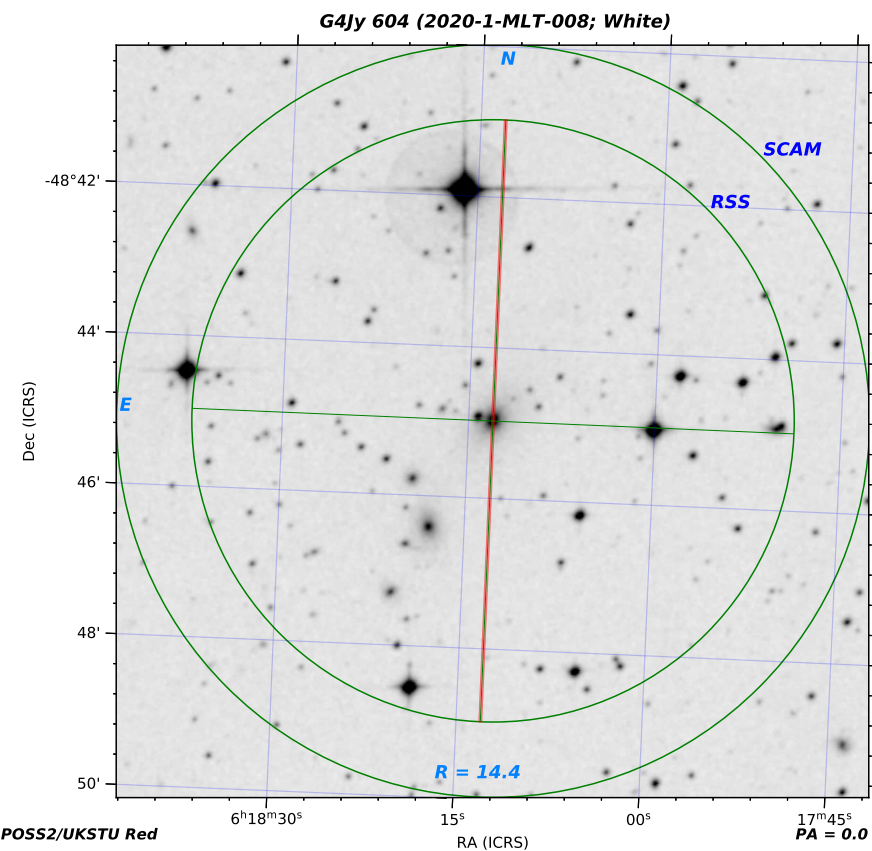


(a) Finder Chart for G4Jy 541

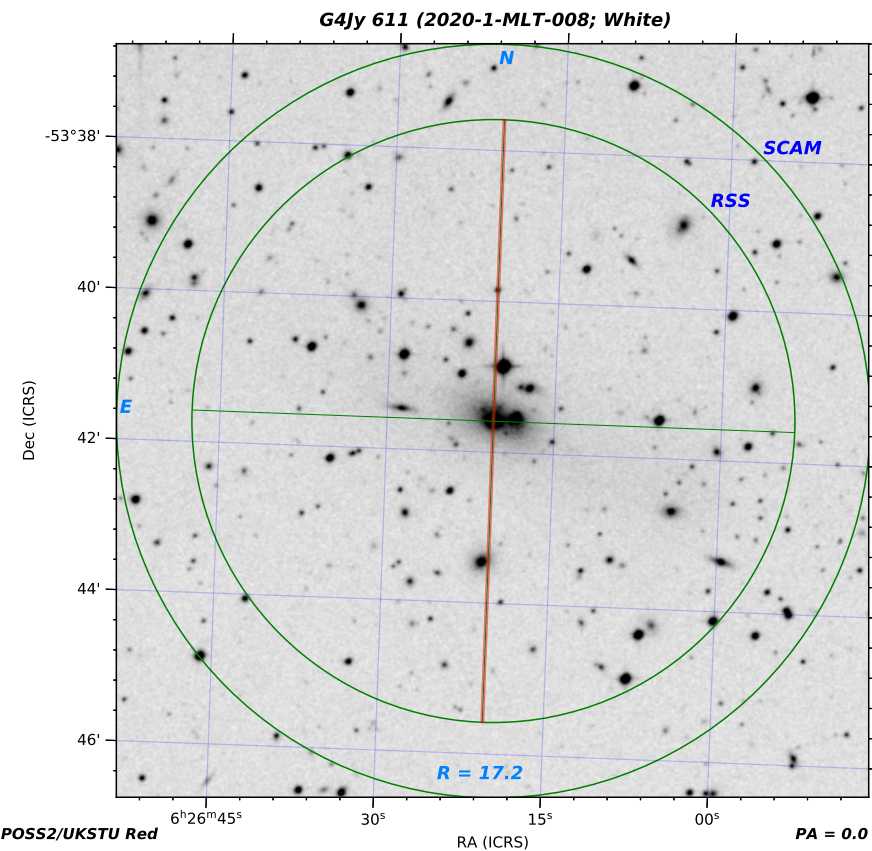


(b) Finder Chart for G4Jy 590

Figure 9. Continued – SALT Finder Charts, with the target at the centre.

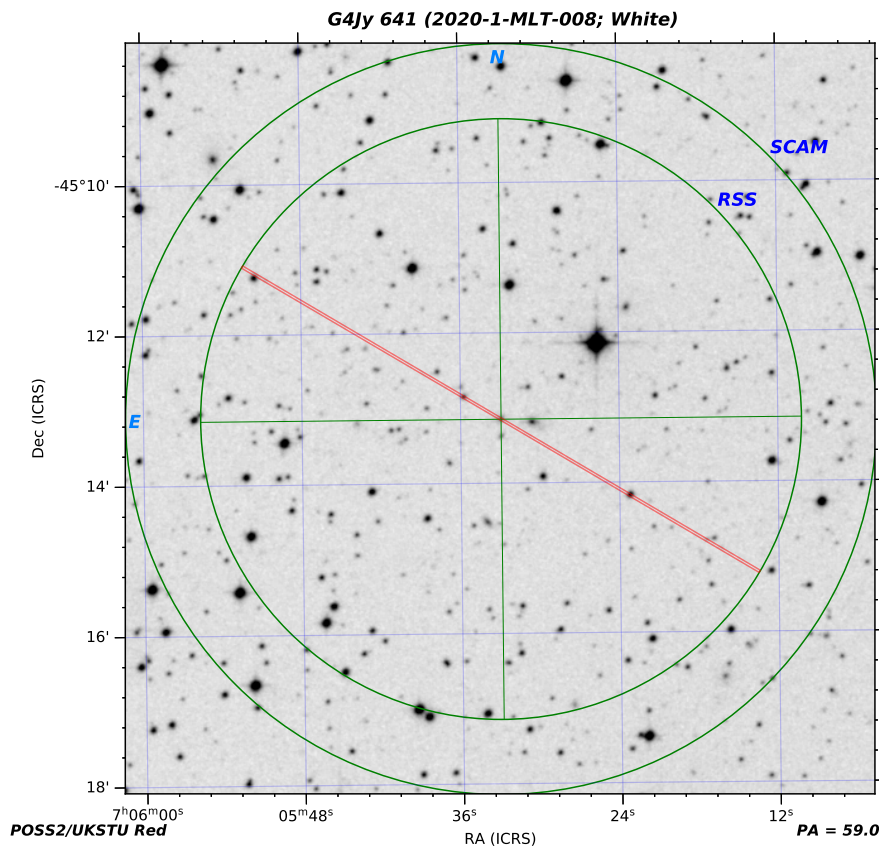


(a) Finder Chart for G4Jy 604

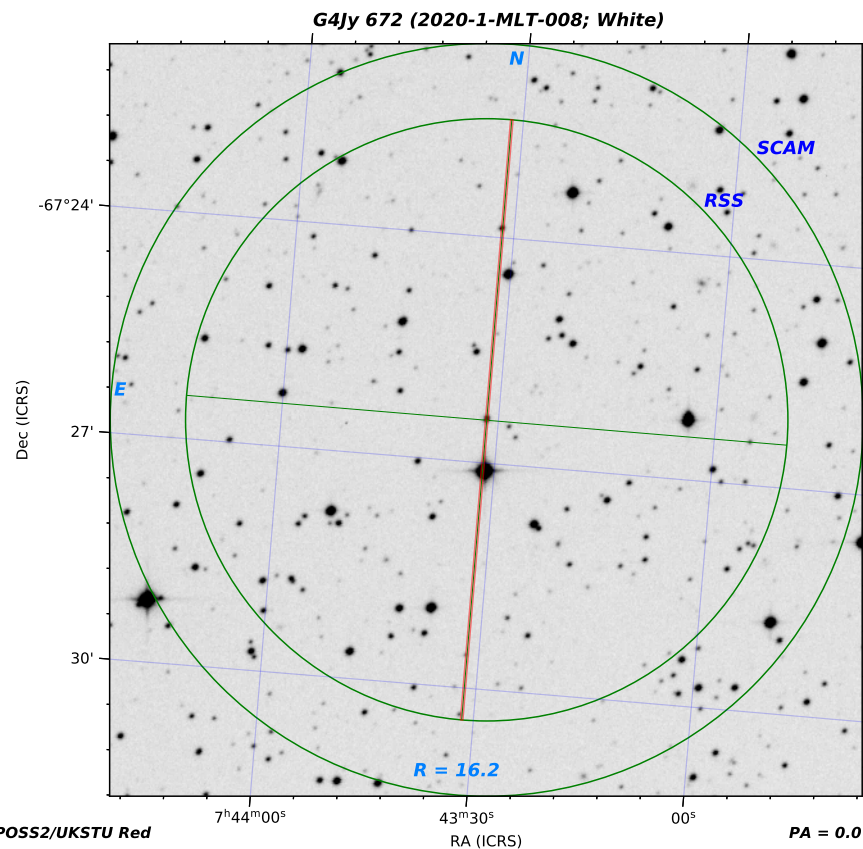


(b) Finder Chart for G4Jy 611

Figure 9. *Continued* – SALT Finder Charts, with the target at the centre.

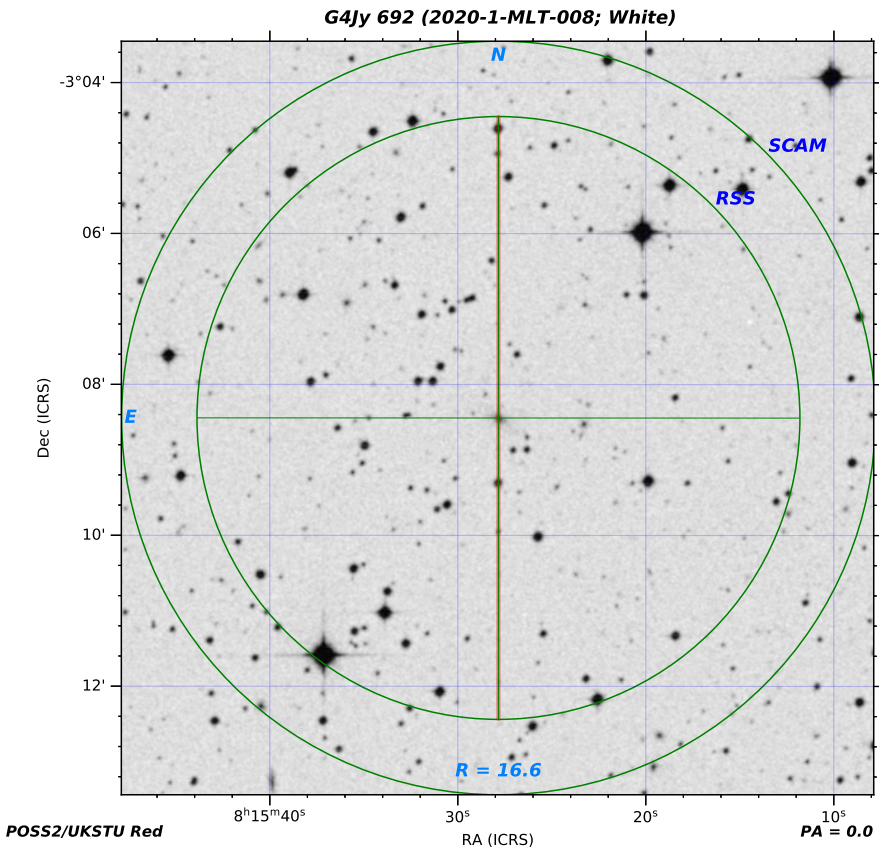


(a) Finder Chart for G4Jy 641

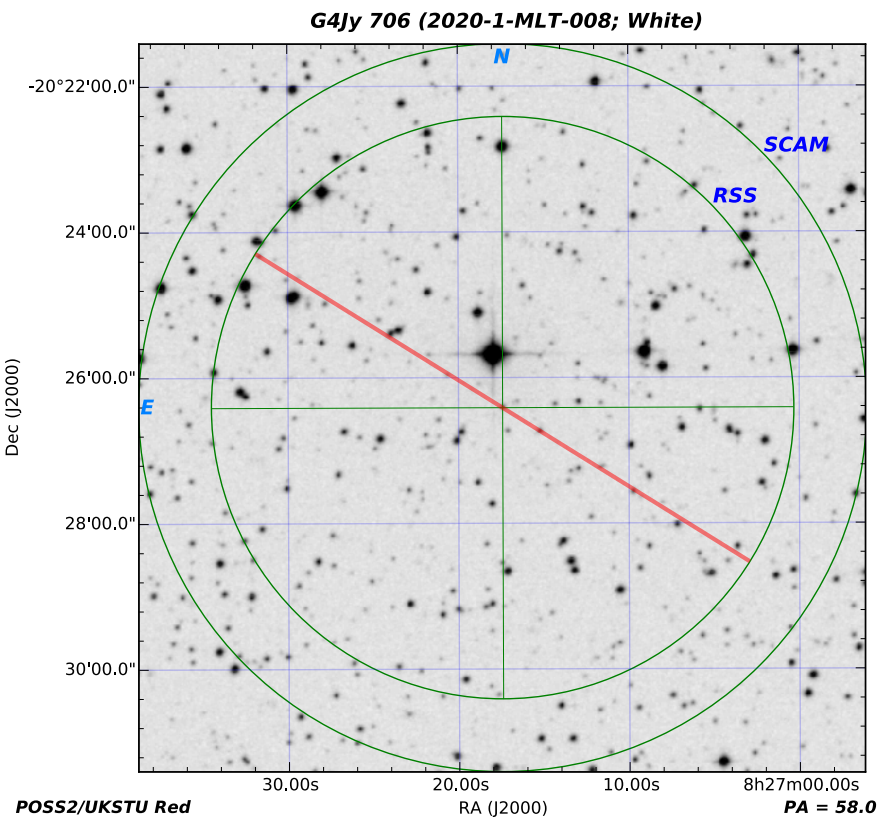


(b) Finder Chart for G4Jy 672

Figure 9. *Continued – SALT Finder Charts, with the target at the centre.*

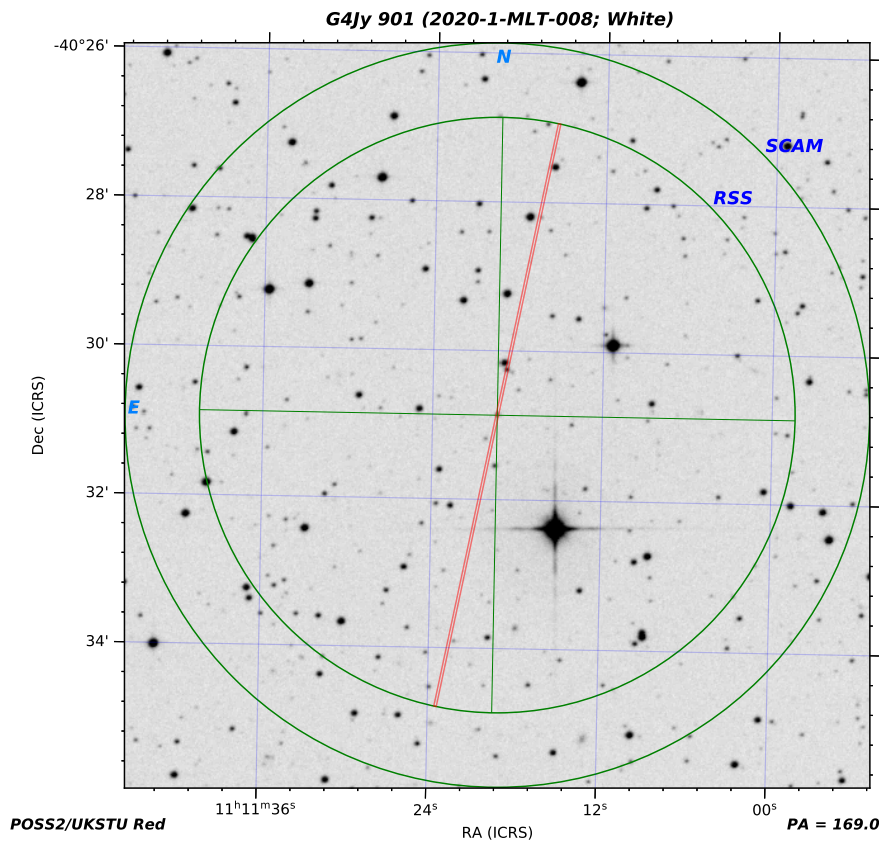


(a) Finder Chart for G4Jy 692

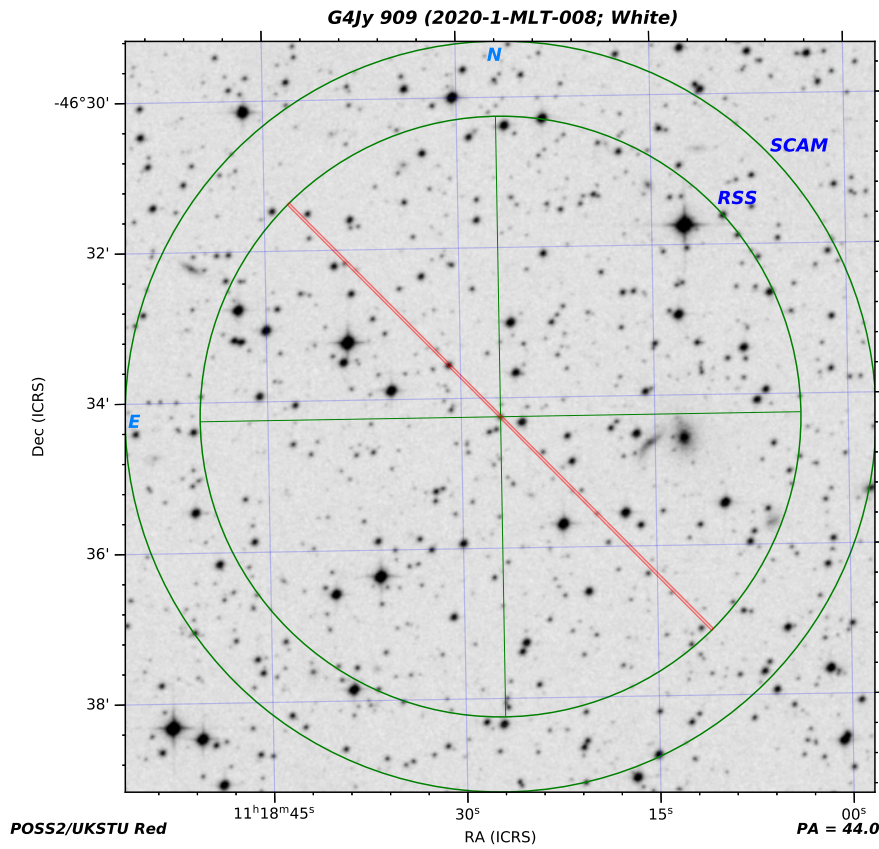


(b) Finder Chart for G4Jy 706

Figure 9. Continued – SALT Finder Charts, with the target at the centre.

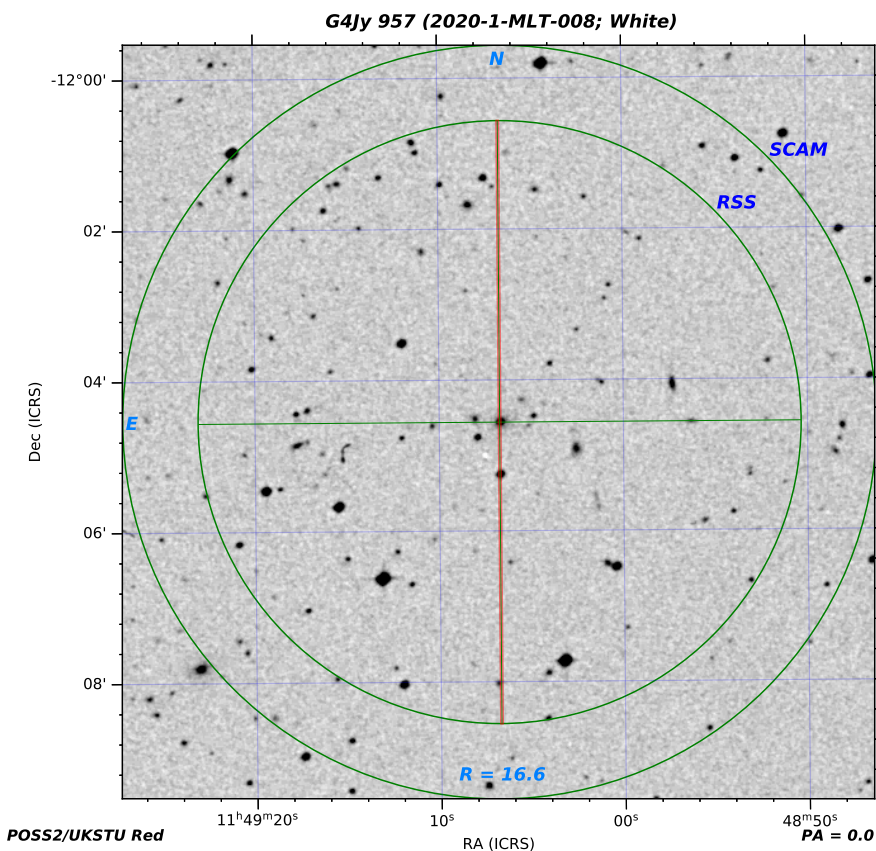


(a) Finder Chart for G4Jy 901

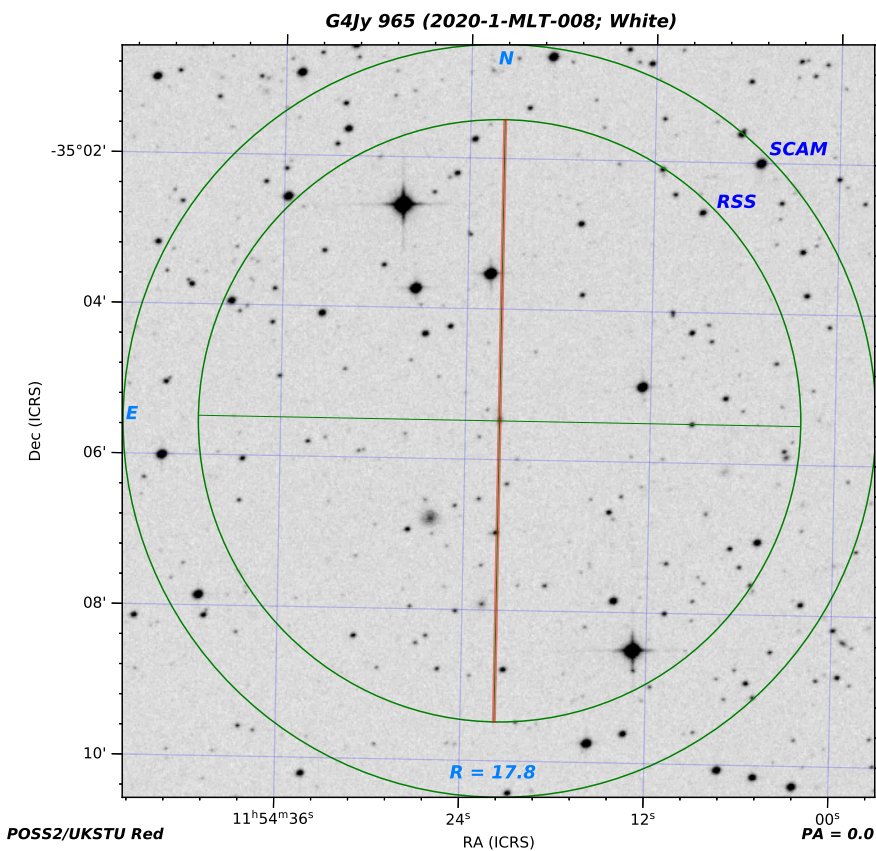


(b) Finder Chart for G4Jy 909

Figure 9. *Continued – SALT Finder Charts, with the target at the centre.*

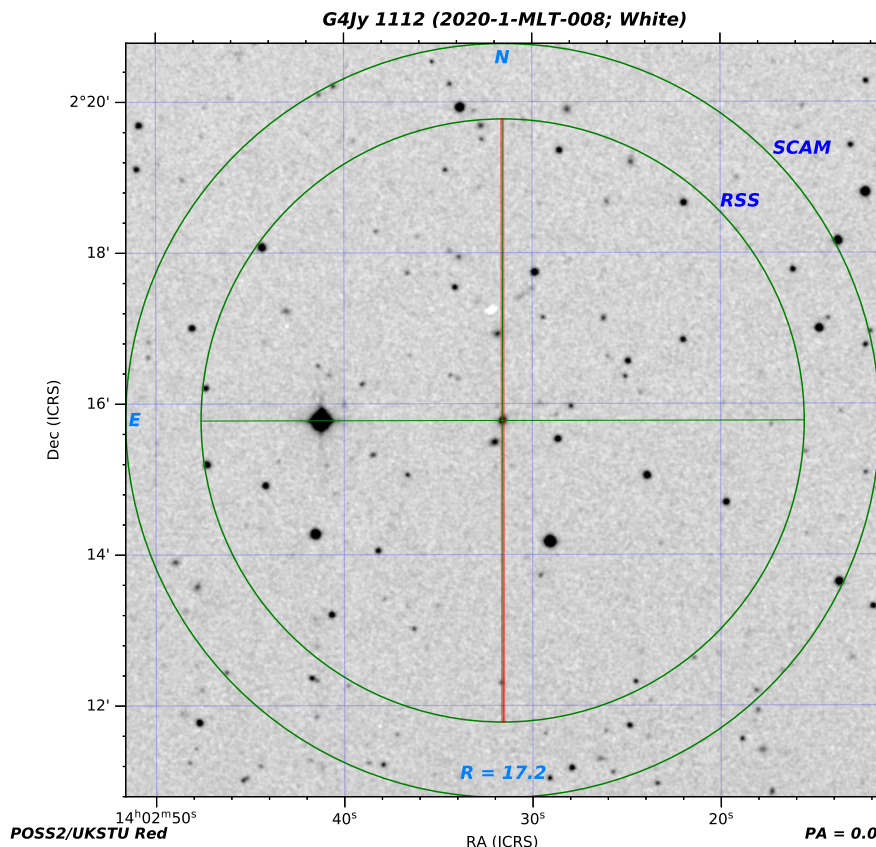


(a) Finder Chart for G4Jy 957

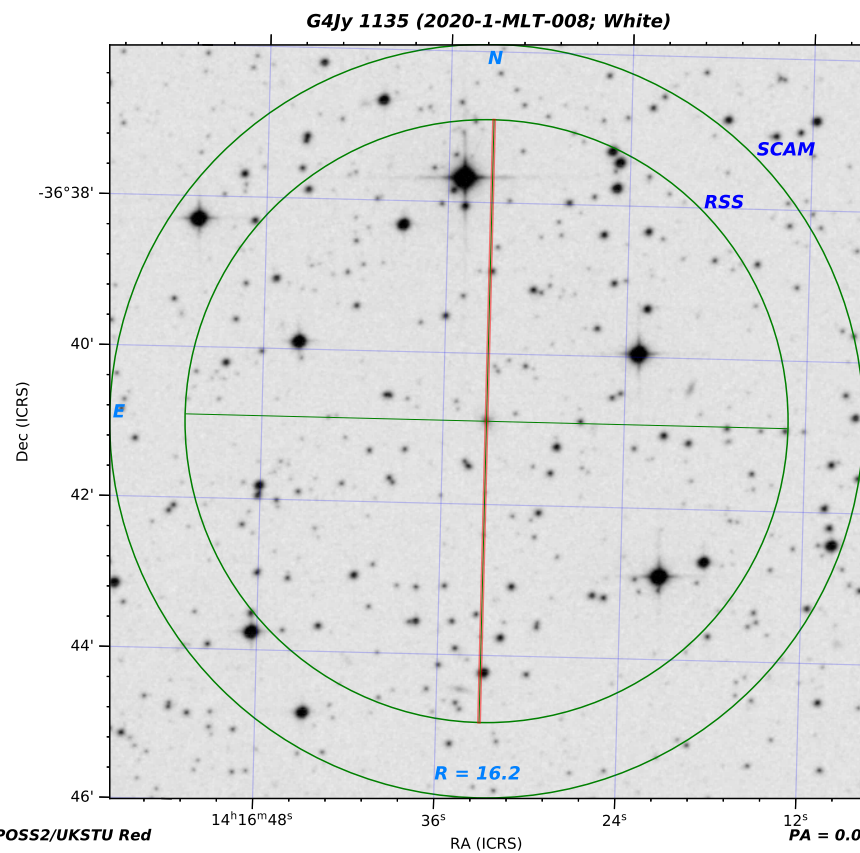


(b) Finder Chart for G4Jy 965

Figure 9. *Continued* – SALT Finder Charts, with the target at the centre.



(a) Finder Chart for G4Jy 1112



(b) Finder Chart for G4Jy 1135

Figure 9. *Continued – SALT Finder Charts, with the target at the centre.*

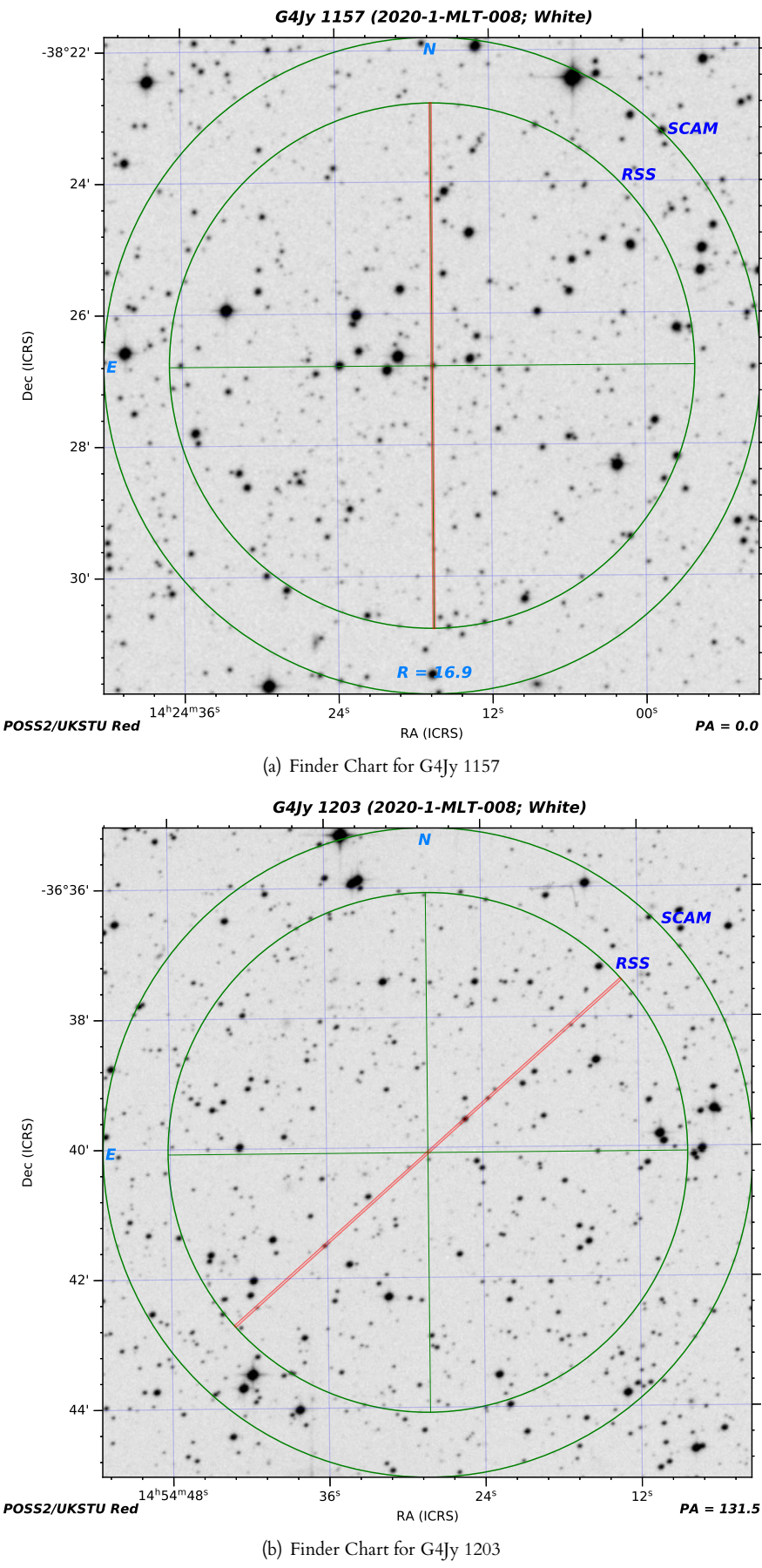


Figure 9. Continued – SALT Finder Charts, with the target at the centre.

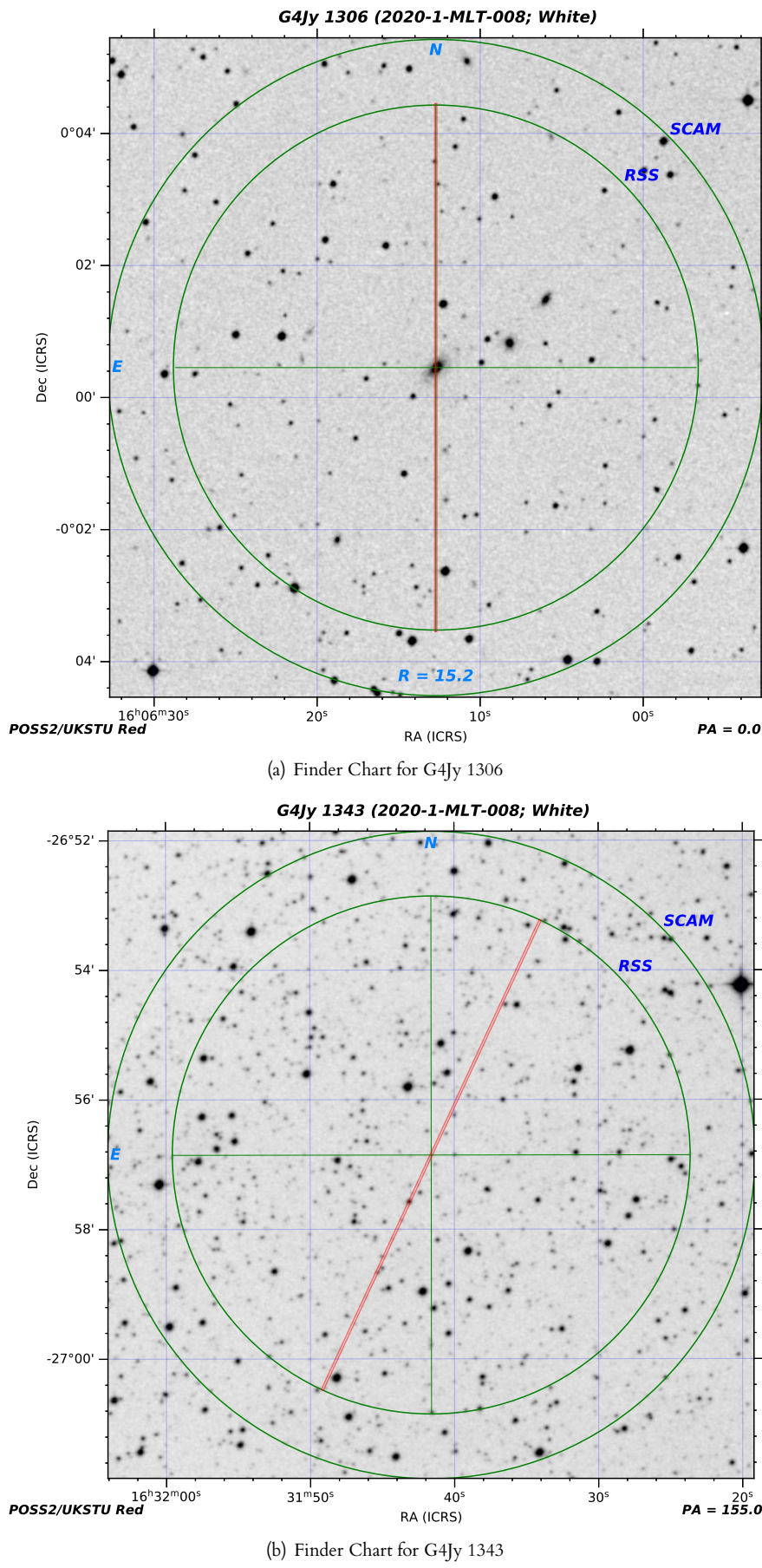
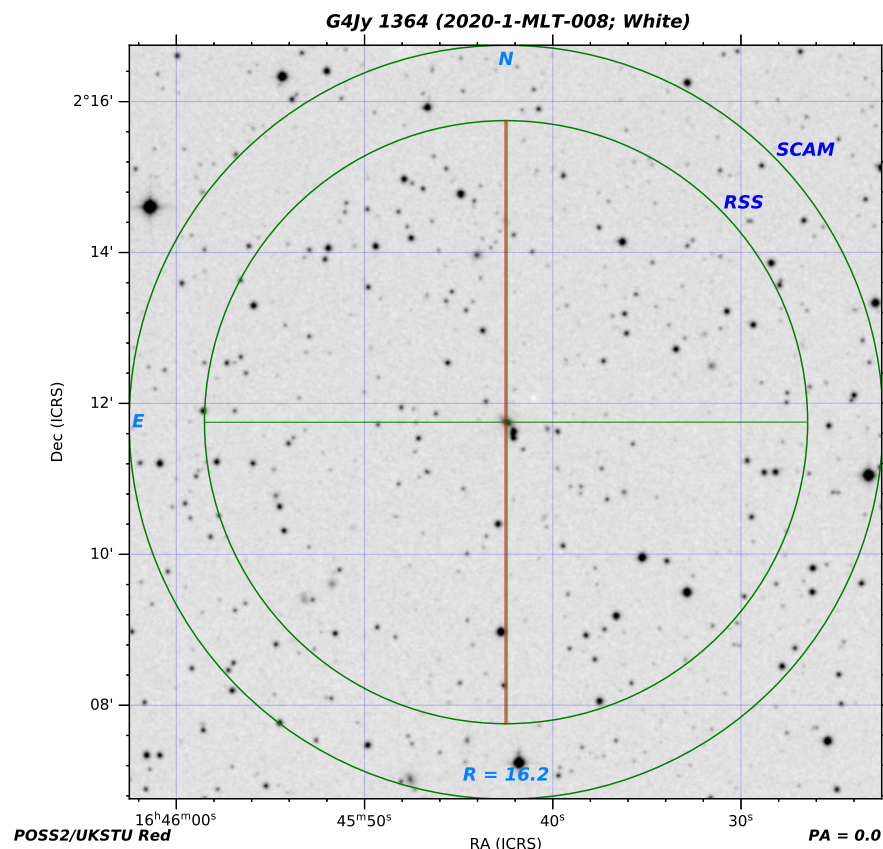
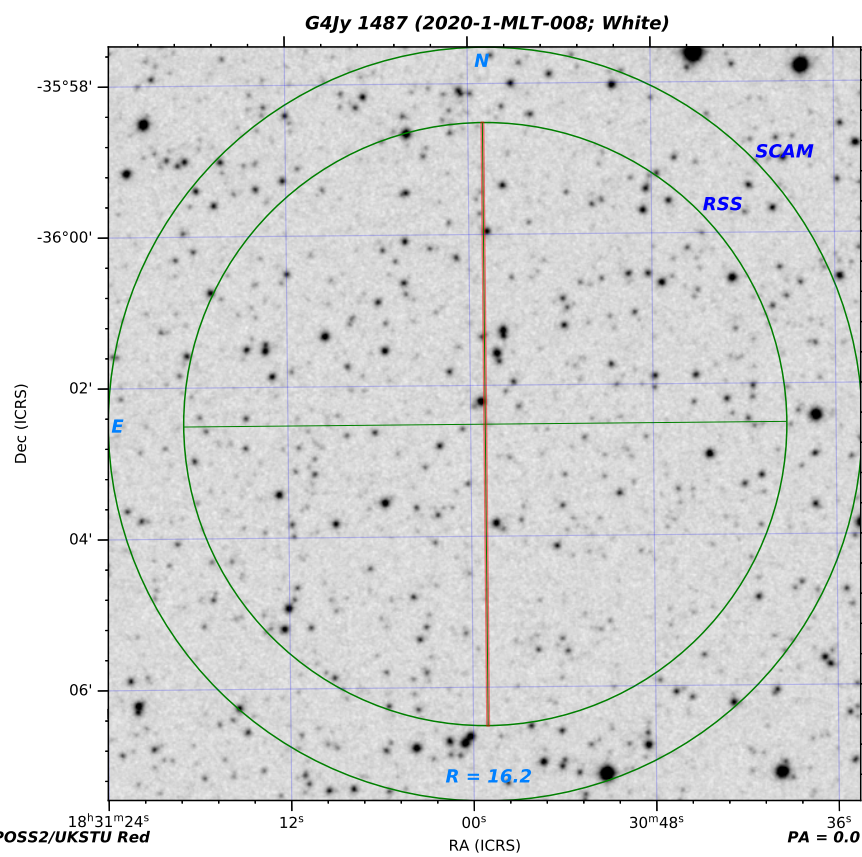


Figure 9. *Continued* – SALT Finder Charts, with the target at the centre.

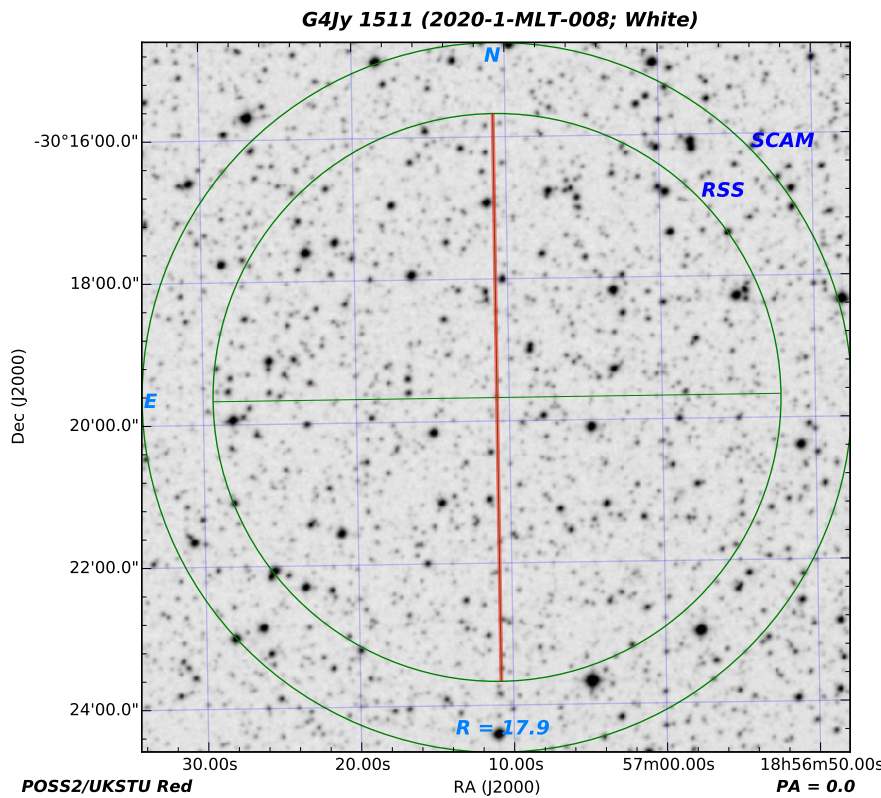


(a) Finder Chart for G4Jy 1364

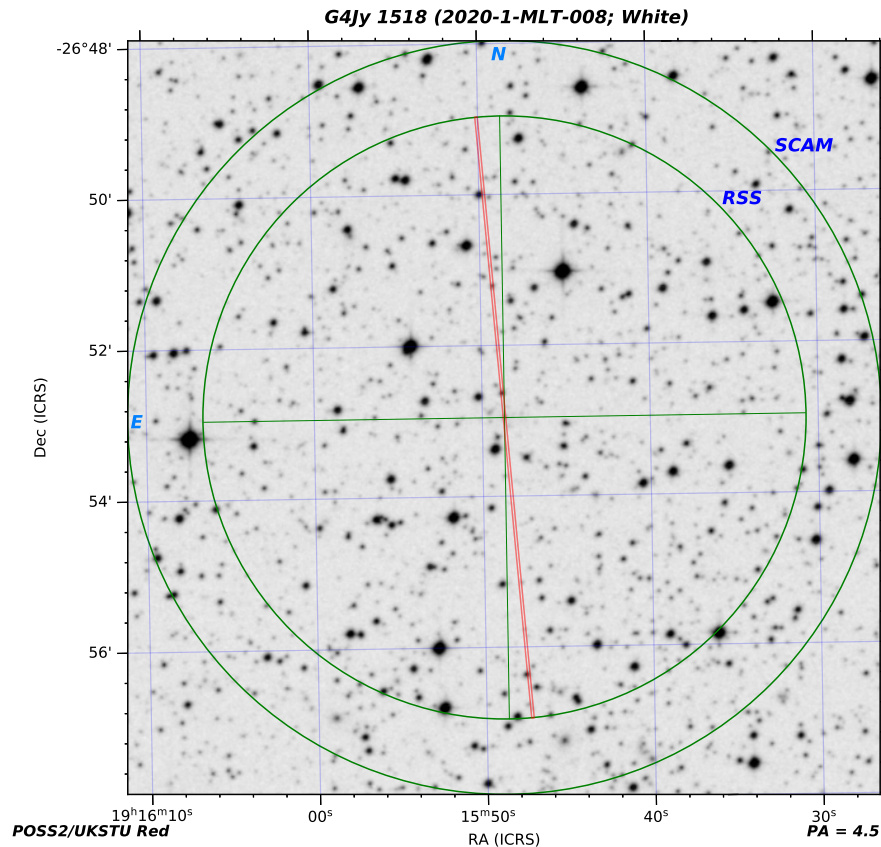


(b) Finder Chart for G4Jy 1487

Figure 9. *Continued* – SALT Finder Charts, with the target at the centre.

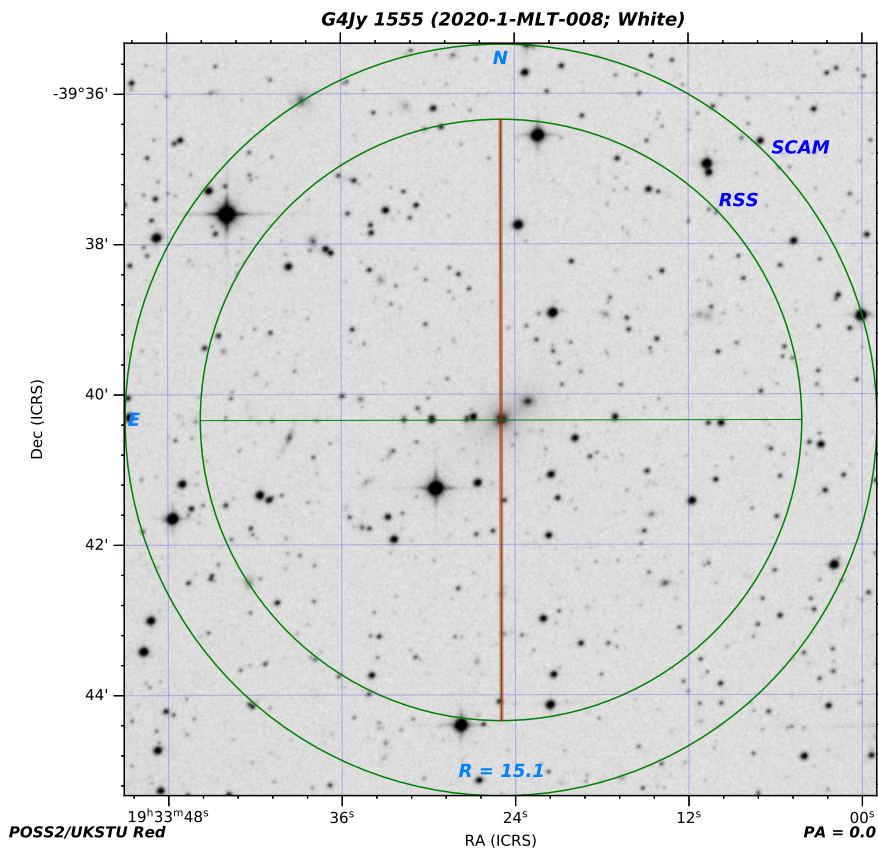


(a) Finder Chart for G4Jy 1511

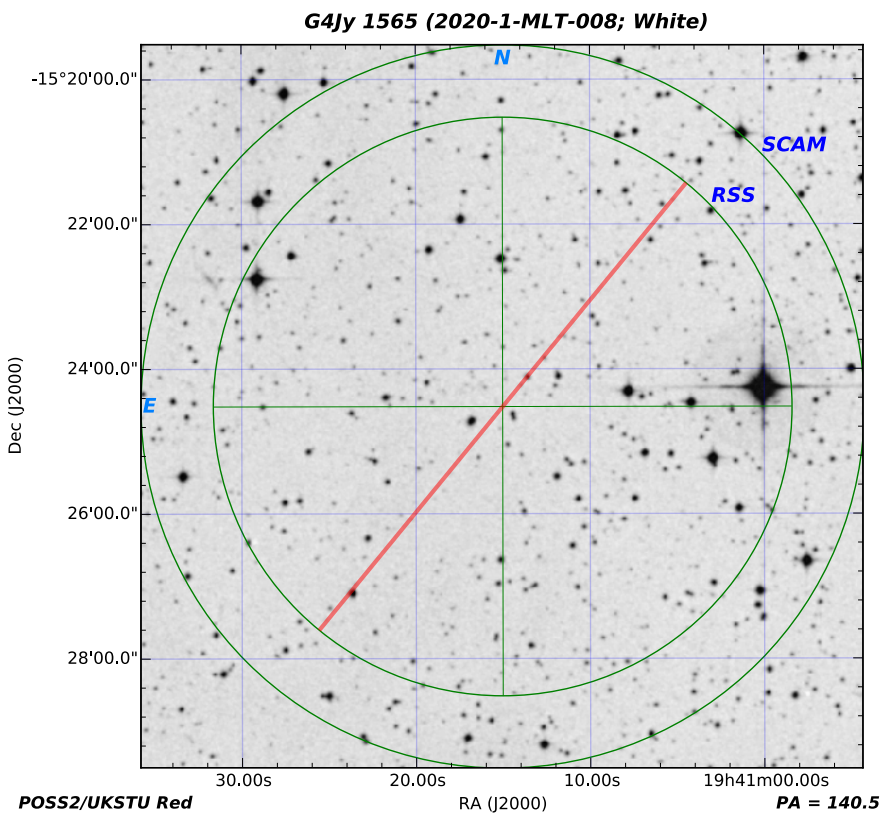


(b) Finder Chart for G4Jy 1518

Figure 9. Continued – SALT Finder Charts, with the target at the centre.

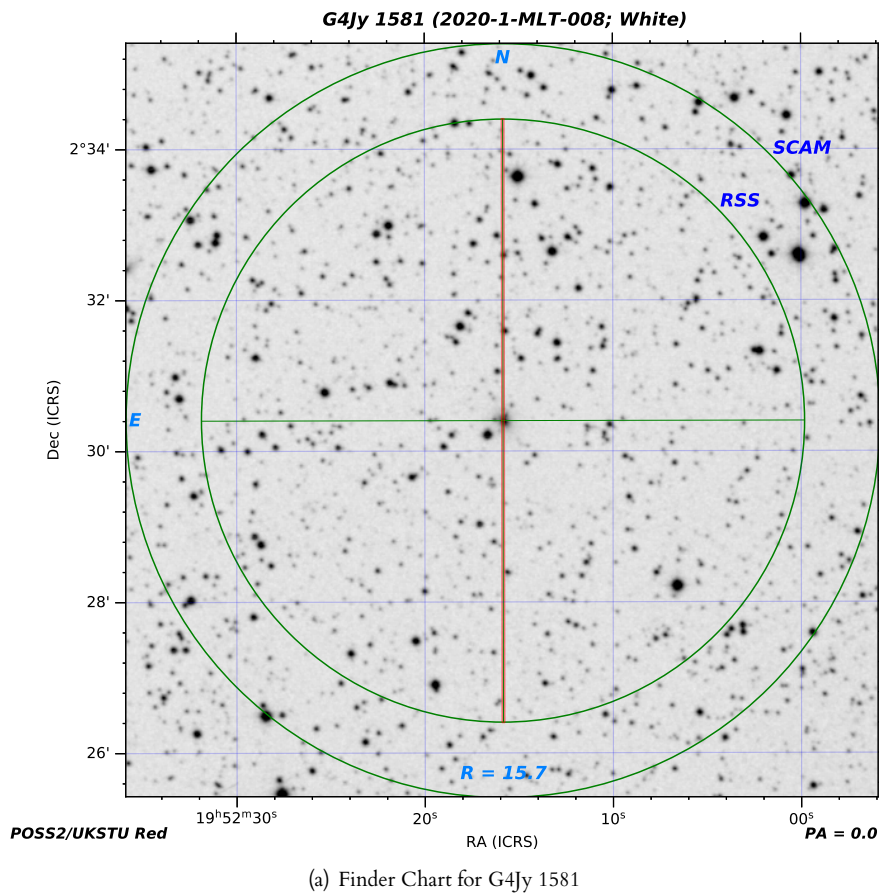


(a) Finder Chart for G4Jy 1555

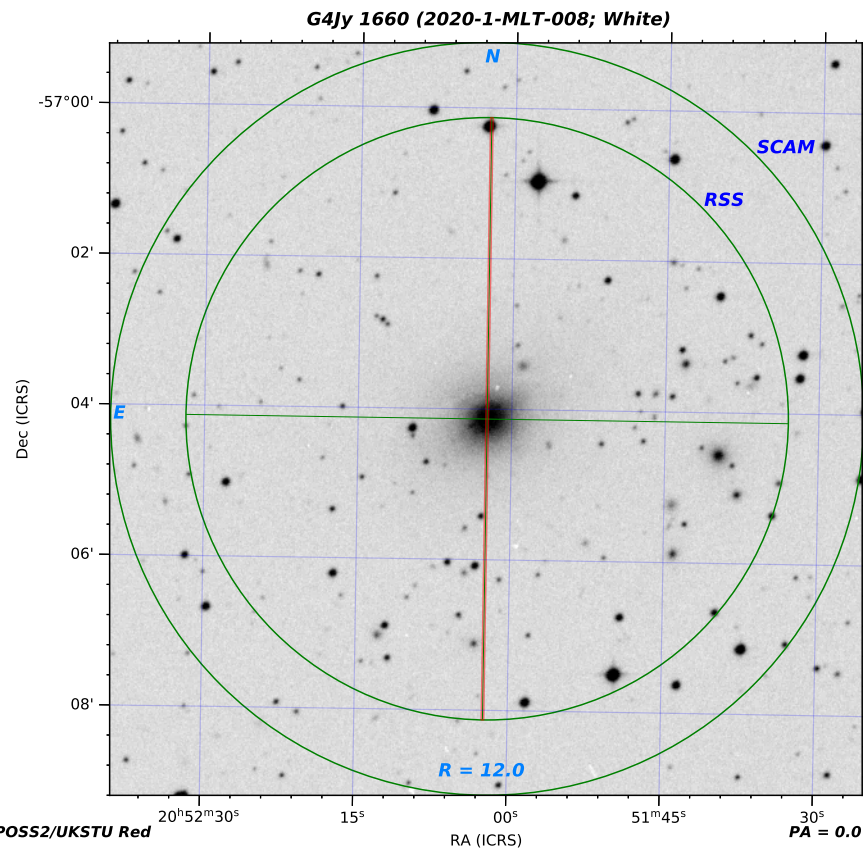


(b) Finder Chart for G4Jy 1565

Figure 9. Continued – SALT Finder Charts, with the target at the centre.

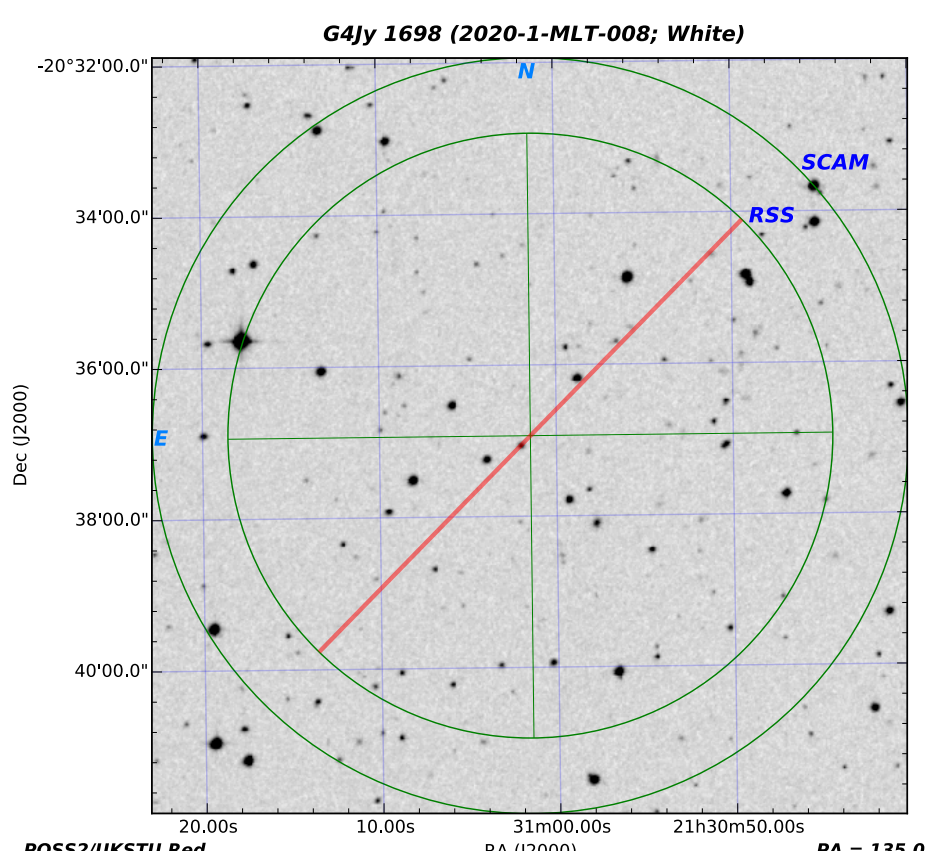
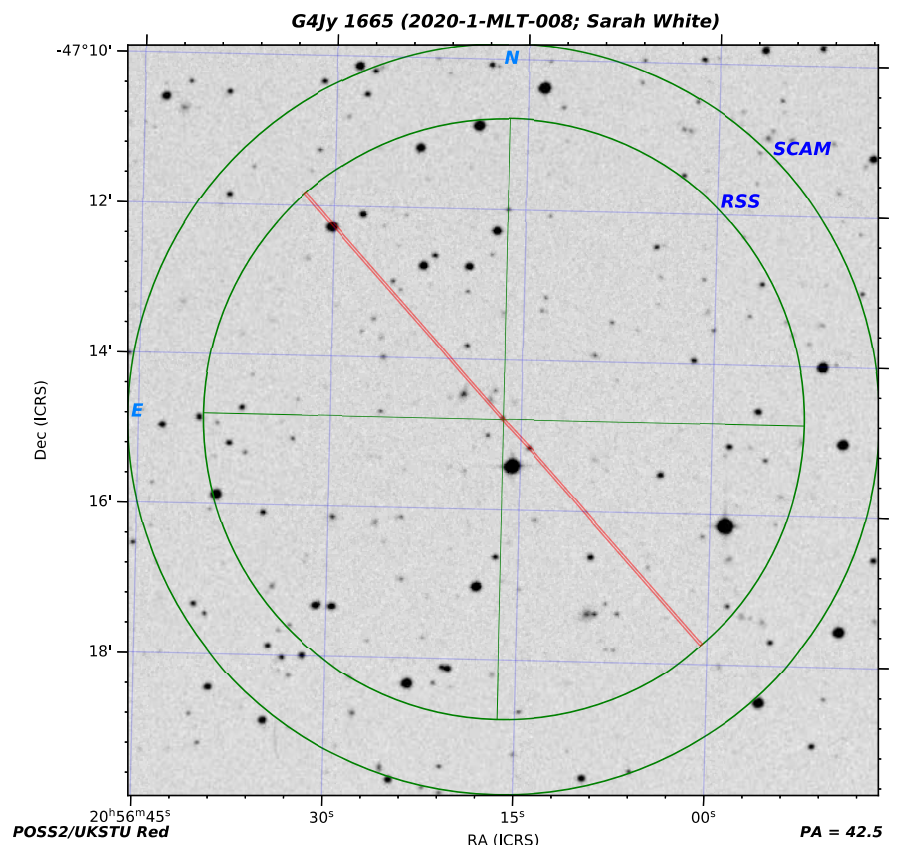


(a) Finder Chart for G4Jy 1581



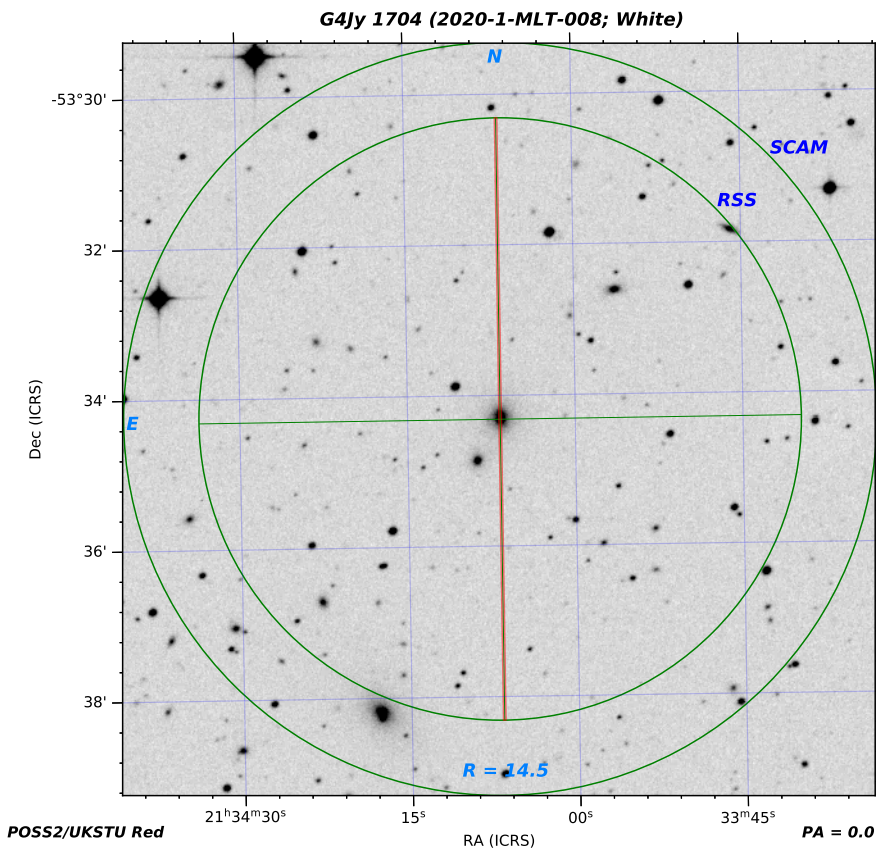
(b) Finder Chart for G4Jy 1660

Figure 9. *Continued* – SALT Finder Charts, with the target at the centre.

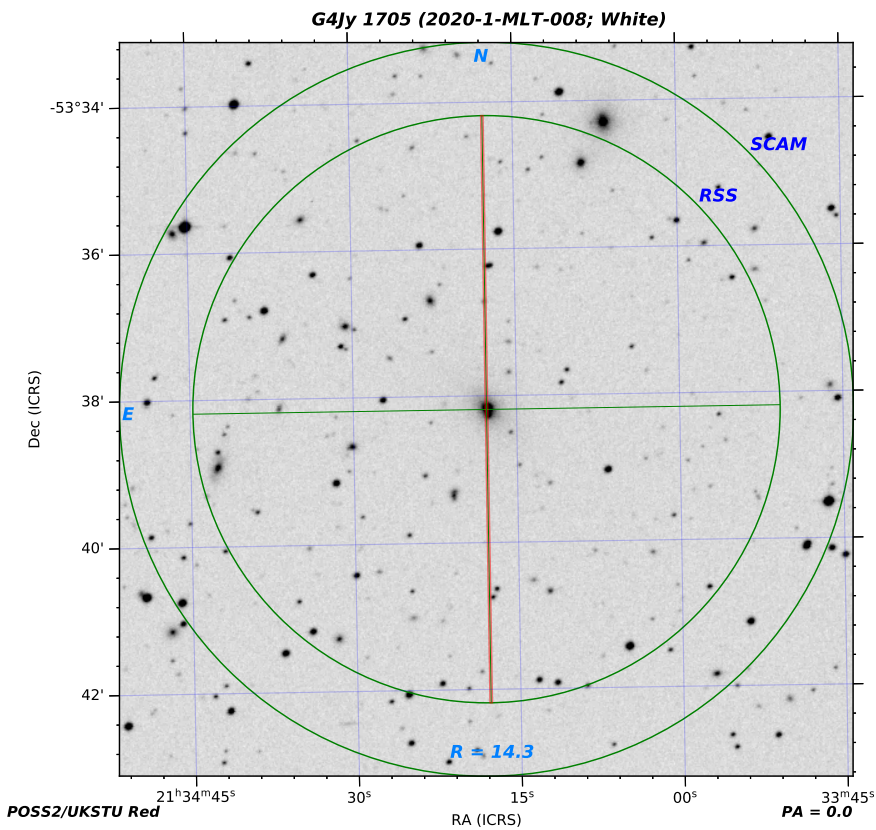


(b) Finder Chart for G4Jy 1698

Figure 9. *Continued* – SALT Finder Charts, with the target at the centre.

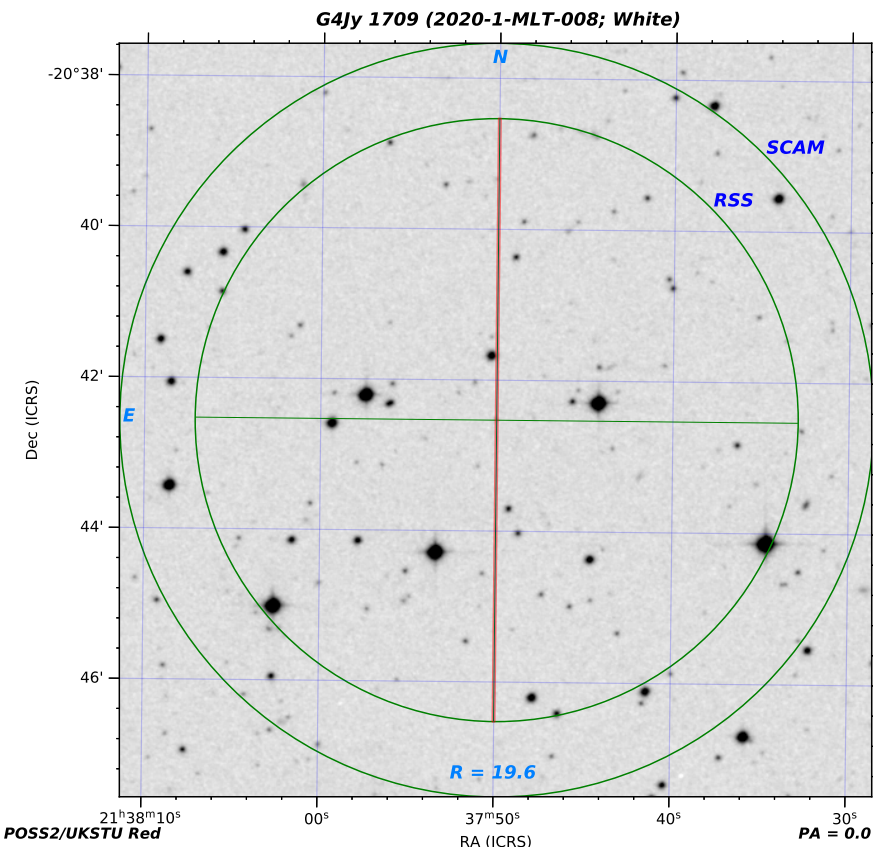


(a) Finder Chart for G4Jy 1704

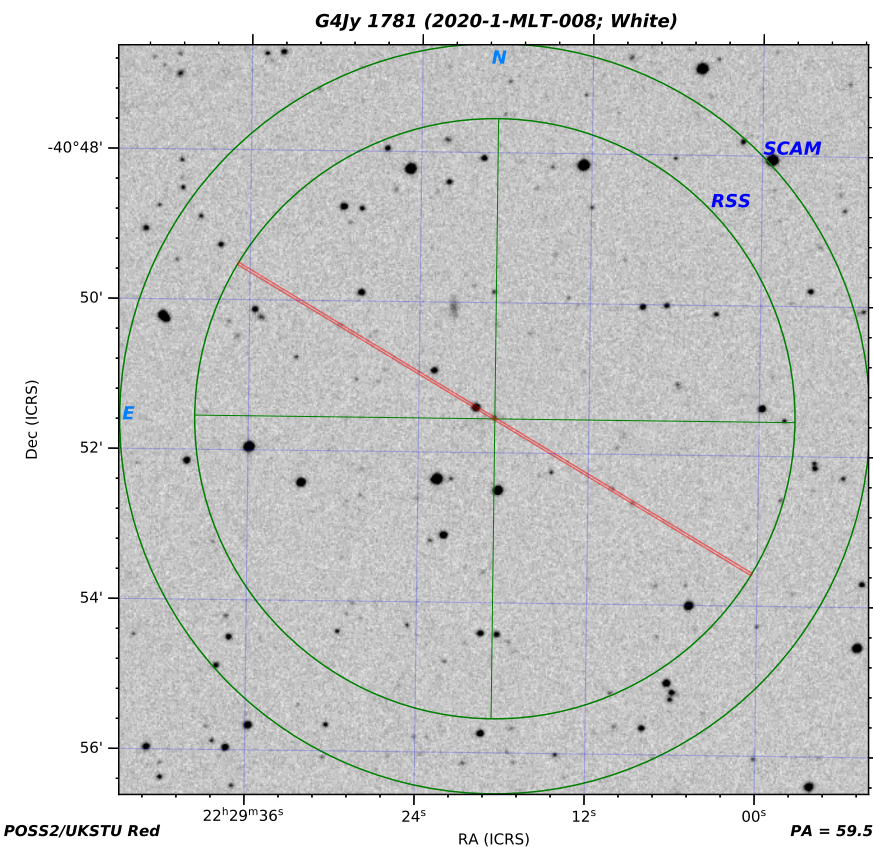


(b) Finder Chart for G4Jy 1705

Figure 9. Continued – SALT Finder Charts, with the target at the centre.



(a) Finder Chart for G4Jy 1709



(b) Finder Chart for G4Jy 1781

Figure 9. *Continued* – SALT Finder Charts, with the target at the centre.

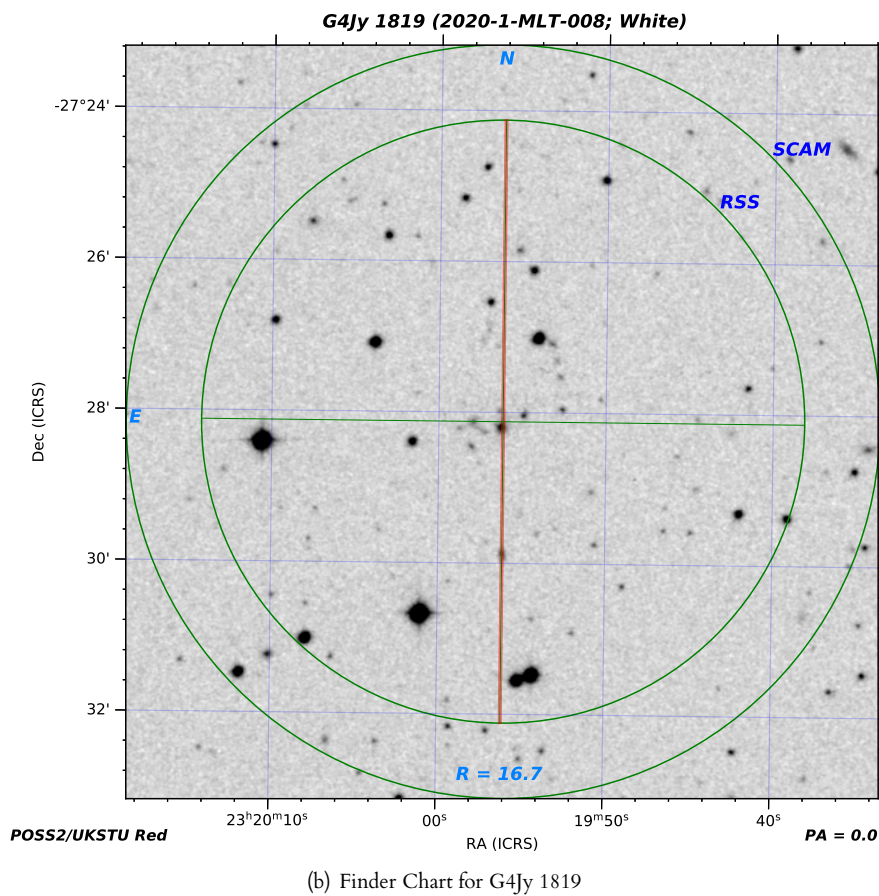
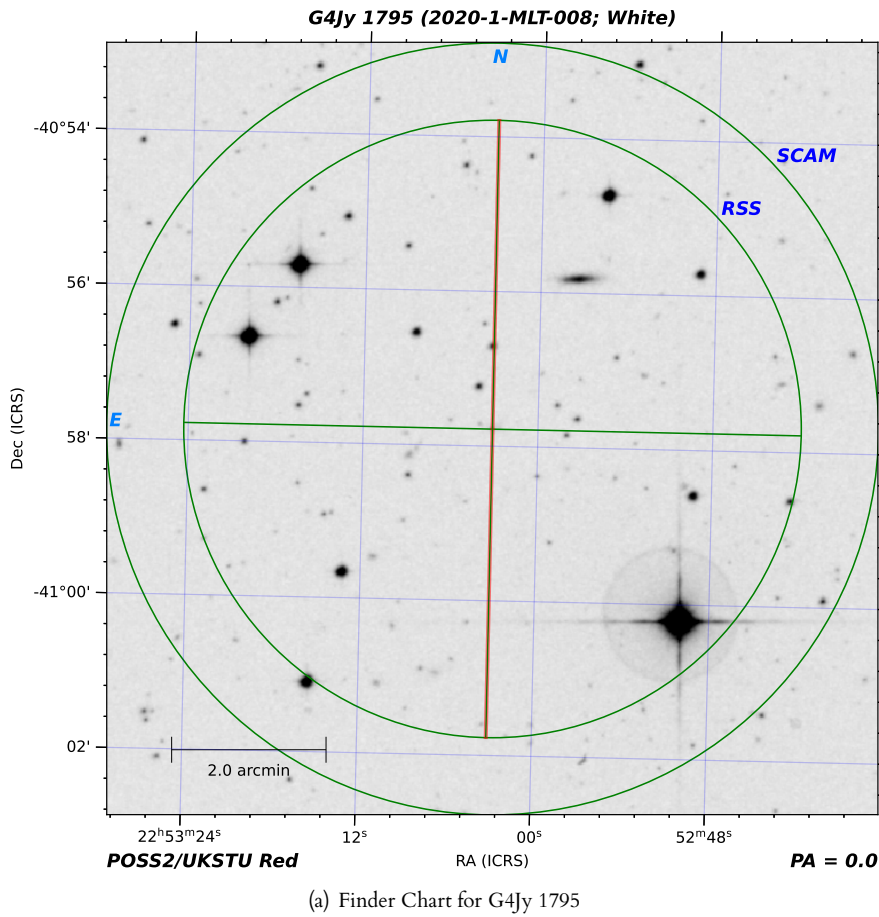


Figure 9. *Continued* – SALT Finder Charts, with the target at the centre.

of $z = 1.965$, and assign an error of 0.005 to accommodate the slight mismatch of the wavelength scaling. For comparison, Osmer et al. (1994) report a redshift of $z = 1.925$, and Yao et al. (2019) provide a redshift of $z = 1.972$. Meanwhile, Steidel & Sargent (1991) measure $z = 1.9417$ from the CIII] line and $z = 1.9635$ from the MgII line.

For G4Jy 176, the emission lines are correctly labelled by the SDSS data-reduction pipeline but the *wavelength* identifications are slightly offset. This is most likely due to resonance leading to “negative emission” that affects the ‘weighting’ of the emission line’s central wavelength^o. Therefore, we re-fit the spectrum with a focus on the (non-resonating) CIII] emission-line, and calculate a spectroscopic redshift of $z = 1.660 \pm 0.005$. Again, the relatively large error is to account for the wavelength scaling being slightly different from that of the redshifted template. Whilst the radio emission of this source is well-documented, we cannot find another spectroscopic redshift in published results.

SDSS provided a redshift of $z = 0.24639 \pm 0.00010$ for G4Jy 679 (3C 190), which is primarily based upon strong [OII] emission being misinterpreted as H α emission. With what we believe to be the correct interpretation, supported by the MgII showing a resonant profile, and multiple emission-line identifications, we find that the spectroscopic redshift is $z = 1.196 \pm 0.001$. This is in good agreement with $z = 1.195649 \pm 0.000368$ from optical spectroscopy (Hewett & Wild, 2010), and with $z = 1.1944 \pm 0.0012$ through H i absorption (Grasha et al., 2019).

Like G4Jy 148, G4Jy 845 (3C 243) has its CIV emission mislabelled as Lyman- α , and the prominent emission of CIII] and MgII going unidentified. Our re-fitting of the spectrum leads to a redshift ($z = 1.706 \pm 0.001$) that is again in close agreement with that provided by Hewett & Wild (2010, $z = 1.70756 \pm 0.00049$).

Finally, G4Jy 1240 (3C 316) had originally been identified as the highest-redshift source in the G4Jy Sample, at $z \sim 5.5$ (!). However, inspection of the SDSS spectrum showed that the [OIII] line at rest-frame $\lambda = 5007 \text{ \AA}$ had been misidentified as a Lyman- α line. Re-fitting the quasar spectrum gives a redshift of $z = 0.581 \pm 0.001$, which is in close agreement with previous spectroscopic redshifts available via prior work ($z = 0.5795$; Gendre & Wall, 2008; Smith et al., 2010). Indeed, via the SALT helpdesk (with thanks to Joel Brownstein) it was found that, although the lowest- χ^2 fit in SDSS’s automated pipeline (Bolton et al., 2012) had $z = 5.49964$, the third next-best fit has $z = 0.580673$. (For interest, we add lower-ranked SDSS redshifts to Table 4.)

^o<https://skyserver.sdss.org/dr16/en/get/SpecById.ashx?id=8654825137051553792>

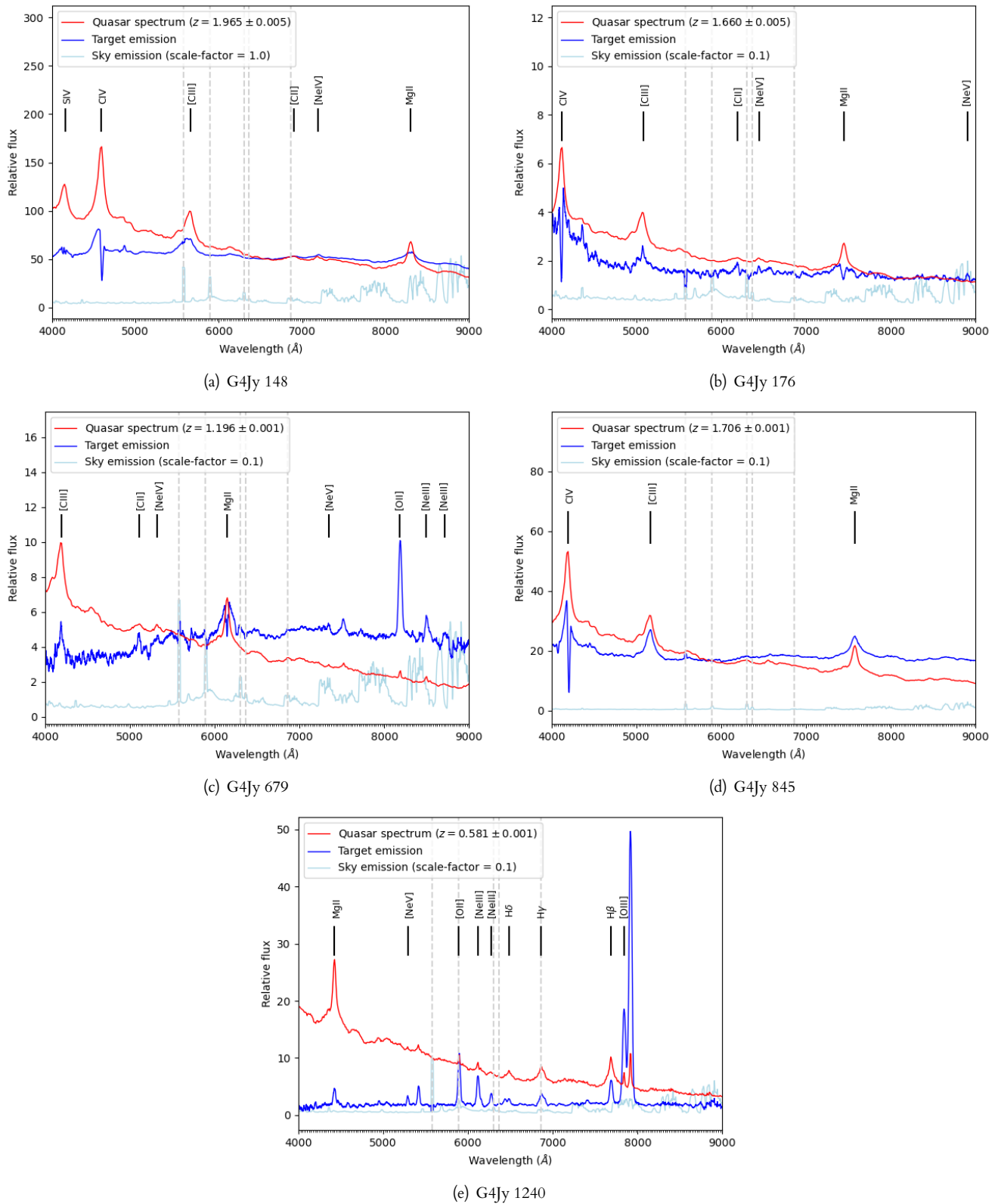


Figure 10. SDSS spectra (blue lines) of G4Jy sources (Section 3 and Appendix 3), with sky-emission spectra represented by lighter-blue lines. (The latter is scaled to aid comparison with the target emission, and the scale factor that has been applied is noted in each legend.) The dashed, grey, vertical lines indicate prominent sky-emission, and the target spectrum is re-fitted with the appropriate template spectrum (red lines).

Table 3. Angular sizes, spectral indices, and 151-MHz flux-densities for 299 G4Jy sources, provided in the G4Jy catalogue (White et al., 2020b,a). These G4Jy spectral indices ('G4Jy_alpha') are measured across 20 flux-densities, from 72 MHz to 231 MHz. By combining these data with redshift information from SALT (this work), 6dFGS (Jones et al., 2009), SDSS DR12 (Alam et al., 2015), and SDSS DR16 (Ahumada et al., 2020), we calculate the radio luminosities and linear sizes of these sources. [The ‘(re-fitted)’ label applies to five sources where we corrected the redshift provided in the SDSS database (see Figure 10).] The ‘Confusion flag’ is also from the G4Jy catalogue, and indicates (via ‘1’) whether the *radio* emission of the G4Jy source may be blended with another (unrelated) radio source. An inequality ($<$) in the angular-size column indicates that this value should be treated as an upper limit, as should the angular size for G4Jy sources that are flagged as ‘confused’. See (White et al., 2020a) for further details.

Source name	Confusion flag	Angular size / ''	G4Jy spectral-index	Total $S_{151\text{ MHz}}$ / Jy	Redshift origin	Host-galaxy name	Spectroscopic redshift	$L_{151\text{ MHz}}$ / W Hz ⁻¹	Linear size / kpc
G4Jy3	0	115.7	-1.13 ± 0.01	7.193 ± 0.031	6dFGS	g0003130-355614	0.04973	4.230 × 10 ⁻²⁵ ± 1.821 × 10 ⁻²³	112.5
G4Jy28	0	47.6	-1.11 ± 0.01	7.489 ± 0.025	6dFGS	g0016200-143011	0.76776	2.170 × 10 ⁻²⁸ ± 7.135 × 10 ⁻²⁵	351.9
G4Jy32	0	135.4	-0.76 ± 0.02	4.519 ± 0.041	SDSS DR12	J001815.21+214133.4	0.30261 ± 0.00004	1.248 × 10 ⁻²⁷ ± 1.122 × 10 ⁻²⁵	606.9
G4Jy43	1	61.0	-0.72 ± 0.01	9.982 ± 0.026	SALT	J002308.86-250229.6	0.354 ± 0.001	3.882 × 10 ⁻²⁷ ± 1.004 × 10 ⁻²⁵	303.4
G4Jy44	0	19.1	-0.91 ± 0.01	5.553 ± 0.020	SDSS DR12	J002319.04-074449.3	0.51367 ± 0.00005	5.477 × 10 ⁻²⁷ ± 1.994 × 10 ⁻²⁵	118.3
G4Jy45	0	42.0	-0.86 ± 0.01	16.103 ± 0.023	SALT	J002430.15-292854.3	0.407 ± 0.002	9.020 × 10 ⁻²⁷ ± 1.311 × 10 ⁻²⁵	228.0
G4Jy46	0	24.2	-0.85 ± 0.02	11.459 ± 0.034	SDSS DR16	J003606.45-183759.0	1.47035 ± 0.00024	1.350 × 10 ⁻²⁹ ± 4.033 × 10 ⁻²⁶	204.6
G4Jy47	0	26.1	-0.82 ± 0.01	19.879 ± 0.025	6dFGS	g0037041-010908	0.07333	2.581 × 10 ⁻²⁶ ± 3.191 × 10 ⁻²³	36.4
G4Jy49	1	19.9	-0.71 ± 0.01	28.249 ± 0.033	6dFGS	g0038205-020741	0.22040	3.812 × 10 ⁻²⁷ ± 4.481 × 10 ⁻²⁴	70.8
G4Jy70	0	18.1	-0.90 ± 0.01	11.349 ± 0.020	6dFGS	g0038269-385948	0.59272	1.570 × 10 ⁻²⁸ ± 2.778 × 10 ⁻²⁵	120.3
G4Jy74	0	183.8	-0.86 ± 0.01	7.188 ± 0.033	SDSS DR12	J004052.73+085401.0	0.13018 ± 0.00002	3.159 × 10 ⁻²⁶ ± 1.435 × 10 ⁻²⁴	426.4
G4Jy84	1	151.3	-0.74 ± 0.02	4.267 ± 0.025	6dFGS	g0046050-633319	0.07446	5.685 × 10 ⁻²⁵ ± 3.371 × 10 ⁻²³	214.0
G4Jy85	0	98.0	-0.72 ± 0.01	30.859 ± 0.028	6dFGS	g0046178-420752	0.05277	2.011 × 10 ⁻²⁶ ± 1.802 × 10 ⁻²³	100.7
G4Jy86	1	996.3	—	9.922 ± 0.031	6dFGS	g0047331-251719	0.00083	—	17.2
G4Jy92	1	17.9	-0.76 ± 0.01	7.558 ± 0.034	SDSS DR16	J005147.16+174710.6	1.53626 ± 0.00056	9.169 × 10 ⁻²⁸ ± 4.165 × 10 ⁻²⁶	151.6
G4Jy98	1	18.8	-0.51 ± 0.01	11.394 ± 0.027	SALT	J005408.43-033355.2	0.211 ± 0.001	1.344 × 10 ⁻²⁷ ± 3.191 × 10 ⁻²⁴	64.7
G4Jy99	1	33.1	-1.08 ± 0.02	19.360 ± 0.048	SDSS DR12	J005550.61+262437.2	0.19545 ± 0.00001	2.143 × 10 ⁻²⁷ ± 5.294 × 10 ⁻²⁴	107.3
G4Jy100	0	225.9	-0.73 ± 0.02	4.478 ± 0.052	6dFGS	g0056027-012004	0.04296	1.912 × 10 ⁻²⁵ ± 2.232 × 10 ⁻²³	191.3
G4Jy101	0	243.2	-0.65 ± 0.02	6.019 ± 0.068	6dFGS	g0056256-011545	0.03819	2.014 × 10 ⁻²⁵ ± 2.285 × 10 ⁻²³	184.2
G4Jy104	0	71.4	-0.64 ± 0.01	18.837 ± 0.042	6dFGS	g0057349-012328	0.04494	8.793 × 10 ⁻²⁵ ± 1.967 × 10 ⁻²³	63.1
G4Jy110	1	71.4	-0.77 ± 0.01	4.016 ± 0.024	6dFGS	g0100467-503208	0.06088	3.527 × 10 ⁻²⁵ ± 2.099 × 10 ⁻²³	83.8
G4Jy128	1	57.8	-0.67 ± 0.01	4.230 ± 0.025	6dFGS	g0111091-135740	0.05160	2.626 × 10 ⁻²⁵ ± 1.567 × 10 ⁻²³	58.2
G4Jy131	1	472.3	-0.76 ± 0.02	4.618 ± 0.058	SDSS DR16	J011259.57+152928.7	0.04385 ± 0.00002	2.060 × 10 ⁻²⁵ ± 2.605 × 10 ⁻²³	407.8
G4Jy133	0	543.6	-0.84 ± 0.01	13.949 ± 0.039	6dFGS	g0116251-472241	0.14585	7.809 × 10 ⁻²⁶ ± 2.163 × 10 ⁻²⁴	1388.2
G4Jy139	0	19.3	-0.93 ± 0.01	10.849 ± 0.028	SDSS DR16	J011818.48+025805.7	0.66715 ± 0.00004	2.023 × 10 ⁻²⁸ ± 5.172 × 10 ⁻²⁵	135.2
G4Jy140	1	23.7	-0.79 ± 0.01	6.054 ± 0.021	6dFGS	g0118342-184917	0.27757	1.387 × 10 ⁻²⁷ ± 4.746 × 10 ⁻²⁴	100.0
G4Jy148	0	15.6	-0.42 ± 0.01	4.749 ± 0.023	SDSS DR16 (re-fitted)	J012227.89-042127.1	1.96500 ± 0.00024	6.970 × 10 ⁻²⁸ ± 3.427 × 10 ⁻²⁶	130.8
G4Jy150	1	190.8	-0.92 ± 0.02	4.267 ± 0.035	6dFGS	g0125443-012246	0.01814	3.165 × 10 ⁻²⁴ ± 2.624 × 10 ⁻²²	70.3
G4Jy151	1	846.6	-0.78 ± 0.01	14.220 ± 0.043	6dFGS	g0126006-012043	0.01841	1.084 × 10 ⁻²⁵ ± 3.291 × 10 ⁻²²	316.5
G4Jy159	0	30.5	-0.76 ± 0.02	12.821 ± 0.049	SDSS DR12	J012830.11+290300.8	0.39610 ± 0.00002	6.521 × 10 ⁻²⁷ ± 2.469 × 10 ⁻²⁵	162.9
G4Jy163	0	18.2	-0.63 ± 0.01	4.686 ± 0.029	SDSS DR16	J013107.04+041014.8	1.26030 ± 0.00017	3.221 × 10 ⁻²⁸ ± 2.024 × 10 ⁻²⁶	151.9
G4Jy167	0	71.7	-0.95 ± 0.01	10.948 ± 0.027	SDSS DR12	J013121.65+062343.1	0.65932 ± 0.00003	1.998 × 10 ⁻²⁸ ± 4.552 × 10 ⁻²⁵	499.9

Table 3. *Continued – Angular sizes, spectral indices, 151-MHz flux-densities, redshifts, radio luminosities, and linear sizes for 299 G4Jy sources.*

Source name	Confusion flag	Angular size / ''	G4Jy spectral-index	Total $S_{151\text{ MHz}}$ / Jy	Redshift origin	Host-galaxy name	Spectroscopic redshift	$L_{151\text{ MHz}}$ / W Hz ⁻¹	Linear size / kpc
G4Jy171	0	689.1	-0.71 ± 0.01	32.108 ± 0.061	6dFGS	g0133577-362936	0.03051	$6.812 \times 10^{25} \pm 1.287 \times 10^{23}$	420.7
G4Jy172	1	45.7	-0.76 ± 0.01	8.357 ± 0.018	SALT	J013333.18-444417.7	0.091 ± 0.003	$1.698 \times 10^{26} \pm 3.638 \times 10^{23}$	77.5
G4Jy176	0	17.6	-0.86 ± 0.02	6.453 ± 0.035	SDSS DR16 (re-fitted)	J013813.78+230115.6	1.66000 ± 0.00086	$1.029 \times 10^{29} \pm 5.639 \times 10^{26}$	149.1
G4Jy179	0	16.9	-0.31 ± 0.01	9.129 ± 0.031	SDSS DR16	J014109.16+135328.3	0.23577 ± 0.00006	$1.311 \times 10^{27} \pm 4.388 \times 10^{24}$	63.3
G4Jy184	0	26.2	-0.88 ± 0.01	5.130 ± 0.028	SDSS DR12	J014316.72-0111900.9	0.51931 ± 0.00004	$5.133 \times 10^{27} \pm 2.798 \times 10^{25}$	163.2
G4Jy192	0	111.3	-0.80 ± 0.01	16.595 ± 0.029	SALT	J015035.94-293155.3	0.413 ± 0.003	$9.436 \times 10^{27} \pm 1.643 \times 10^{25}$	609.5
G4Jy203	0	29.3	-0.65 ± 0.02	4.099 ± 0.031	SDSS DR16	J015559.18+033158.1	1.28009 ± 0.00024	$2.949 \times 10^{28} \pm 2.237 \times 10^{26}$	245.1
G4Jy208	0	17.4	-0.69 ± 0.01	9.483 ± 0.027	6dFGS	g0157416-104341	0.61804	$1.308 \times 10^{28} \pm 3.698 \times 10^{25}$	117.9
G4Jy216	0	19.2	-0.44 ± 0.01	7.665 ± 0.026	6dFGS	g0201572-113233	0.67006	$1.121 \times 10^{28} \pm 3.741 \times 10^{25}$	134.8
G4Jy229	0	55.3	-0.47 ± 0.01	6.235 ± 0.016	6dFGS	g0210462-510102	0.03154	$1.404 \times 10^{25} \pm 3.552 \times 10^{22}$	34.9
G4Jy241	0	316.4	-0.78 ± 0.01	10.815 ± 0.035	6dFGS	g0216451-474909	0.06423	$1.062 \times 10^{26} \pm 3.403 \times 10^{23}$	390.7
G4Jy247	0	63.8	-1.00 ± 0.01	9.362 ± 0.024	6dFGS	g0219029-362607	0.48848	$8.492 \times 10^{27} \pm 2.159 \times 10^{25}$	384.8
G4Jy260	0	17.1	-0.78 ± 0.01	10.180 ± 0.022	6dFGS	g0225028-231248	0.23208	$1.560 \times 10^{27} \pm 3.417 \times 10^{24}$	63.3
G4Jy277	0	19.5	-0.75 ± 0.01	6.811 ± 0.023	SDSS DR16	J023507.34-040205.3	1.44207 ± 0.00010	$7.022 \times 10^{28} \pm 2.365 \times 10^{26}$	164.7
G4Jy288	0	16.0	-0.51 ± 0.01	17.886 ± 0.031	6dFGS	g0242407-000048	0.00379	$5.661 \times 10^{23} \pm 9.762 \times 10^{20}$	1.3
G4Jy292	0	89.7	-0.74 ± 0.01	5.671 ± 0.016	6dFGS	g0245541-445939	0.28267	$1.336 \times 10^{27} \pm 3.786 \times 10^{24}$	383.4
G4Jy330	0	89.5	-0.80 ± 0.01	4.071 ± 0.021	6dFGS	g0310015-301940	0.06817	$4.531 \times 10^{25} \pm 2.362 \times 10^{23}$	116.7
G4Jy341	0	54.1	-0.65 ± 0.01	4.181 ± 0.022	6dFGS	g0316393-435117	0.06274	$3.879 \times 10^{25} \pm 2.030 \times 10^{23}$	65.4
G4Jy344	0	57.1	-1.03 ± 0.01	7.305 ± 0.021	6dFGS	g0317577-441417	0.07588	$1.034 \times 10^{26} \pm 2.951 \times 10^{23}$	82.2
G4Jy361	1	15.7	-0.79 ± 0.01	7.137 ± 0.021	6dFGS	g0328365-284156	0.10869	$2.117 \times 10^{26} \pm 6.251 \times 10^{23}$	31.2
G4Jy366	0	276.9	-0.79 ± 0.01	8.374 ± 0.046	6dFGS	g0334033-390036	0.06227	$7.716 \times 10^{25} \pm 4.269 \times 10^{23}$	332.2
G4Jy373	0	88.8	-0.83 ± 0.01	10.028 ± 0.019	SALT	J033846.01-352252.0	0.113 ± 0.001	$3.242 \times 10^{26} \pm 6.208 \times 10^{23}$	182.4
G4Jy377	0	15.2	-0.64 ± 0.01	7.407 ± 0.022	6dFGS	g0342054-370322	0.28380	$1.719 \times 10^{27} \pm 5.067 \times 10^{24}$	65.1
G4Jy381	0	283.6	-0.75 ± 0.01	16.692 ± 0.041	6dFGS	g0346306-342246	0.05346	$1.119 \times 10^{26} \pm 2.768 \times 10^{23}$	295.3
G4Jy386	0	355.0	-0.80 ± 0.01	27.550 ± 0.052	6dFGS	g0351358-274435	0.06565	$2.835 \times 10^{26} \pm 5.337 \times 10^{23}$	447.3
G4Jy392	0	56.7	-0.84 ± 0.01	20.011 ± 0.027	SDSS DR12	J035230.55-071102.3	0.96354 ± 0.00011	$8.561 \times 10^{28} \pm 1.147 \times 10^{26}$	449.8
G4Jy411	0	18.1	–	9.072 ± 0.025	6dFGS	g0405340-130814	0.57428	–	118.5
G4Jy423	0	36.2	-0.71 ± 0.01	7.596 ± 0.020	6dFGS	g0411594-643624	0.15507	$4.770 \times 10^{26} \pm 1.246 \times 10^{24}$	97.3
G4Jy437	0	21.5	-1.10 ± 0.01	8.600 ± 0.024	6dFGS	g0417168-055345	0.77465	$2.534 \times 10^{28} \pm 7.027 \times 10^{25}$	159.6
G4Jy462	0	345.4	-0.67 ± 0.01	25.569 ± 0.044	6dFGS	g0429082-534940	0.03797	$8.463 \times 10^{25} \pm 1.468 \times 10^{23}$	260.1
G4Jy466	1	104.7	-0.65 ± 0.01	7.592 ± 0.031	6dFGS	g0430220-613201	0.05546	$5.460 \times 10^{25} \pm 2.258 \times 10^{23}$	112.7
G4Jy475	1	305.0	-0.77 ± 0.02	4.066 ± 0.054	6dFGS	g0434104-132212	0.03487	$1.134 \times 10^{25} \pm 1.500 \times 10^{23}$	211.7
G4Jy479	0	115.2	-0.67 ± 0.01	4.390 ± 0.026	6dFGS	g0436354-222639	0.06895	$4.961 \times 10^{25} \pm 2.984 \times 10^{23}$	151.9
G4Jy492	0	59.1	-0.76 ± 0.01	37.342 ± 0.034	SALT	J044437.70-280954.3	0.148 ± 0.001	$2.135 \times 10^{27} \pm 1.954 \times 10^{24}$	152.8
G4Jy495	1	71.1	-0.96 ± 0.01	4.284 ± 0.021	6dFGS	g0445106-383835	0.53609	$4.781 \times 10^{27} \pm 2.309 \times 10^{25}$	450.0

Table 3. *Continued* – Angular sizes, spectral indices, 151-MHz flux-densities, redshifts, radio luminosities, and linear sizes for 299 G4-ly sources.

Source name	Confusion flag	Angular size / ''	G4Jy spectral-index	Total S_{151} MHz / Jy	Redshift origin	Host-galaxy name	Spectroscopic redshift	L_{151} MHz / W Hz ⁻¹	Linear size / kpc
G4Jy 499	1	196.8	-0.93 ± 0.01	4.274 ± 0.029	6dFGS	g0448306-203214	0.07393	$5.687 \times 10^{-25} \pm 3.902 \times 10^{-23}$	276.6
G4Jy 510	1	73.3	-0.78 ± 0.01	10.007 ± 0.024	6dFGS	g0456089-215909	0.27821	$2.302 \times 10^{-27} \pm 5.557 \times 10^{-24}$	309.7
G4Jy 516	1	18.8	-0.87 ± 0.01	9.057 ± 0.024	6dFGS	g0504531-101453	0.04032	$3.415 \times 10^{-25} \pm 9.069 \times 10^{-22}$	15.0
G4Jy 517	1	2143.5	–	9.538 ± 0.096	6dFGS	g0505492-283519	0.03812	–	1620.3
G4Jy 530	1	109.9	-0.86 ± 0.01	16.768 ± 0.033	SALT	WISEA J051247.41-482416.5	0.305 ± 0.002	$4.838 \times 10^{-27} \pm 9.478 \times 10^{-24}$	495.2
G4Jy 536	0	54.3	-0.76 ± 0.01	6.739 ± 0.024	6dFGS	g0518264-561413	0.09480	$1.491 \times 10^{-26} \pm 5.228 \times 10^{-23}$	95.5
G4Jy 540	0	5.0	-0.62 ± 0.01	55.942 ± 0.032	6dFGS	g0522580-362731	0.05651	$4.175 \times 10^{-26} \pm 2.362 \times 10^{-23}$	5.5
G4Jy 541	0	65.1	-0.81 ± 0.01	4.793 ± 0.020	SALT	J052320.72-481630.6	0.200 ± 0.007	$5.324 \times 10^{-26} \pm 2.229 \times 10^{-24}$	214.9
G4Jy 543	0	283.1	-0.77 ± 0.01	5.806 ± 0.030	6dFGS	g0525272-324216	0.07676	$8.262 \times 10^{-25} \pm 4.268 \times 10^{-23}$	411.7
G4Jy 579	0	522.5	-0.69 ± 0.02	4.348 ± 0.036	6dFGS	g0548276-325638	0.03716	$1.378 \times 10^{-25} \pm 1.125 \times 10^{-23}$	385.5
G4Jy 590	0	77.9	-0.95 ± 0.01	9.785 ± 0.022	SALT	J060312.22-342632.6	0.529 ± 0.002	$1.054 \times 10^{-28} \pm 2.319 \times 10^{-25}$	489.5
G4Jy 592	1	18.6	-0.95 ± 0.01	5.698 ± 0.020	6dFGS	g0605540-351808	0.14115	$3.016 \times 10^{-26} \pm 1.038 \times 10^{-24}$	46.2
G4Jy 604	0	881.9	-0.76 ± 0.02	5.962 ± 0.058	SALT	J061813.03-484458.3	0.049 ± 0.003	$3.342 \times 10^{-25} \pm 3.235 \times 10^{-23}$	845.8
G4Jy 606	0	47.3	–	7.656 ± 0.019	6dFGS	g0621013-450440	0.20818	–	161.0
G4Jy 607	0	178.6	-0.83 ± 0.01	13.938 ± 0.031	6dFGS	g0621433-524133	0.05107	$8.535 \times 10^{-25} \pm 1.904 \times 10^{-23}$	178.1
G4Jy 611	0	59.7	-1.02 ± 0.01	46.864 ± 0.037	SALT	WISEA J062620.46-534135.1	0.055 ± 0.001	$3.379 \times 10^{-26} \pm 2.700 \times 10^{-23}$	63.8
G4Jy 613	0	194.1	-0.89 ± 0.01	19.702 ± 0.035	6dFGS	g0626496-543234	0.05171	$1.242 \times 10^{-26} \pm 2.195 \times 10^{-23}$	195.8
G4Jy 614	0	94.2	-0.73 ± 0.01	16.577 ± 0.024	6dFGS	g0627067-352915	0.05482	$1.169 \times 10^{-26} \pm 1.671 \times 10^{-23}$	100.4
G4Jy 615	0	84.6	-1.14 ± 0.01	5.104 ± 0.020	6dFGS	g0628498-414337	0.17826	$4.649 \times 10^{-26} \pm 1.845 \times 10^{-24}$	254.8
G4Jy 619	0	806.4	-0.75 ± 0.01	41.188 ± 0.099	6dFGS	g0636323-203453	0.05501	$2.929 \times 10^{-26} \pm 7.034 \times 10^{-23}$	862.1
G4Jy 627	1	204.7	-0.78 ± 0.01	6.732 ± 0.023	6dFGS	g0644251-434349	0.06142	$6.024 \times 10^{-25} \pm 2.030 \times 10^{-23}$	242.5
G4Jy 631	1	123.4	-0.81 ± 0.01	5.286 ± 0.029	6dFGS	g0650215-554933	0.04969	$3.056 \times 10^{-25} \pm 1.705 \times 10^{-23}$	119.9
G4Jy 633	0	103.8	-0.79 ± 0.01	5.837 ± 0.020	6dFGS	g0651549-602217	0.13380	$2.699 \times 10^{-26} \pm 9.333 \times 10^{-23}$	246.5
G4Jy 641	1	255.8	-0.94 ± 0.02	5.504 ± 0.037	SALT	WISEA J070532.94-451308.8	0.128 ± 0.002	$2.354 \times 10^{-26} \pm 1.569 \times 10^{-24}$	584.9
G4Jy 651	0	211.8	-0.81 ± 0.01	11.948 ± 0.035	6dFGS	g0717081-362159	0.03134	$2.684 \times 10^{-25} \pm 7.841 \times 10^{-22}$	132.7
G4Jy 672	0	25.1	-0.62 ± 0.01	11.568 ± 0.027	SALT	WISEA J074331.61-672625.5	1.510 ± 0.001	$1.182 \times 10^{-20} \pm 2.809 \times 10^{-26}$	212.5
G4Jy 679	0	16.6	-0.79 ± 0.01	16.760 ± 0.032	SDSS DR12 (re-fitted)	J080133.55+141442.8	1.19600 ± 0.00010	$1.155 \times 10^{-20} \pm 2.218 \times 10^{-26}$	137.6
G4Jy 682	0	16.1	-0.87 ± 0.01	14.441 ± 0.030	SDSS DR16	J080447.96+101523.7	1.96818 ± 0.00016	$3.481 \times 10^{-20} \pm 7.222 \times 10^{-26}$	135.0
G4Jy 683	0	97.3	-0.74 ± 0.02	23.065 ± 0.046	SDSS DR12	J080535.00+240950.3	0.05968 ± 0.00001	$1.940 \times 10^{-26} \pm 3.905 \times 10^{-23}$	112.3
G4Jy 685	1	86.2	-0.88 ± 0.01	22.306 ± 0.034	6dFGS	g0808536-102740	0.10891	$6.705 \times 10^{-26} \pm 1.033 \times 10^{-24}$	171.4
G4Jy 692	1	18.1	-1.07 ± 0.01	22.731 ± 0.033	SALT	J081527.81-030826.6	0.198 ± 0.001	$2.589 \times 10^{-27} \pm 3.802 \times 10^{-24}$	59.3
G4Jy 699	0	16.5	–	5.316 ± 0.032	SDSS DR12	J082144.02+174820.2	0.29699 ± 0.00008	–	73.0
G4Jy 706	0	19.3	-0.62 ± 0.01	17.804 ± 0.022	SALT	J082717.41-202624.8	0.828 ± 0.004	$4.645 \times 10^{-28} \pm 5.828 \times 10^{-25}$	146.6
G4Jy 722	0	19.5	-0.73 ± 0.01	11.758 ± 0.026	SDSS DR12	J084047.58+131223.5	0.68038 ± 0.00007	$2.074 \times 10^{-28} \pm 4.603 \times 10^{-25}$	137.7
G4Jy 725	0	63.9	-0.90 ± 0.02	6.178 ± 0.048	SDSS DR12	J084309.85+294404.6	0.39797 ± 0.00002	$3.332 \times 10^{-27} \pm 2.601 \times 10^{-25}$	342.1

Table 3. *Continued – Angular sizes, spectral indices, 151-MHz flux-densities, redshifts, radio luminosities, and linear sizes for 299 G4Jy sources.*

Source name	Confusion flag	Angular size / ''	G4Jy spectral-index	Total $S_{151\text{MHz}}$ / Jy	Redshift origin	Host-galaxy name	Spectroscopic redshift	$L_{151\text{MHz}} / \text{W Hz}^{-1}$	Linear size / kpc
G4Jy728	1	79.3	–	5.119 ± 0.027	SDSS DR16	J084605.09+145928.3	0.67560 ± 0.00004	–	558.5
G4Jy741	0	16.5	–	12.711 ± 0.042	SDSS DR16	J085810.02+275053.8	0.23017 ± 0.00008	–	60.7
G4Jy745	0	57.7	-0.77 ± 0.02	6.473 ± 0.032	SDSS DR16	J090048.22+183226.0	0.60078 ± 0.00005	$8.704 \times 10^{27} \pm 4.266 \times 10^{25}$	385.9
G4Jy750	1	44.2	-0.78 ± 0.02	4.263 ± 0.023	SDSS DR12	J090604.06+110328.7	0.41658 ± 0.00005	$2.453 \times 10^{27} \pm 1.332 \times 10^{25}$	243.4
G4Jy751	0	39.6	–	11.496 ± 0.027	SDSS DR12	J090631.87+164611.8	0.41106 ± 0.00004	–	216.3
G4Jy755	0	19.2	–	4.596 ± 0.029	SDSS DR16	J091022.55+241919.5	0.90674 ± 0.00011	–	149.9
G4Jy760	0	48.0	–	7.789 ± 0.030	SDSS DR12	J091405.21+171554.3	0.51998 ± 0.00004	–	299.1
G4Jy770	1	51.6	–	5.637 ± 0.024	SDSS DR12	J092507.27+144425.6	0.89615 ± 0.00007	–	401.5
G4Jy786	0	56.0	-0.67 ± 0.01	4.791 ± 0.028	SDSS DR12	J094319.23-000424.8	0.46432 ± 0.00005	$3.392 \times 10^{27} \pm 1.978 \times 10^{25}$	328.5
G4Jy794	0	188.3	–	37.273 ± 0.042	SDSS DR16	J094745.14+072520.5	0.08556 ± 0.00004	–	302.2
G4Jy797	0	53.7	–	16.766 ± 0.028	SDSS DR16	J095010.79+142000.6	0.55183 ± 0.00002	–	344.9
G4Jy809	0	34.4	-0.60 ± 0.02	4.597 ± 0.026	SDSS DR12	J100021.80+223318.6	0.41893 ± 0.00002	$2.519 \times 10^{27} \pm 1.423 \times 10^{25}$	190.0
G4Jy816	1	111.6	-0.97 ± 0.01	5.030 ± 0.022	6dFGS	g1004400-321642	0.08842	$9.792 \times 10^{25} \pm 4.192 \times 10^{23}$	184.4
G4Jy817	0	58.3	-0.83 ± 0.02	4.403 ± 0.030	SDSS DR16	J100445.74+222519.2	0.98061 ± 0.00005	$1.954 \times 10^{28} \pm 1.326 \times 10^{26}$	464.5
G4Jy820	1	86.5	–	5.595 ± 0.026	SDSS DR16	J100726.10+124856.2	0.24074 ± 0.00008	–	328.8
G4Jy829	0	49.6	-0.98 ± 0.01	5.735 ± 0.018	6dFGS	g101329/-283126	0.25482	$1.133 \times 10^{27} \pm 3.605 \times 10^{24}$	196.8
G4Jy832	0	17.3	–	4.129 ± 0.044	SDSS DR16	J101418.79+290400.3	0.37828 ± 0.00002	–	89.8
G4Jy834	1	16.7	-0.74 ± 0.02	5.687 ± 0.037	SDSS DR16	J101749.37+273204.1	0.46792 ± 0.00002	$4.220 \times 10^{27} \pm 2.721 \times 10^{25}$	98.3
G4Jy842	0	19.5	-0.89 ± 0.02	4.199 ± 0.023	SDSS DR16	J102459.80+062453.7	1.73621 ± 0.00080	$7.679 \times 10^{28} \pm 4.173 \times 10^{26}$	165.0
G4Jy843	0	75.1	-0.87 ± 0.02	7.397 ± 0.032	SDSS DR16	J102520.80+201020.0	0.43687 ± 0.00004	$4.911 \times 10^{27} \pm 2.140 \times 10^{25}$	425.2
G4Jy845	0	16.8	-1.08 ± 0.01	9.493 ± 0.024	SDSS DR12 (re-fitted)	J102631.95+062733.0	1.70600 ± 0.00015	$2.012 \times 10^{29} \pm 5.145 \times 10^{26}$	142.2
G4Jy852	0	53.8	–	5.543 ± 0.036	SDSS DR16	J103244.38+250223.0	0.52416 ± 0.00003	–	336.8
G4Jy864	0	17.0	-0.56 ± 0.01	9.295 ± 0.027	SDSS DR16	J104138.98+024231.4	0.53395 ± 0.00008	$8.662 \times 10^{27} \pm 2.486 \times 10^{25}$	107.4
G4Jy865	0	17.9	-0.89 ± 0.01	13.049 ± 0.027	SDSS DR12	J104244.60+120331.2	1.02860 ± 0.00011	$6.749 \times 10^{28} \pm 1.414 \times 10^{26}$	144.3
G4Jy876	1	76.7	-0.82 ± 0.01	10.110 ± 0.024	6dFGS	g1051299-091810	0.34506	$3.830 \times 10^{27} \pm 9.147 \times 10^{24}$	375.2
G4Jy881	0	35.0	-1.09 ± 0.01	4.950 ± 0.027	SDSS DR12	J105517.27+020544.9	0.87529 ± 0.00027	$1.974 \times 10^{28} \pm 1.096 \times 10^{26}$	270.5
G4Jy882	0	25.5	-0.64 ± 0.01	5.964 ± 0.019	6dFGS	g1055334-283134	0.06103	$5.225 \times 10^{25} \pm 1.630 \times 10^{23}$	30.0
G4Jy884	0	30.2	–	8.476 ± 0.033	SDSS DR12	J105817.90+195150.9	1.11592 ± 0.00007	–	247.2
G4Jy885	0	19.6	-0.31 ± 0.01	4.833 ± 0.025	SDSS DR16	J105829.60+013358.8	0.89193 ± 0.00062	$1.223 \times 10^{28} \pm 6.436 \times 10^{25}$	152.3
G4Jy886	1	237.4	-0.79 ± 0.01	7.410 ± 0.029	6dFGS	g1058548-361921	0.07047	$8.834 \times 10^{25} \pm 3.514 \times 10^{23}$	319.3
G4Jy891	0	56.9	-0.89 ± 0.01	4.382 ± 0.016	6dFGS	g1103316-325117	0.35526	$1.811 \times 10^{27} \pm 6.648 \times 10^{24}$	283.8
G4Jy893	1	61.7	-1.02 ± 0.01	8.861 ± 0.019	6dFGS	g1106121-244444	0.04997	$5.236 \times 10^{25} \pm 1.111 \times 10^{23}$	60.3
G4Jy895	0	19.3	-0.84 ± 0.01	4.848 ± 0.024	SDSS DR16	J110631.77-005252.3	0.42370 ± 0.00002	$2.966 \times 10^{27} \pm 1.498 \times 10^{25}$	107.3
G4Jy901	0	20.8	-0.72 ± 0.01	5.714 ± 0.020	SALT	WISEAJ11119.43-403051.9	0.725 ± 0.002	$1.158 \times 10^{28} \pm 3.996 \times 10^{25}$	150.7
G4Jy903	0	56.1	-0.82 ± 0.01	8.932 ± 0.026	SDSS DR16	J111332.49-021253.3	0.47543 ± 0.00003	$7.099 \times 10^{27} \pm 2.074 \times 10^{25}$	333.5

Table 3. *Continued* – Angular sizes, spectral indices, 151-MHz flux-densities, redshifts, radio luminosities, and linear sizes for 299 G4-Jy sources.

Source name	Confusion flag	Angular size / ''	G4-Jy spectral-index	Total $S_{151\text{ MHz}}$ / Jy	Redshift origin	Host-galaxy name	Spectroscopic redshift	$L_{151\text{ MHz}}$ / W Hz ⁻¹	Linear size / kpc
G4-Jy 906	1	67.9	-0.73 ± 0.03	7.323 ± 0.057	SDSS DR12	J111634.61+291517.1	0.04888 ± 0.00001	$4.0444 \times 10^{-25} \pm 3.148 \times 10^{-23}$	64.7
G4-Jy 909	0	62.2	-0.74 ± 0.01	8.948 ± 0.024	SALT	J111826.95+463414.9	0.714 ± 0.001	$1.770 \times 10^{-28} \pm 4.720 \times 10^{-25}$	447.9
G4-Jy 910	0	18.3	–	4.228 ± 0.030	SDSS DR16	J111857.29+123441.7	2.1258 ± 0.00027	–	152.0
G4-Jy 916	1	16.5	-0.81 ± 0.01	6.335 ± 0.037	SDSS DR16	J112437.40+045618.9	0.28280 ± 0.00002	$1.521 \times 10^{-27} \pm 8.977 \times 10^{-24}$	70.5
G4-Jy 917	0	103.6	-0.73 ± 0.01	11.328 ± 0.022	6dFGS	g1125529-352340	0.03262	$2.755 \times 10^{-25} \pm 5.316 \times 10^{-22}$	67.4
G4-Jy 919	1	15.8	-0.94 ± 0.01	6.408 ± 0.028	SDSS DR16	J112627.12+122034.8	1.09920 ± 0.00013	$4.053 \times 10^{-28} \pm 1.798 \times 10^{-26}$	129.1
G4-Jy 924	0	16.6	-0.82 ± 0.02	4.340 ± 0.028	SDSS DR16	J113259.49+102342.2	0.53963 ± 0.00004	$4.640 \times 10^{-27} \pm 2.989 \times 10^{-25}$	105.4
G4-Jy 933	1	15.9	-0.78 ± 0.01	19.350 ± 0.025	6dFGS	g1139107-135043	0.55607	$2.181 \times 10^{-28} \pm 2.799 \times 10^{-25}$	102.5
G4-Jy 936	0	78.4	–	5.772 ± 0.034	SDSS DR12	J114027.73+120308.2	0.0815 ± 0.00001	–	119.9
G4-Jy 944	0	26.5	-1.00 ± 0.02	7.935 ± 0.053	SDSS DR12	J114257.21+212911.2	1.37303 ± 0.00010	$9.096 \times 10^{-28} \pm 6.070 \times 10^{-26}$	223.1
G4-Jy 949	0	219.9	–	22.096 ± 0.077	SDSS DR12	J114505.01+193622.8	0.02160 ± 0.00001	–	96.1
G4-Jy 957	0	227.6	-0.86 ± 0.01	9.692 ± 0.042	SALT	J114906.68-120433.4	0.119 ± 0.002	$3.513 \times 10^{-26} \pm 1.510 \times 10^{-24}$	488.8
G4-Jy 965	1	17.5	–	8.868 ± 0.018	SALT	J115421.78-350529.0	0.258 ± 0.001	–	70.0
G4-Jy 966	0	176.9	-0.79 ± 0.03	6.082 ± 0.081	SDSS DR12	J115820.13+262112.0	0.11202 ± 0.00002	$1.924 \times 10^{-26} \pm 2.556 \times 10^{-24}$	360.6
G4-Jy 968	0	14.0	-0.78 ± 0.04	4.077 ± 0.071	SDSS DR12	J115931.83+291443.8	0.72475 ± 0.00010	$8.535 \times 10^{-27} \pm 1.477 \times 10^{-26}$	101.4
G4-Jy 975	0	17.8	-0.80 ± 0.01	8.563 ± 0.041	SDSS DR12	J120620.12+040610.7	0.53604 ± 0.00005	$8.913 \times 10^{-27} \pm 4.300 \times 10^{-25}$	112.7
G4-Jy 979	1	64.8	-0.78 ± 0.01	5.509 ± 0.029	6dFGS	g1214188-415954	0.06918	$6.312 \times 10^{-25} \pm 3.278 \times 10^{-23}$	85.7
G4-Jy 984	0	24.8	-0.95 ± 0.01	7.872 ± 0.047	SDSS DR12	J121738.77+033948.2	0.07784 ± 0.00002	$1.169 \times 10^{-26} \pm 7.046 \times 10^{-23}$	36.5
G4-Jy 985	0	14.7	-0.81 ± 0.03	4.781 ± 0.054	SDSS DR12	J121756.88+252927.5	0.67890 ± 0.00007	$8.727 \times 10^{-27} \pm 9.935 \times 10^{-25}$	103.7
G4-Jy 987	0	275.1	-0.84 ± 0.01	14.127 ± 0.051	6dFGS	g1218380-102035	0.08734	$2.650 \times 10^{-26} \pm 9.621 \times 10^{-23}$	449.6
G4-Jy 988	0	77.4	-0.72 ± 0.03	4.648 ± 0.054	SDSS DR12	J121859.14+195528.0	0.42442 ± 0.00002	$2.732 \times 10^{-27} \pm 3.145 \times 10^{-25}$	430.9
G4-Jy 991	1	17.3	-0.99 ± 0.02	8.746 ± 0.045	SDSS DR12	J122027.98+092827.3	1.08013 ± 0.00023	$5.519 \times 10^{-28} \pm 2.827 \times 10^{-26}$	140.9
G4-Jy 993	0	18.7	-0.77 ± 0.03	4.167 ± 0.053	SDSS DR12	J122044.89+223404.7	1.87646 ± 0.00011	$8.098 \times 10^{-28} \pm 1.027 \times 10^{-27}$	157.5
G4-Jy 994	1	57.1	–	7.344 ± 0.029	6dFGS	g1223434-423532	0.02658	–	30.5
G4-Jy 995	1	59.0	-0.90 ± 0.03	4.292 ± 0.066	SDSS DR16	J122433.28+261315.0	0.58266 ± 0.00009	$5.684 \times 10^{-27} \pm 8.798 \times 10^{-25}$	389.1
G4-Jy 997	0	14.7	-0.69 ± 0.02	6.103 ± 0.049	SDSS DR12	J122454.46+21246.4	0.43383 ± 0.00006	$3.740 \times 10^{-27} \pm 2.974 \times 10^{-25}$	82.9
G4-Jy 1001	0	73.6	-0.61 ± 0.03	4.830 ± 0.058	SDSS DR16	J122811.73+20352.4	0.70004 ± 0.00006	$8.540 \times 10^{-27} \pm 1.028 \times 10^{-26}$	525.8
G4-Jy 1005	0	14.1	-1.00 ± 0.01	7.876 ± 0.030	SDSS DR12	J123200.01-022404.7	1.04313 ± 0.00011	$4.570 \times 10^{-28} \pm 1.762 \times 10^{-26}$	114.0
G4-Jy 1007	0	16.4	-0.87 ± 0.01	4.028 ± 0.020	6dFGS	g1232431-244552	0.25682	$7.896 \times 10^{-26} \pm 3.975 \times 10^{-24}$	65.4
G4-Jy 1008	0	118.1	–	18.191 ± 0.068	SDSS DR16	J123526.66+212034.7	0.42266 ± 0.00004	–	656.0
G4-Jy 1009	1	100.4	-0.86 ± 0.01	12.563 ± 0.028	6dFGS	g1235378-251217	0.35496	$5.138 \times 10^{-27} \pm 1.138 \times 10^{-25}$	500.3
G4-Jy 1011	0	191.0	-0.92 ± 0.02	7.802 ± 0.083	SDSS DR12	J123625.77+163218.3	0.06846 ± 0.00001	$8.832 \times 10^{-25} \pm 9.395 \times 10^{-23}$	250.2
G4-Jy 1012	0	24.8	–	4.709 ± 0.066	SDSS DR16	J123631.31+263508.6	1.39871 ± 0.00035	–	209.1
G4-Jy 1019	0	15.8	–	16.680 ± 0.061	SDSS DR16	J124357.65+162253.3	0.55533 ± 0.00004	–	101.8
G4-Jy 1029	0	48.2	-0.79 ± 0.02	4.006 ± 0.039	SDSS DR12	J125222.61+03154.0	0.09835 ± 0.00002	$9.712 \times 10^{-25} \pm 9.420 \times 10^{-23}$	88.0

Table 3. *Continued* – Angular sizes, spectral indices, 151-MHz flux-densities, redshifts, radio luminosities, and linear sizes for 299 G4Jy sources.

Source name	Confusion flag	Angular size / ''	G4Jy spectral-index	Total $S_{151\text{MHz}}$ / Jy	Redshift origin	Host-galaxy name	Spectroscopic redshift	$L_{151\text{MHz}}$ / W Hz^{-1}	Linear size / kpc
G4Jy 1032	0	31.9	–	9.493 ± 0.075	SDSS DR12	J125412.00+273733.9	0.08552 ± 0.00001	–	51.3
G4Jy 1034	0	172.8	-0.73 ± 0.01	30.746 ± 0.053	6dFGS	g1254357-123407	0.01317	$1.190 \times 10^{25} \pm 2.032 \times 10^{22}$	46.5
G4Jy 1035	1	24.9	-1.19 ± 0.01	13.365 ± 0.034	6dFGS	g1254410-291340	0.05736	$1.062 \times 10^{26} \pm 2.731 \times 10^{23}$	27.7
G4Jy 1039	0	23.2	-0.82 ± 0.01	6.164 ± 0.025	6dFGS	g1257206-333444	0.18987	$6.115 \times 10^{26} \pm 2.445 \times 10^{24}$	73.5
G4Jy 1040	1	40.9	-1.07 ± 0.01	6.550 ± 0.027	6dFGS	g1257219-302149	0.05422	$4.598 \times 10^{25} \pm 1.906 \times 10^{23}$	43.1
G4Jy 1044	0	69.7	-0.73 ± 0.02	4.713 ± 0.026	6dFGS	g1301008-322629	0.01701	$3.059 \times 10^{24} \pm 1.676 \times 10^{22}$	24.1
G4Jy 1051	0	46.1	–	6.588 ± 0.039	SDSS DR12	J130753.92+06213.8	0.60139 ± 0.00007	–	308.5
G4Jy 1060	0	190.3	–	6.211 ± 0.044	SDSS DR12	J131617.01+070246.6	0.05022 ± 0.00001	–	186.8
G4Jy 1062	0	15.9	-0.63 ± 0.01	5.995 ± 0.028	SDSS DR12	J131938.76-004940.0	0.89114 ± 0.00006	$1.857 \times 10^{28} \pm 8.814 \times 10^{25}$	123.5
G4Jy 1065	1	15.2	-0.69 ± 0.01	8.900 ± 0.038	SDSS DR12	J132118.83+110649.9	2.17827 ± 0.00015	$2.210 \times 10^{29} \pm 9.377 \times 10^{26}$	125.8
G4Jy 1066	0	74.5	-0.89 ± 0.01	7.607 ± 0.037	SDSS DR16	J132318.81+030807.1	0.26893 ± 0.00004	$1.662 \times 10^{27} \pm 8.165 \times 10^{24}$	307.2
G4Jy 1068	1	70.6	-0.89 ± 0.01	6.611 ± 0.027	SDSS DR12	J132738.22-020309.9	0.18269 ± 0.00002	$6.096 \times 10^{26} \pm 2.520 \times 10^{24}$	216.7
G4Jy 1075	0	109.3	-0.73 ± 0.01	10.569 ± 0.044	SDSS DR16	J133253.26+020455.6	0.21582 ± 0.00003	$1.368 \times 10^{27} \pm 5.743 \times 10^{24}$	382.5
G4Jy 1079	1	807.8	-0.95 ± 0.02	13.707 ± 0.173	6dFGS	g1334186-100929	0.08372	$2.372 \times 10^{26} \pm 2.996 \times 10^{24}$	1270.8
G4Jy 1081	0	197.6	–	8.366 ± 0.070	6dFGS	g1337005-295160	0.00170	–	7.0
G4Jy 1084	0	18.5	-0.71 ± 0.02	4.535 ± 0.033	SDSS DR16	J133932.44+014522.5	0.56669 ± 0.00004	$5.164 \times 10^{27} \pm 3.806 \times 10^{25}$	120.4
G4Jy 1086	0	19.5	-0.73 ± 0.01	6.266 ± 0.035	SDSS DR12	J134243.62+050432.2	0.13648 ± 0.00001	$2.997 \times 10^{26} \pm 1.654 \times 10^{24}$	47.1
G4Jy 1094	0	77.5	-1.17 ± 0.01	4.116 ± 0.027	6dFGS	g1348542-252724	0.12612	$1.754 \times 10^{26} \pm 1.149 \times 10^{24}$	175.0
G4Jy 1108	0	26.4	–	7.931 ± 0.042	SDSS DR12	J135704.43+191907.3	0.71967 ± 0.00001	–	190.7
G4Jy 1110	0	368.3	-0.77 ± 0.01	8.850 ± 0.047	6dFGS	g140149-113625	0.03797	$2.940 \times 10^{25} \pm 1.568 \times 10^{23}$	277.4
G4Jy 1112	0	34.4	-0.84 ± 0.01	5.030 ± 0.032	SALT	J140231.57+021546.5	0.180 ± 0.003	$4.456 \times 10^{26} \pm 2.855 \times 10^{24}$	104.4
G4Jy 1122	0	47.6	-0.86 ± 0.01	7.044 ± 0.027	SDSS DR16	J140648.61-015416.4	0.63993 ± 0.00012	$1.148 \times 10^{28} \pm 4.430 \times 10^{25}$	327.6
G4Jy 1127	0	43.8	-1.06 ± 0.02	4.339 ± 0.072	6dFGS	g1413319-300244	0.06486	$4.427 \times 10^{25} \pm 7.356 \times 10^{23}$	54.6
G4Jy 1135	0	186.5	-0.89 ± 0.01	11.445 ± 0.079	SALT	J141633.15-364053.7	0.075 ± 0.001	$1.564 \times 10^{26} \pm 1.081 \times 10^{24}$	265.6
G4Jy 1137	0	317.0	-0.55 ± 0.01	11.805 ± 0.053	SDSS DR12	J141652.94+104826.7	0.02471 ± 0.00001	$1.624 \times 10^{25} \pm 7.275 \times 10^{22}$	157.8
G4Jy 1145	0	61.6	-0.87 ± 0.01	9.797 ± 0.023	6dFGS	g1419497-192826	0.11990	$3.614 \times 10^{26} \pm 8.323 \times 10^{23}$	133.2
G4Jy 1157	1	59.8	-1.06 ± 0.01	15.118 ± 0.066	SALT	J142416.47-382647.6	0.406 ± 0.001	$9.022 \times 10^{27} \pm 3.967 \times 10^{25}$	324.5
G4Jy 1163	0	21.3	–	7.566 ± 0.047	SDSS DR12	J142550.71+240403.3	0.65300 ± 0.00004	–	147.9
G4Jy 1173	0	68.3	–	10.567 ± 0.093	SDSS DR12	J142955.37+071512.8	0.05599 ± 0.00001	–	731.6
G4Jy 1177	0	19.5	–	4.225 ± 0.040	SDSS DR16	J143556.61+172934.6	1.20212 ± 0.00015	–	161.8
G4Jy 1182	0	46.4	–	5.590 ± 0.053	SDSS DR16	J143821.86+034013.2	0.22468 ± 0.00004	–	167.5
G4Jy 1184	0	18.6	-0.55 ± 0.01	8.604 ± 0.023	6dFGS	g1439287-165905	0.14570	$4.621 \times 10^{26} \pm 1.232 \times 10^{24}$	47.5
G4Jy 1189	0	36.5	–	4.066 ± 0.037	SDSS DR16	J144631.52+072900.0	0.74211 ± 0.00005	–	266.8
G4Jy 1199	0	70.8	–	4.015 ± 0.035	SDSS DR12	J145353.90+093423.2	0.62711 ± 0.00002	–	483.1
G4Jy 1200	1	294.2	–	7.184 ± 0.065	SDSS DR16	J145423.45+162119.0	0.04528 ± 0.00001	–	261.9

Table 3. *Continued* – Angular sizes, spectral indices, 151-MHz flux-densities, redshifts, radio luminosities, and linear sizes for 299 G4Jy sources.

Source name	Confusion flag	Angular size / ''	G4Jy spectral-index	Total $S_{151\text{ MHz}}$ / Jy	Redshift origin	Host-galaxy name	Spectroscopic redshift	$L_{151\text{ MHz}}$ / W Hz ⁻¹	Linear size / kpc
G4Jy 1202	0	42.9	-0.78 ± 0.02	4.840 ± 0.050	6dFGS SALT	g1454274-374733 J145428.22-364004.7	0.31384 0.420 ± 0.001	1.458 × 10 ²⁷ ± 1.151 × 10 ²⁵ 1.260 × 10 ²⁸ ± 3.831 × 10 ²⁵	197.1
G4Jy 1203	1	124.3	-1.03 ± 0.01	19.718 ± 0.060	6dFGS	g1455096-365508	0.09459	1.562 × 10 ²⁶ ± 1.436 × 10 ²⁴	687.7
G4Jy 1205	0	90.6	-0.95 ± 0.02	6.970 ± 0.064	SDSS DR12	J145605.67+162654.8	0.28713 ± 0.00006	–	159.1
G4Jy 1210	1	89.4	–	7.392 ± 0.044	SDSS DR12	J145753.81+283218.7	0.14404 ± 0.00001	2.775 × 10 ²⁶ ± 5.056 × 10 ²⁴	386.2
G4Jy 1212	0	158.5	-0.86 ± 0.04	5.077 ± 0.092	SDSS DR12	J150457.12+260058.4	0.05398 ± 0.00001	–	400.6
G4Jy 1216	0	188.2	–	68.229 ± 0.102	SDSS DR12	J151100.02+075150.2	0.45938 ± 0.00004	6.417 × 10 ²⁶ ± 5.468 × 10 ²⁴	197.7
G4Jy 1227	0	115.5	–	23.746 ± 0.049	SDSS DR12	J151215.74+02316.9	0.21985 ± 0.00002	–	672.9
G4Jy 1231	0	55.6	-0.87 ± 0.02	4.638 ± 0.040	SDSS DR16	J151644.48+070117.8	0.03453 ± 0.00001	1.536 × 10 ²⁶ ± 1.418 × 10 ²³	197.3
G4Jy 1239	0	25.2	-0.93 ± 0.01	55.856 ± 0.052	SDSS DR12	J151656.59+183021.5	0.58100 ± 0.00032	–	17.3
G4Jy 1240	1	18.8	–	6.454 ± 0.044	SDSS DR16 (re-fitted)	J152005.47+201605.4	1.57250 ± 0.00021	–	123.8
G4Jy 1244	0	18.0	–	14.881 ± 0.047	SDSS DR12	J1520060-283420	0.12264	2.458 × 10 ²⁶ ± 1.192 × 10 ²⁴	152.5
G4Jy 1245	0	80.5	-0.80 ± 0.01	6.504 ± 0.031	6dFGS	g152356.96+105543.4	0.41392 ± 0.00007	–	177.4
G4Jy 1255	0	16.4	–	4.203 ± 0.034	SDSS DR16	J153315.07+133225.1	0.77477 ± 0.00004	–	90.0
G4Jy 1267	0	19.4	–	5.469 ± 0.039	SDSS DR12	J153315.07+133225.1	0.77477 ± 0.00004	–	144.0
G4Jy 1270	0	14.2	–	6.875 ± 0.043	SDSS DR12	J153732.43+134448.1	0.67176 ± 0.00012	–	99.8
G4Jy 1272	1	47.7	-0.92 ± 0.02	4.816 ± 0.044	SDSS DR12	J154112.87+005032.0	1.13738 ± 0.00064	3.244 × 10 ²⁸ ± 2.948 × 10 ²⁶	392.2
G4Jy 1278	0	58.9	-0.82 ± 0.02	11.052 ± 0.053	SDSS DR16	J154743.53+205216.6	0.26428 ± 0.00002	2.255 × 10 ²⁷ ± 1.101 × 10 ²⁵	240.0
G4Jy 1286	0	54.0	0.04 ± 0.02	7.146 ± 0.043	6dFGS	g1556589-791404	0.05896	5.607 × 10 ²⁵ ± 3.383 × 10 ²³	61.6
G4Jy 1290	0	76.6	-0.95 ± 0.02	4.207 ± 0.045	SDSS DR16	J155907.05+121030.4	0.31736 ± 0.00004	1.364 × 10 ²⁷ ± 1.472 × 10 ²⁵	354.6
G4Jy 1291	0	102.1	-0.76 ± 0.02	4.052 ± 0.051	SDSS DR12	J160027.78+083743.0	0.22687 ± 0.00003	5.883 × 10 ²⁶ ± 7.462 × 10 ²⁴	371.3
G4Jy 1297	0	89.5	-0.87 ± 0.02	4.351 ± 0.058	SDSS DR12	J160240.36+154521.5	0.03738 ± 0.00001	1.405 × 10 ²⁵ ± 1.869 × 10 ²³	66.4
G4Jy 1306	0	2.5	-0.66 ± 0.01	8.798 ± 0.049	SALT	J160612.69+000027.2	0.058 ± 0.001	6.947 × 10 ²⁵ ± 3.897 × 10 ²³	2.8
G4Jy 1332	0	23.6	-0.66 ± 0.02	13.679 ± 0.068	SDSS DR12	J162439.08+234512.1	0.92715 ± 0.00011	4.731 × 10 ²⁸ ± 2.354 × 10 ²⁶	185.4
G4Jy 1339	0	63.9	-0.77 ± 0.02	13.033 ± 0.090	SDSS DR12	J162803.97+274139.3	0.44881 ± 0.00003	8.868 × 10 ²⁷ ± 6.123 × 10 ²⁵	367.5
G4Jy 1343	0	58.4	-0.88 ± 0.01	13.024 ± 0.046	SALT	J163141.60-265651.3	0.168 ± 0.001	9.984 × 10 ²⁶ ± 3.539 × 10 ²⁴	167.7
G4Jy 1348	0	56.7	-0.76 ± 0.03	7.952 ± 0.082	SDSS DR12	J163636.50+264809.2	0.55148 ± 0.00004	9.052 × 10 ²⁷ ± 9.331 × 10 ²⁵	367.1
G4Jy 1358	0	19.5	-0.56 ± 0.01	12.424 ± 0.057	SDSS DR12	J164348.60+171549.4	0.16300 ± 0.00002	8.494 × 10 ²⁶ ± 3.872 × 10 ²⁴	54.6
G4Jy 1360	0	207.0	-0.48 ± 0.02	25.322 ± 0.060	6dFGS	g1644161-771549	0.04297	1.071 × 10 ²⁶ ± 2.522 × 10 ²³	175.3
G4Jy 1364	0	18.1	-0.74 ± 0.01	11.270 ± 0.069	SALT	J164542.39+021145.0	0.094 ± 0.001	2.446 × 10 ²⁶ ± 1.502 × 10 ²⁴	31.6
G4Jy 1383	0	87.9	-0.43 ± 0.02	7.644 ± 0.040	6dFGS	g170241.10-774157	0.09461	1.655 × 10 ²⁶ ± 8.527 × 10 ²³	154.3
G4Jy 1402	0	216.6	-0.64 ± 0.01	232.344 ± 0.181	6dFGS	g1720282-005847	0.03038	4.875 × 10 ²⁶ ± 3.794 × 10 ²³	131.7
G4Jy 1423	0	308.8	-0.84 ± 0.01	39.071 ± 0.062	6dFGS	g1737358-563403	0.09839	9.425 × 10 ²⁶ ± 1.505 × 10 ²⁴	561.5
G4Jy 1487	0	17.7	–	30.436 ± 0.053	SALT	J183058.92-360230.7	0.078 ± 0.001	–	26.1
G4Jy 1504	0	88.7	-0.99 ± 0.01	19.111 ± 0.037	6dFGS	g1843146-483623	0.11072	6.022 × 10 ²⁶ ± 1.151 × 10 ²⁴	179.0
G4Jy 1511	0	20.1	-0.91 ± 0.01	10.105 ± 0.037	SALT	J185710.80-301940.1	1.554 ± 0.003	1.439 × 10 ²⁹ ± 5.204 × 10 ²⁶	170.3

Table 3. *Continued* – Angular sizes, spectral indices, 151-MHz flux-densities, redshifts, radio luminosities, and linear sizes for 299 G4Jy sources.

Source name	Confusion flag	Angular size / ''	G4Jy	Total $S_{151\text{MHz}}$	Redshift	Host-galaxy name	Spectroscopic redshift	$L_{151\text{MHz}}$ / W Hz $^{-1}$	Linear size / kpc
			spectral-index	/ Jy	origin				
G4Jy 1518	1	43.5	-1.00 ± 0.01	15.518 ± 0.048	SALT	WISEA J191548.68-265257.4	0.231 ± 0.003	2.463 × 10 ⁻²⁷ ± 7.547 × 10 ⁻²⁴	160.3
G4Jy 1526	0	82.7	-0.87 ± 0.01	8.137 ± 0.041	6dFGS	g1919280-295808	0.16670	6.116 × 10 ⁻²⁶ ± 3.081 × 10 ⁻²⁴	235.9
G4Jy 1533	0	16.5	0.14 ± 0.02	5.299 ± 0.038	6dFGS	g1924510-291430	0.35238	1.572 × 10 ⁻²⁷ ± 1.122 × 10 ⁻²⁵	81.9
G4Jy 1537	1	141.1	-1.00 ± 0.02	5.964 ± 0.057	6dFGS	g1926057-574017	0.06092	5.317 × 10 ⁻²⁵ ± 5.076 × 10 ⁻²³	165.9
G4Jy 1544	1	198.7	-0.72 ± 0.02	7.550 ± 0.053	6dFGS	g1928170-293144	0.02440	1.021 × 10 ⁻²⁵ ± 7.174 × 10 ⁻²²	97.7
G4Jy 1549	1	55.3	-1.06 ± 0.01	8.636 ± 0.035	6dFGS	g1931382-335442	0.09781	2.101 × 10 ⁻²⁶ ± 8.508 × 10 ⁻²³	100.0
G4Jy 1555	0	100.2	-0.81 ± 0.01	10.753 ± 0.041	SALT	J193325.00-394020.7	0.074 ± 0.001	1.421 × 10 ⁻²⁶ ± 5.410 × 10 ⁻²³	140.9
G4Jy 1565	1	18.5	-0.63 ± 0.01	25.361 ± 0.043	SALT	J194115.02-152431.2	0.454 ± 0.001	1.683 × 10 ⁻²⁸ ± 2.877 × 10 ⁻²⁵	107.1
G4Jy 1581	0	148.5	-0.88 ± 0.01	25.613 ± 0.065	SALT	J195215.79+023024.1	0.059 ± 0.001	2.121 × 10 ⁻²⁶ ± 5.384 × 10 ⁻²³	169.5
G4Jy 1592	1	16.8	-0.74 ± 0.01	9.100 ± 0.038	6dFGS	g1959038-353431	0.35292	3.542 × 10 ⁻²⁷ ± 1.471 × 10 ⁻²⁵	83.4
G4Jy 1606	0	48.5	-1.11 ± 0.02	5.048 ± 0.072	6dFGS	g2011275-564407	0.05514	3.679 × 10 ⁻²⁵ ± 5.260 × 10 ⁻²³	52.0
G4Jy 1613	0	494.2	-0.98 ± 0.02	10.348 ± 0.125	6dFGS	g2018013-553932	0.06059	9.109 × 10 ⁻²⁵ ± 1.101 × 10 ⁻²⁴	578.1
G4Jy 1619	0	20.1	-0.94 ± 0.02	6.130 ± 0.030	6dFGS	g2024353-051641	0.08218	1.020 × 10 ⁻²⁶ ± 4.935 × 10 ⁻²³	31.1
G4Jy 1635	1	61.0	-0.79 ± 0.01	11.789 ± 0.029	6dFGS	g2023166-225317	0.13140	5.241 × 10 ⁻²⁶ ± 1.286 × 10 ⁻²⁴	142.6
G4Jy 1638	0	24.1	-0.86 ± 0.01	8.809 ± 0.037	6dFGS	g2034447-354902	0.08873	1.711 × 10 ⁻²⁶ ± 7.140 × 10 ⁻²³	40.0
G4Jy 1643	0	220.8	-0.65 ± 0.01	9.344 ± 0.047	6dFGS	g2043457-263301	0.04074	3.568 × 10 ⁻²⁵ ± 1.805 × 10 ⁻²³	177.8
G4Jy 1658	0	27.6	-0.92 ± 0.03	4.066 ± 0.086	SDSS DR12	J205125.70+165253.1	0.52857 ± 0.00002	4.305 × 10 ⁻²⁷ ± 9.156 × 10 ⁻²⁵	173.4
G4Jy 1660	0	40.5	-0.54 ± 0.01	5.406 ± 0.036	SALT	J205202.35-570407.5	0.012 ± 0.001	1.731 × 10 ⁻²⁴ ± 1.146 × 10 ⁻²²	9.9
G4Jy 1664	0	37.5	-0.71 ± 0.01	12.294 ± 0.027	6dFGS	g2056043-195635	0.15651	7.871 × 10 ⁻²⁶ ± 1.715 × 10 ⁻²⁴	101.6
G4Jy 1665	0	84.9	-0.73 ± 0.01	5.727 ± 0.023	SALT	J205616.36-471447.6	1.488 ± 0.003	6.245 × 10 ⁻²⁸ ± 2.548 × 10 ⁻²⁶	718.3
G4Jy 1671	1	440.4	-0.73 ± 0.01	24.589 ± 0.063	6dFGS	g2101377-280154	0.03942	8.805 × 10 ⁻²⁵ ± 2.247 × 10 ⁻²³	343.6
G4Jy 1677	0	263.4	-0.82 ± 0.01	18.556 ± 0.051	6dFGS	g2107163-252808	0.03680	5.792 × 10 ⁻²⁵ ± 1.607 × 10 ⁻²³	192.5
G4Jy 1678	0	76.6	–	23.187 ± 0.051	6dFGS	g2107257-252543	0.03878	–	58.8
G4Jy 1686	0	14.1	-0.75 ± 0.01	12.094 ± 0.015	6dFGS	g2118106-301912	0.97711	5.031 × 10 ⁻²⁸ ± 6.079 × 10 ⁻²⁵	112.3
G4Jy 1698	0	18.2	-0.75 ± 0.01	11.697 ± 0.018	SALT	J213101.47-203656.1	1.630 ± 0.002	1.599 × 10 ⁻²⁹ ± 2.473 × 10 ⁻²⁶	154.2
G4Jy 1704	0	195.7	-0.83 ± 0.02	4.443 ± 0.047	SALT	J213406.70-533418.7	0.078 ± 0.001	6.569 × 10 ⁻²⁵ ± 6.899 × 10 ⁻²³	288.8
G4Jy 1705	0	72.0	-0.90 ± 0.02	4.187 ± 0.047	SALT	J213417.69-533811.1	0.076 ± 0.002	5.888 × 10 ⁻²⁵ ± 6.564 × 10 ⁻²³	103.7
G4Jy 1708	0	110.8	-0.78 ± 0.01	20.556 ± 0.032	6dFGS	g2137452-143256	0.19979	2.265 × 10 ⁻²⁷ ± 3.495 × 10 ⁻²⁴	365.4
G4Jy 1709	0	17.0	–	11.341 ± 0.019	SALT	J213750.00-204231.7	0.638 ± 0.004	–	116.8
G4Jy 1714	0	64.8	-1.11 ± 0.01	4.550 ± 0.017	6dFGS	g2140141-441228	0.07124	5.671 × 10 ⁻²⁵ ± 2.170 × 10 ⁻²³	88.0
G4Jy 1718	0	171.5	-1.55 ± 0.01	6.282 ± 0.037	6dFGS	g2143592-563721	0.08189	1.088 × 10 ⁻²⁶ ± 6.458 × 10 ⁻²³	264.5
G4Jy 1719	0	51.6	–	20.703 ± 0.142	SDSS DR12	J214411.71+281018.8	0.21461 ± 0.00002	–	179.8
G4Jy 1732	0	366.1	-0.74 ± 0.02	7.227 ± 0.054	6dFGS	g2151299-552013	0.03876	2.501 × 10 ⁻²⁵ ± 1.884 × 10 ⁻²³	281.2
G4Jy 1741	0	346.9	-0.85 ± 0.02	4.234 ± 0.031	6dFGS	g2154230-455232	0.14519	2.352 × 10 ⁻²⁶ ± 1.734 × 10 ⁻²⁴	882.7
G4Jy 1744	1	86.0	-1.06 ± 0.02	5.085 ± 0.084	SDSS DR16	J215541.97+123128.6	0.19305 ± 0.00004	5.462 × 10 ⁻²⁶ ± 9.044 × 10 ⁻²⁴	276.0

Table 3. *Continued* – Angular sizes, spectral indices, 151-MHz flux-densities, redshifts, radio luminosities, and linear sizes for 299 G4Jy sources.

Source name	Confusion flag	Angular size / ''	G4Jy spectral-index	Total $S_{151\text{ MHz}}$ / Jy	Redshift	Host-galaxy name	Spectroscopic redshift	$L_{151\text{ MHz}}$ / W Hz $^{-1}$	Linear size / kpc
G4Jy 1748	0	65.9	-0.50 ± 0.01	100.007 ± 0.077	6dFGS	g2157060-694124	0.02848	$1.833 \times 10^{26} \pm 1.415 \times 10^{23}$	37.7
G4Jy 1751	0	96.0	-0.86 ± 0.01	7.887 ± 0.019	6dFGS	g2201171-374624	0.03341	$2.023 \times 10^{25} \pm 4.949 \times 10^{22}$	63.9
G4Jy 1753	0	26.7	-0.63 ± 0.01	4.568 ± 0.014	6dFGS	g2201564-332103	0.15359	$2.777 \times 10^{26} \pm 8.782 \times 10^{23}$	71.2
G4Jy 1760	0	15.5	-0.31 ± 0.01	4.840 ± 0.021	6dFGS	g2209202-233153	0.08644	$8.504 \times 10^{25} \pm 3.611 \times 10^{23}$	25.1
G4Jy 1763	0	19.0	-0.74 ± 0.01	4.959 ± 0.023	6dFGS	g2211241-132810	0.39178	$2.449 \times 10^{27} \pm 1.135 \times 10^{25}$	100.8
G4Jy 1775	1	538.6	-0.86 ± 0.01	30.199 ± 0.112	6dFGS	g2223495-020613	0.05584	$2.229 \times 10^{26} \pm 8.250 \times 10^{23}$	583.9
G4Jy 1781	0	7.0	-0.50 ± 0.01	10.262 ± 0.017	SALT	J222918.63-405132.8	0.448 ± 0.002	$6.290 \times 10^{27} \pm 1.070 \times 10^{25}$	40.3
G4Jy 1786	0	90.1	-0.72 ± 0.01	9.259 ± 0.024	6dFGS	g2239114-172028	0.07411	$1.220 \times 10^{26} \pm 3.128 \times 10^{23}$	126.9
G4Jy 1788	1	62.4	-0.76 ± 0.01	4.285 ± 0.022	6dFGS	g2242237-604430	0.28157	$1.005 \times 10^{27} \pm 5.108 \times 10^{24}$	265.9
G4Jy 1795	0	32.7	-0.78 ± 0.01	26.175 ± 0.024	SALT	J225303.11-405746.7	0.307 ± 0.003	$7.502 \times 10^{27} \pm 7.016 \times 10^{24}$	148.0
G4Jy 1796	0	14.6	-0.78 ± 0.01	6.194 ± 0.018	6dFGS	g2254599-391304	0.26132	$1.236 \times 10^{27} \pm 3.624 \times 10^{24}$	59.0
G4Jy 1802	0	120.4	-0.79 ± 0.01	5.147 ± 0.020	6dFGS	g2303030-184126	0.12884	$2.193 \times 10^{26} \pm 8.514 \times 10^{23}$	276.8
G4Jy 1812	0	70.0	-1.17 ± 0.01	4.020 ± 0.017	6dFGS	g2313586-424339	0.05641	$3.081 \times 10^{25} \pm 1.291 \times 10^{23}$	76.6
G4Jy 1817	0	90.5	-0.71 ± 0.02	4.280 ± 0.031	6dFGS	g2319059-420649	0.05428	$2.954 \times 10^{25} \pm 2.120 \times 10^{23}$	95.5
G4Jy 1819	0	167.8	-0.88 ± 0.01	13.648 ± 0.031	SALT	J231956.26-272807.4	0.174 ± 0.001	$1.129 \times 10^{27} \pm 2.587 \times 10^{24}$	495.5
G4Jy 1829	0	16.9	-0.84 ± 0.01	14.654 ± 0.024	6dFGS	g2325197-120727	0.08212	$2.415 \times 10^{26} \pm 3.995 \times 10^{23}$	26.1
G4Jy 1831	0	92.5	-0.79 ± 0.01	10.289 ± 0.041	SDSS DR16	J232653.77-020213.7	0.18874 ± 0.00002	$1.002 \times 10^{27} \pm 3.955 \times 10^{24}$	291.6
G4Jy 1838	0	18.4	-0.77 ± 0.01	7.340 ± 0.026	SDSS DR16	J233225.59-095756.2	1.67157 ± 0.00064	$1.084 \times 10^{29} \pm 3.904 \times 10^{26}$	155.8
G4Jy 1842	0	60.6	-0.84 ± 0.01	5.008 ± 0.018	6dFGS	g2334449-525119	1.03189	$2.517 \times 10^{28} \pm 9.075 \times 10^{25}$	488.8
G4Jy 1856	0	18.1	-0.84 ± 0.01	7.566 ± 0.040	6dFGS	g2351561-010913	0.17362	$6.186 \times 10^{26} \pm 3.248 \times 10^{24}$	53.4
G4Jy 1858	0	62.4	-1.12 ± 0.01	22.438 ± 0.024	6dFGS	g2357007-344553	0.04941	$1.302 \times 10^{26} \pm 1.403 \times 10^{23}$	60.3
G4Jy 1863	0	372.9	-0.65 ± 0.01	125.123 ± 0.087	6dFGS	g2359043-605460	0.09573	$2.799 \times 10^{27} \pm 1.940 \times 10^{24}$	661.6